FACULTY
OF MATHEMATICS
AND PHYSICS
Charles University

DOCTORAL THESIS

Pavel Zháňal

Study of Phase Transformations in Ti Alloys

Department of Physics of Materials

Supervisor of the doctoral thesis:	RNDr. Petr Harcuba, PhD.
Study programme:	Physics
Study branch:	Physics of Condensed Matter and Materials Research

Prague 2018

I declare that I carried out this doctoral thesis independently, and only with the cited sources, literature and other professional sources.

I understand that my work relates to the rights and obligations under the Act No. 121/2000 Sb., the Copyright Act, as amended, in particular the fact that the Charles University has the right to conclude a license agreement on the use of this work as a school work pursuant to Section 60 subsection 1 of the Copyright Act.

In Prague, 25.7.2018 Signature

Acknowledgements

In the first place, I would like to thank my supervisor Petr Harcuba Ph.D. for his constant support and guidance during my studies. I would also like to express my gratitude to prof. Miloš Janeček, who acted as my supervisor for a few years of my doctoral studies, for his willingness to help even at the expense of his own free time.

I wish to thank all the members of group of ”Titans” at our department who were always available for discussion and often provided valuable new ideas, especially Jana Šmilauerová, Josef Stráský, Kristína Bartha, Dalibor Preisler and Jiří Kozlík.

I am also very grateful to prof. Václav Holý for his help with processing of X-ray data and to Přemysl Beran for measuring neutron diffraction with me and following data treatment. Another person deserving my thanks is Vasyl Ryukhtin for his help with small angle neutron scattering experiments.

My sincere thanks also goes to Jozef Veselý and Michal Hájek, who helped me with transmission electron microscopy and electrical resistance measurements, respectively. I would also like to appreciate their willingness to listen whenever I voiced my thoughts in our office and for their opinions on those thoughts. Further I have to mention their help with a lot of programming challenges.

Last but not least, I wish to extend my most sincere thanks to my family and friends, who supported and encouraged me during my studies.

Title: Study of Phase Transformations in Ti Alloys

Author: Pavel Zháňal

Department: Department of Physics of Materials

Supervisor: RNDr. Petr Harcuba, PhD., Department of Physics of Materials

Abstract: In this work phase transformations in metastable β (primarily Ti-15Mo) alloys were studied utilizing electrical resistance, dilatometry, transmission electron microscopy and X-ray and neutron diffraction. The materials - Ti-15Mo, Ti-6.8Mo-4.5Fe-1.5Al (LCB), Ti-5Al-5V-5Mo-3Cr (Ti-5553), Ti-29Nb-1Fe-0.5Si (TNFS), Ti-15Mo-3Nb-3Al-0.2Si (Timetal 21S) and Ti-13Cr-1Fe-3Al (TCFA) (in wt. %) - were subjected to a solution treatment at a temperature above β transus and quenched into water. In this condition, the microstructure of the investigated materials consists of β matrix and ω particles. Samples quenched from important temperatures determined from in-situ electrical resistance and dilatometry measurements were studied by post-mortem TEM. In-situ X-ray and neutron diffraction provided direct observations of microstructure of Ti-15Mo alloy during linear heating and confirmed statements based on results of indirect methods, such as: the decrease of volume fraction of ω phase during heating at low temperatures (up to 250 °C), complete dissolution of ω phase at 560 °C and precipitation of α phase without ω particles serving as its direct precursors. X-ray diffraction experiment allowed to determine relative evolution of the size of ω particles while phase fraction evolution was derived from neutron diffraction. The volume fraction of β phase at room temperature is about 60 %. The volume fraction of ω phase during heating with the heating rate of 5 °C/min reaches its maximum value of 45 % at about 400 °C. The maximum amount of the volume fraction of α phase during the same experiment was 11 % at about 650 °C.

Keywords: metastable β-Ti alloys ω phase electrical resistance dilatometry X-ray diffraction neutron diffraction phase transformations

Contents

Introduction

The thesis is the continuation of my master thesis, which I defended at 2014. It presents results achieved mainly during my following doctoral study. I actively participated not only in a significant part of the measurements and but also in following analysis of the obtained data. Due to several utilized experimental methods a support and consultations with experienced researchers were required. Their help made this thesis possible.

Titanium alloys are used in a wide range of components for the aerospace and chemical industry and as alternative structural materials for the automotive sector due to their high specific strength and excellent fatigue and corrosion resistance. Moreover, due to biocompatibility and partial or total superelasticity, β-Ti alloys are also considered for biomedical applications. The mechanical properties of these alloys are mainly determined by the distribution and the size of metastable ω particles or stable α precipitates in β matrix. The formation of the precipitates, their morphology, volume fraction, the size and the distribution are influenced by phase transformations occurring during heat treatment. Therefore, a thorough understanding of these processes is necessary to optimize the mechanical properties of the material through thermomechanical treatment.

Two types of experimental method were employed in this thesis: direct and indirect. The direct methods bring more complex results and unambiguous explanations of occurring processes. However, such methods have usually limited accessibility. On the other hand, the indirect techniques could be found in standard laboratories of universities and research institutions investigating material properties. In order to provide a clear description of occurring processes by utilizing easily available techniques, we aim to clarify the detected phenomena with unique direct methods.

The thesis is divided to four chapters. The first chapter: theoretical background and literature review describes characteristics of titanium and its alloys. Special attention is given to ω phase and its possible evolution. The description of experimental procedures follows in the next chapter. A brief characterization of all investigated alloys is presented. Even though I was not able to employ some of the experimental techniques on my own and needed the assistance and expertise of colleagues mentioned in the acknowledgement, I tried to understand the fundamentals of employed experimental methods and to interpret the results.

Results and discussion chapter contains two discussions, which divide the results obtained from the indirect (electrical resistance measurement, dilatometry, ex-situ transmission electron microscopy) and the direct experimental techniques (in-situ transmission electron microscopy, X-ray and neutron diffraction). Short summary of the main results for each method is provided. The final conclusions and the most important achievements of the thesis are summarized at the end.

1. Theoretical background and Literature review

1.1 Characteristics of Titanium

Titanium is the ninth most plentiful element and the fourth most abundant structural metal in the Earth's crust. Unfortunately, it is never found in a pure state and seldom found in high concentrations [1]. It has atomic number 22 and belongs to Group 4 of the periodic table of elements. Titanium is a shiny element with a silver color, low density, high strength and high corrosion resistance. In nature it occurs in five isotopes, ^{46}Ti through ^{50}Ti, with ^{48}Ti being the most abundant (73.8%) [2]. Its incomplete 3d shell enables it to form solid solutions with most substitutional elements, which have atomic radius within ± 20 % [3] of titanium. In its elemental form it has a melting point of 1678 °C.

Titanium was discovered in 1791 by British clergyman and amateur mineralogist William Gregor. He investigated the magnetic sand (ilmenite $FeTiO_3$) from the local river, Helford, in the Menachan Valley in Cornwall, England. By removing the iron and treating the sand with hydrochloric acid he produced the impure oxide of a new element. Four years later, a German chemist Martin Heinrich Klaproth, analyzed rutile (TiO_2) from Hungary and identified it as an oxide of an unknown element, the same as the one reported by Gregor. Klaproth named the element after the Titans, the powerful sons of the earth in Greek mythology. The titans were utterly hated by their father and so he detained them in captivity in the earth's crust, similar to the hard to extract ore - therefore he named it Titanium [1, 4].

The element was isolated for the first time in 1910 by Matthew Albert Hunter by heating titanium tetrachloride ($TiCl_4$) with sodium. Commercially usable process of titanium production was developed by Wilhelm Justin Kroll from Luxembourg. In 1932 he produced significant quantities of titanium by combining $TiCl_4$ with magnesium. The obtained material is called "titanium sponge" because of its porous and spongy appearance. This so called Kroll process remained essentially unchanged and is the dominant process for titanium production today. The starting ore for the production of titanium is either rutile (TiO_2) or ilmenite ($FeTiO_3$). The extraction of metallic titanium from these ores occurs in following steps [1, 4, 5]:

- Chlorination of the rutile (ilmenite) to produce $TiCl_4$:

  $$\mathrm{TiO_2 + 2\,Cl_2 + C \longrightarrow TiCl_4 + CO_2}$$

  and

  $$\mathrm{TiO_2 + 2\,Cl_2 + 2\,C \longrightarrow TiCl_4 + 2\,CO.}$$

- Purification of $TiCl_4$ by distillation.

- Reduction of the $TiCl_4$ - Kroll process. The purified $TiCl_4$ is put into a reactor filled with inert gas and containing metallic Mg and heated to drive reactions:

  $$\mathrm{TiCl_4 + Mg \longrightarrow TiCl_2 + MgCl_2}$$

  followed by

  $$\mathrm{TiCl_2 + Mg \longrightarrow Ti + MgCl_2}$$

  Product of these reactions is a solid mass of intermingled mixture of highly porous metallic titanium sponge and $MgCl_2$.

- Extraction of the metallic titanium from the sponge by removal of the residual $MgCl_2$:
  Several methods can by employed to separate $MgCl_2$: acid leaching, inert gas sweep, or vacuum distillation. The former method is no longer utilized extensively. In both other processes (inert gas sweep and vacuum distillation), the Mg and Cl_2 are recovered and recycled. Today, these methods can be nearly considered as a closed loop batch process with only modest amounts of new Mg and chlorine being required from batch to batch [1].

- Crushing and sizing of the titanium sponge:
  The sponge is crushed to granules of metallic titanium typically to sizes about 3 - 5 cm. This eliminates the cost of further crushing.

- In order to prepare ingot, the titanium sponge is pre-densified in a hydraulic press. These compacts are then assembled to an electrode for the melting process, which results in bulk titanium without pores.

Titanium has a low density, of about 60 % of steel and can be greatly strengthened by alloying (which results to even more favourable strength-to-density ratio) or deformation processing. It is exceptionally corrosion resistant (often exceeds stainless steels). Pure titanium is non-toxic and some of its alloys are biologically compatible with human tissues and bones. Titanium alloys primarily excel due to two properties: the high specific strength (73 kN m/kg for pure Ti [6] and 260 kN m/kg for β Ti alloy [7] compared to 46 and 63 kN m/kg for low carbon [8] and stainless [9] steels, respectively) and excellent corrosion resistance, which make them significantly useful in: power generation as condensers, heat exchangers,flue gas scrubbers; water plants as heat exchangers, well heads, pipe and down hole hardware; pulp and paper as diffusion washers in bleaching section of process; chemical industry as dimensionally stable electrodes; metal production as cathodes for electrowinning Cu, Au, and Zn; mineral dressing as pressure vessels at high T and P; biomedical devices as orthopedic implants, surgical implants, surgical implements; spacecraft as cryogenic tanks and as aircraft structural parts. Unfortunately, the maximum application temperature of titanium ad its alloys is limited by their oxidation behaviour. The main reason hindering wider use of titanium for example in automotive applications is the difficult and costly reduction of oxide to metal described above [1, 4]. Selection of important physical properties of highly pure polycrystalline α titanium is listed in Table 1.1.

Structure prototype	Mg
Pearson symbol	hP2
Space group	$P6_3/mmc$ (194)
β-transus temperature	882 °C
Lattice parameters	a = 0.295 nm c = 0.468 nm c/a = 1.587
Thermal expansion coefficient [10^{-6} K^{-1}]	8.36
Thermal conductivity [W/mK]	14.99
Specific heat capacity [J/kgK]	523
Electrical resistance [10^{-9} Ωm]	564.9
Elastic modulus [GPa]	115
Shear modulus [GPa]	44
Specific strength [kN m/kg]	73
Poisson's ratio	0.33

Table 1.1: Physical properties of high-purity polycrystalline α titanium (> 99.9 %) at 25 °C [1].

1.2 Structural modifications of titanium

Different structural modifications/phases depending on various factors like temperature, pressure, cooling rate and alloying elements can exist in both pure titanium and Ti alloys. The phases can be classified into equilibrium and non-equilibrium. By applying appropriate (fast) heating/cooling rates, metastable or non-equilibrium phases can form via displacive transformations like shearing and shuffling. Under favourable conditions, these metastable phases can transform into more stable ones.

1.2.1 Equilibrium phases

At room temperature and pressure, pure titanium crystallizes in a hexagonal close packed structure (hcp), so-called α phase. Its structure is shown in Fig. 1.1a. α phase has a space group of $P6_3/mmc$. Its unit cell has lattice parameters $a = 2.95\,\text{Å}$ and $c = 4.68\,\text{Å}$. The c/a ratio for pure α titanium is 1.587, which is smaller than ideal ratio 1.633 for hcp. Stability limit of α phase is at 882 °C, which is known as β-transus temperature. Above this temperature, the structure of titanium allotropically transforms into a body-centered cubic (bcc) β phase, which is stable up to the melting point of titanium (1678 °C) and belongs to space group $Im\overline{3}m$. Fig. 1.1b shows the unit cell of β phase. Its lattice parameter is $a = 3.32\,\text{Å}$ for pure titanium at 900 °C. The most densely packed lattice planes for both phases and directions are indicated in Fig. 1.1 [10].

It is necessary to note that alloying elements can alter the β-transus temperature. According to their influence on the β-transus, alloying additions can be divided into three groups: α stabilizing, β stabilizing and neutral ones. Scheme of the effect of some elements on phase diagrams of titanium alloys is shown in Fig. 1.2.

The elements which increase β-transus temperature are known as the α sta-

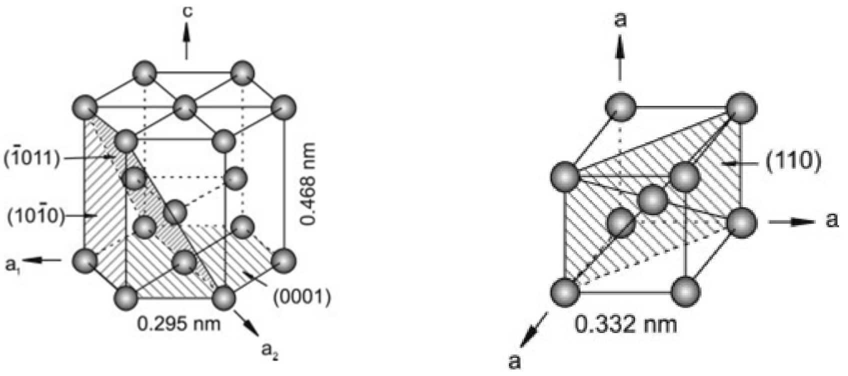

(a) Hexagonal close-packed cell of α phase. (b) Body centered cubic cell of β phase.

Figure 1.1: Structure modifications of Ti [4].

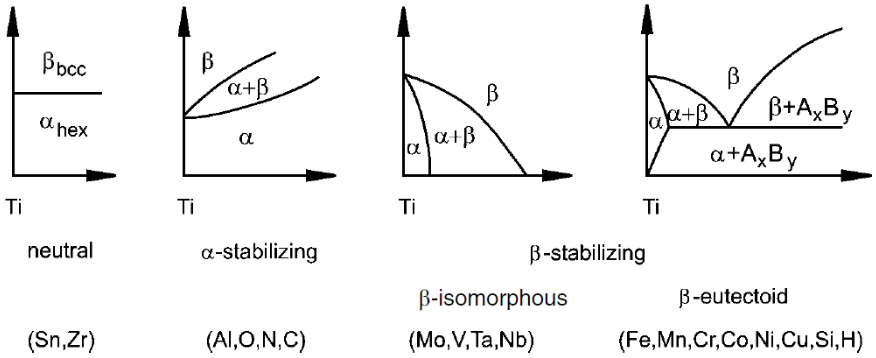

Figure 1.2: Influence of different types of alloying elements on phase diagrams of titanium alloys [4].

bilizing elements (e.g. Al, B, Sc, Ga, La, Ce, Ge, C, O, N) [11]. Oxygen is frequently used to increase the strength of commercially pure titanium. The effect of α stabilizers in multicomponent titanium alloys can be compared in terms of Al equivalency [12]:

$$[Al]_{eq} = [Al] + 0.17[Zr] + 0.33[Sn] + 10[O] \tag{1.1}$$

On the other hand, β stabilizing elements decrease the β-transus temperature. β stabilizing elements can be further divided to β isomorphous (e.g. V, Nb, Mo, Ta and Hf) and β eutectoid (e.g. Fe, Cr, Mn, Co, Ni, Cu, W, Au, Ag, Pt and Pd), depending on whether or not a solid solution / eutectoid compound exists in the material at elevated temperature. Similar to α stabilizers, the effect of β stabilizers could be expressed in terms of Mo equivalency depending on the amount of additions required to suppress the martensitic start temperature below room temperature [11]:

$$\begin{split}[Mo]_{eq} = [Mo] + 0.2[Ta] + 0.28[Nb] + 0.4[W] + 0.67[V] \\ + 1.25[Cr] + 1.25[Ni] + 1.7[Mn] + 1.7[Co] + 2.5[Fe]\end{split} \tag{1.2}$$

Some other elements like Zr, Sn and Hf behave more or less neutrally as they lower the β-transus slightly but again increase it at higher concentrations. Zr and Hf are isomorphous with Ti and they exhibit allotropic phase transformation $\beta \leftrightarrow \alpha$. Titanium is substituted by Zr in a multicomponent alloy and indirectly has a α-stabilizing effect. On the other hand, Sn belongs to the β eutectoid forming element but has no effect on the β-transus temperature. However, Sn is considered to be α stabilizing as it replaces Al in the hexagonal ordered Ti_3Al.

Although α and β phases are most known stable phases of titanium, there are several others, such as:

B2

B2 (or so called A2), which has a simple cubic superlattice (space group $Pm\overline{3}m$). The B2 phase was observed in several binary and ternary titanium aluminides, and nickelides [3].

$\boldsymbol{\alpha_2}$

α_2, which crystal structure is a DO_{19}. Its unit cell is composed of four regular hcp cells and it is an ordered hexagonal solid solution of chemical formula Ti_3SM (where SM denotes simple metals such as Al, Ga, In or Sn) [11].

$\boldsymbol{\gamma}$

γ with $L1_0$ structure is an intermetallic structure seen the most when 50 % of Al is added to titanium. Its (100) planes alter between Ti and Al.

O

An orthorombic (*Cmcm*) O phase was discovered in Ti-Al-Nb systems and could have potential as a structural material for use at elevated temperatures [13].

$\mathbf{B8_2}$

Another ternary phase discovered in Ti-Al-Nb system is $B8_2$. This phase is in apparent equilibrium with the γ, α_2 and O phases [14]. The phase has the $B8_2$ structure of the ω-type phases [15].

1.2.2 Non-equilibrium phases

Non-equilibrium (or metastable) phases usually form during very fast processes (e.g. quenching or deformation), which prevent reaching the thermodynamic equilibrium. These phases are a compromise between thermodynamics which tend to lower the Gibbs free energy and kinetics which dictate how fast the transformation can occur. A brief description of some of the metastable phases encountered in titanium alloys follows.

$\boldsymbol{\alpha'}$

Martensitic α' phase forms during quenching from β phase instead of α due to fast quenching rates. It has a hexagonal crystal structure ($P6_3/mmc$) and can be found in pure titanium and α alloys. Due to element partitioning the lattice parameters of α and α' should differ as α' is supersaturated in β stabilising elements whereas α is not. Two morphologies of α' were observed, namely massive and acicular martensite. The massive martensite forms only in pure titanium and very dilute alloys as large irregularly shaped regions consisting of individual α laths. The acicular martensite forms in alloys with a higher solute content and contains individual α plates [1, 4, 16]. With increasing content of β-stabilizing elements the martensite start (T_{ms}) temperature decreases and thus this phase is less easily formed.

α''

In alloys with higher solute content, α'' can form [11]. It was shown that its structure is more or less twinned. α'' can also form due to application of external forces as stress induced or strain induced martensite [5], which agrees with its orthorombic structure, which is a halfway between the bcc β and the hcp α [17].

ω

Probably the most investigated and the most important metastable phase in titanium alloys also in the context of this thesis is ω phase. It has received extensive attention since its discovery in 1954 [18] mainly due to ω particles possibly serving as preferential nucleation sites for α precipitates. Fine and uniformly dispersed α precipitates in β matrix result in excellent mechanical properties of the material [19, 20]. The ω particles also affect some physical properties such as ductility, superconductivity, etc. The structure of ω phase is either hexagonal ($P6/mmm$ space group) in leaner alloys [21] or trigonal ($P\overline{3}m1$ space group) in more heavily stabilized β alloys [22]. ω particles are extremely fine (from a few nanometres to a few tens of nanometres) and their crystallographic matrix is coherent with β phase matrix [17]. ω particles are either prolate sphereroids (main axis $\parallel \langle 111 \rangle_\beta$) or cuboids and their number density is extremely large [13]. They are ordered in a cubic array along $\langle 100 \rangle$ directions in β matrix [23]. ω phase is present not only in titanium but also in Zr, and Hf alloys [24].

The main conditions under which ω phase forms and further grows are according to [25, 26]:

1. The thermal treatment:

   Two stages of ω phase are distinguished according to the conditions of their formation [26]:

   (a) When the content of β stabilizing elements is just high enough to retain full β upon quenching (i.e. the T_{ms} is suppressed below room temperature), ω can form from β phase. This is commonly called athermal ω (ω_{ath}). The formation of this phase is diffusionless and experiments proved the reversibility of $\beta \leftrightarrow \omega_{ath}$ transformation [27–29]. It was also shown, that even ultra fast quenching rates were unable to suppress this transformation [22]. For a particular composition there is a specific ω-start temperature (T_ω), where this phase forms during quenching.

(b) The ω phase forms during ageing at temperatures near T_ω (100 - 500 °C, the exact temperature depends on alloy composition) [30]. This is called isothermal ω (ω_{iso}), as thermal activation is necessary for its growth. ω_{iso} particles probably evolve from ω_{ath} particles, which remain in the material after heating to a certain temperature. The growth of ω_{iso} particles is diffusion controlled displacement mechanism [31]. Ageing at suitable temperature is accompanied by rejection of β-stabilizers from ω_{iso} particles, which results in a shift of lattice parameter of both β and ω phases [32].

Even though ω_{iso} being the continuation of ω_{ath} [33], rather than different phase, these two modifications can be distinguished by the fact that the ω_{iso} is larger in size, and there is a composition gradient across the β/ω_{iso} boundary [31]. As the $\beta + \omega_{iso}$ mixture is metastable, prolonged ageing leads to heterogeneous precipitation of α precipitates (preferentially on ω_{iso} particles) and results in an equilibrium $\beta + \alpha$ phase composition.

2. The pressure: The pressure enhances the formation of the ω phase and extends the range of compositions in which the ω is observed. At room temperature, the pressure necessary to transform α to ω has to be higher than about 30 kbar [25, 34].

3. The deformation: The formation of the ω phase was firstly observed during deformation in Ti-8Cr [35] and in Ti-V alloy single crystal [36]. In the recent years, the deformation induced ω phase was investigated, with the aim to develop a titanium alloy with a changeable Young's modulus for biomedical applications [37, 38] .

β'

If the solute content of β-stabilizer is high enough, the metastable ω phase becomes unstable and does not precipitate any longer. On the other hand, the β phase separates into β_{lean} and β_{rich} [30]. This occurs either by nucleation and growth or by spinodal decomposition depending on the kinetics of the separation. β_{lean} is known as β' and β_{rich} simply as β. Both β phases have the same crystallographic structure as the parent phase. The only differences are therefore the solute content and lattice parameters. β' forms coherent and uniformly dispersed particles within the β matrix [4].

O′

Recently discovered nano-sized O' phase with orthorhombic symmetry and occurs by a $\{110\}\langle\bar{1}10\rangle$ shuffle (atoms shuffle every other $\{110\}_\beta$ atomic plane) [39].

O″

Another newly found phase, has been termed O". It has ordered face centered orthorhombic structure and was be observed co-existing with ω_{iso} and α phases in Ti-5Al-5Mo-5V-3Cr alloy [40].

1.3 Identification of Ti alloys (based on β stabilizing elements content)

Titanium alloys are divided with respect to the amount of the alloying elements into α, α+β and β alloys. The identification is schematically shown in Fig. 1.3.

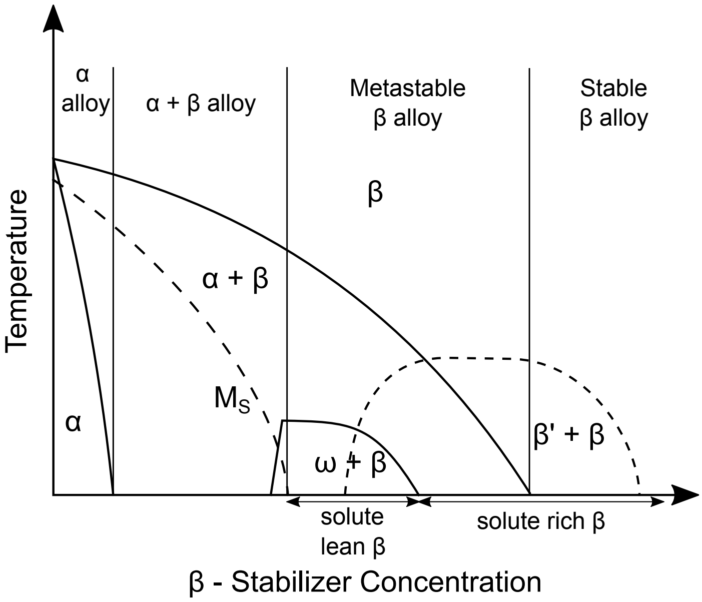

Figure 1.3: Schematic β isomorphous phase diagram of to identify Ti alloys [4].

α alloys comprises only pure Ti and different grades of commercially pure Ti, Ti alloyed with the α-stabilizers, or with neutral elements. In case of addition of minor fractions of β stabilizing elements, the alloys are referred to as the near α alloys [4]. Unfortunatelly, it is not possible to improve mechanical properties of either α or near α alloy by thermal processing. Alloying titanium with oxygen leads to increse in both strength and Youngs modulus [1], however, results in significant decrease of ductility. The main advantage of α alloys is their high corrosion resistance [10].

With increasing content of β stabilizers, the material reaches $\alpha + \beta$ region. The $\alpha+\beta$ alloys, which contains both these phases are in Fig. 1.3 located between $\alpha/(\alpha+\beta)$ phase boundary and the point where T_{ms} drops bellow the room temperature. The volume fraction of α phase, which forms martensitically upon quenching ranges at room temperature from 5 - 40%. The ability to control the microstructure and mechanical properties of these alloys by heat treating predetermines $\alpha + \beta$ alloys to be the most widely used titanium alloys in commercial and technical applications [4].

When the content of β stabilizing elements increases further, T_{ms} decreases bellow room temperature and β phase no longer transforms upon quenching. This is still in the $\alpha + \beta$ region, but such material already belongs to metastable β alloys. Stable β titanium alloys can be reached by additional increase of the content of β stabilizing elements (see Fig. 1.3). In the equilibrium, the volume fraction of α phase in metastable β-Ti alloys can be more than 50 % [1]. The α phase can be precipitated from the metastable β phase as very fine particles. Therefore, the main characteristic of β alloys is that they can be hardened to much higher yield stress levels than $\alpha + \beta$ alloys. On the other hand, stable β alloys are single-phase, they cannot be precipitation hardened. Therefore, the stable β alloys have very limited practical use Metastable β alloys are the most versatile from all titanium alloys. The main advantages of metastable β alloys are the high strength to weight ratio, the high ductility and the high fatigue resistance. Furthemore the metastable β alloys can be processed at lower temperatures than $\alpha + \beta$ alloys [4, 10].

1.4 Phase transformations in metastable β titanium alloys

The mechanical properties of titanium alloys are mainly determined by the distribution and the size of metastable ω particles or stable α precipitates in β matrix [41, 42]. The formation of the precipitates, their morphology, volume fraction, the size and the distribution are influenced by phase transformations occurring during heat treatment [5, 43]. Therefore, a thorough understanding of these processes is necessary to optimize the mechanical properties of the material through thermomechanical treatment. The phase transformations relevant for this study are $\beta \leftrightarrow \omega$, $\omega \rightarrow \alpha$ and $\beta \leftrightarrow \alpha$. These transitions are discussed bellow.

1.4.1 $\alpha \leftrightarrow \beta$

The precipitation of α phase in β matrix in metastable β-Ti alloys is a thermally activated diffusional process. It is controlled by the migration of the α/β interface and the diffusion of solute atoms across the interface. The growth rate is determined by the slower of these simultaneously occurring processes. When the diffusion of solute atoms is slower than the interface migration rate, the interface will move as fast as the diffusion allows and the transformation is said to be diffusion controlled. On the other hand, when the interface mobility is the limiting process, interface controlled transformation occurs [16]. Upon cooling from the temperatures above β-transus, the most densely packed planes of the bcc β phase $\{110\}$ transform to basal planes $\{0001\}$ of hexagonal α phase. α phase precipitates most commonly obey Burgers orientation relationship with respect to β matrix [4, 44].

$$\begin{gathered}(0001)_\alpha \parallel (110)_\beta \\ [11\overline{2}0]_\alpha \parallel [111]_\beta\end{gathered} \tag{1.3}$$

Graphical representation of ideal Burgers orientation relationship is shown in Fig. 1.4.

Other orientation relationships observed between bcc and hcp structures are:

i) Pitsch-Schrader[46]:

$$\begin{gathered}(0001)_\alpha \parallel (110)_\beta \\ [11\overline{2}0]_\alpha \parallel [001]_\beta,\end{gathered} \tag{1.4}$$

which was also found in titanium alloys [47, 48].

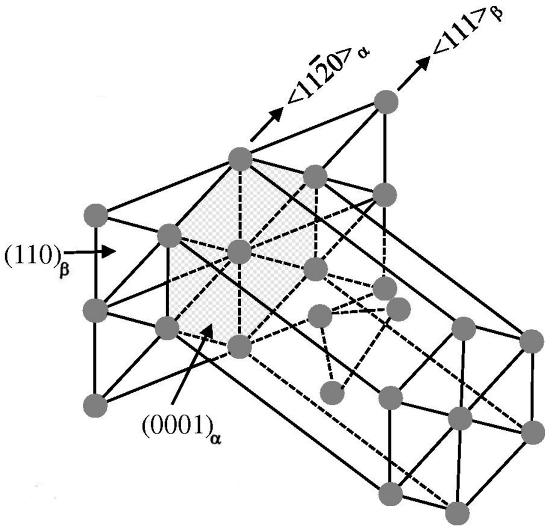

Figure 1.4: Graphical representation of ideal Burgers orientation relationship [45].

ii) Rong-Dunlop, first observed in [49] and also reported in titanium alloys [50]:

$$\begin{aligned}(0001)_\alpha &\parallel (021)_\beta \\ [11\bar{2}0]_\alpha &\parallel [100]_\beta,\end{aligned} \tag{1.5}$$

iii) Potter [51]:

$$\begin{aligned}(\bar{1}011)_\alpha &\parallel (110)_\beta \\ [\bar{2}110]_\alpha &\parallel [1\bar{1}1]_\beta.\end{aligned} \tag{1.6}$$

The grain boundary α precipitates were found to have the Potter orientation relationship rather than the Burgers orientation relationship with one of the adjacent β grains in [52].

α phase in metastable β alloys preferably grows at nucleation sites, such as: β/β grain boundaries, previously formed α particles, ω particles, dislocations and β' phase formed during phase separation. In $\alpha + \beta$ alloys, the martensite plates serve as additional nucleation site [25].

Each nucleation site results in a special morphology and distribution of the α phase. Based on the ageing temperature and the nucleation site, three types of nucleation mechanisms are distinguished [4, 25, 31]:

At ageing temperatures below approximately 450 °C (exact temperature depend on the material), the appearance of α is preceded by ω. The α precipitates are extremely fine and uniformly dispersed throughout the β matrix. This transformation is explained in detail in Section: 1.4.3.

For ageing temperatures above about 400 °C, a sufficient thermal activation to allow non-uniform nucleation of the α phase is reached. The nucleated α phase does not have any relationship to ω phase in the β matrix. Preferential nucleation site for this transformation are β/β grain boundaries, but there is also an evidence of nucleation within grains. The precipitates of the α phase are non-uniform plates with high aspect ratio.

The third precipitation mechanism occurs at temperatures above circa 650 °C. Thick α layers form along β/β grain boundaries with smaller number of the α precipitates, which grow towards the grain interior as parallel plates belonging to the same variant of Burgers orientation relationship (so-called α colonies or families). This process is referred to as sympathetic nucleation and growth, and the resulting α structure is known as Widmanstätten side plates.

1.4.2 $\beta \leftrightarrow \omega$

ω phase is a metastable phase, which occurs in Ti alloys which contain the required levels of β stabilizing elements to suppress T$_{ms}$ below room temperature. The mechanism of ω phase formation was proposed in [53] and described in [54]. ω_{ath} forms by a diffusionless, displacive transformation upon quenching from temperatures above β-transus. In the most common model $\beta \rightarrow \omega$ transformation, the ω forms by collapsing a pair of the $(111)_\beta$ planes to the intermediate position, leaving the next plane unaffected, and collapsing the next pair of planes and so on, which creates a hexagonal ω lattice. This process is schematically shown in Fig. 1.5. According to this picture, the planes marked as 1/3 and 2/3 collapse in the middle and the 0 and 1 are unaffected.

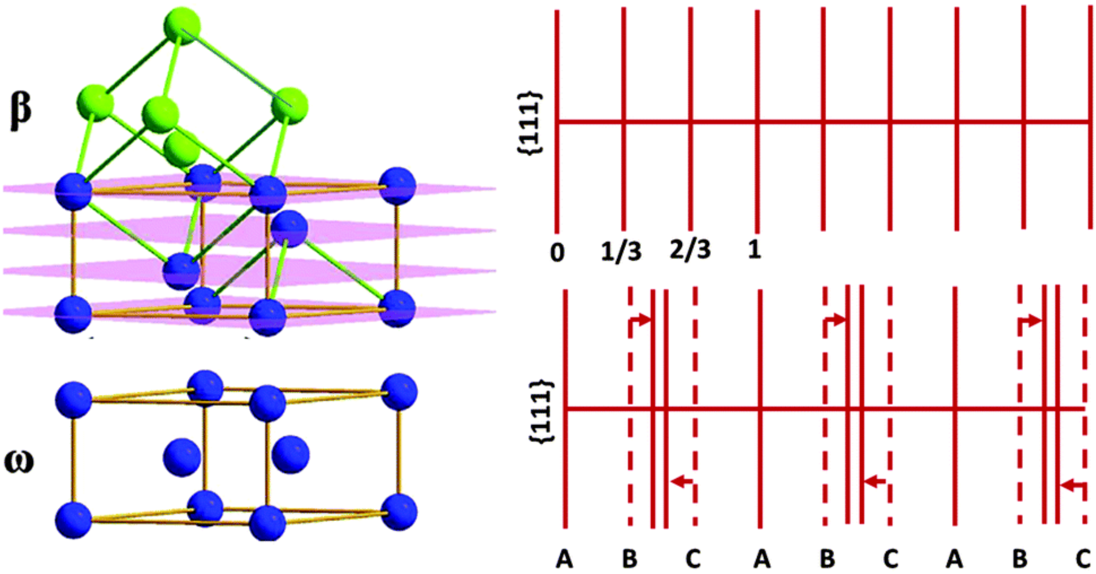

Figure 1.5: Schematic collapse of $(111)_\beta$ planes [55].

The complete collapse of $(111)_\beta$ planes create basal plane $(0001)_\omega$ of hexagonal ω phase. However, it has been shown, that the collapse can be only partial, which results in a trigonal symmetry of ω phase [56, 57]. The orientation relationship between the β and the ω phase is for fully collapsed $(111)_\beta$ planes the following:

$$\begin{gathered}(111)_\beta \parallel (0001)_\omega \\ [1\bar{1}0]_\beta \parallel [11\bar{2}0]_\omega\end{gathered} \tag{1.7}$$

There are four $[111]_\beta$ directions, which results into four possible crystallographic variants of the ω structure in β phase matrix. Lattice parameters for the ideal ω phase (completely collapsed $(111)_\beta$ planes) can be easily calculated with respect to lattice parameter of β phase:

$$a_\omega = a_\beta\sqrt{2}, c_\omega = a_\beta\sqrt{3}/2 \tag{1.8}$$

1.4.3 $\omega \rightarrow \alpha$

During ageing of the material consisting of $\beta + \omega$ mixture, α phase heterogeneous nucleation can occur. Preferential nucleation sites for α formation are inhomogeneities in the material, such as ω particles, grain boundaries, β' phase or dislocations. Different mechanisms of ω assisted nucleation of α phase have been suggested:

It was shown in [58] that if the misfit of β/ω interface exceeds a critical value, interfacial edge dislocations form in $\langle 110\rangle_\beta$ directions. α rod-shaped precipitates form in the same orientation as the corresponding dislocations. The nucleation at the dislocation or in its vicinity occurs due to stress fields induced by the dislocation and after sufficient ageing time, α phase grows over dissolving ω particles. The $\alpha/\beta/\omega$ orientation relationship in such conditions was found to be [59]:

$$\begin{gathered}(0001)_\omega \parallel (\bar{1}2\bar{1}0)_\alpha \parallel (\bar{1}11)_\beta \\ (\bar{1}\bar{1}20)_\omega \parallel (0001)_\alpha \parallel (0\bar{1}1)_\beta \\ [1\bar{1}00]_\omega \parallel (10\bar{1}1)_\alpha \parallel [211]_\beta\end{gathered} \tag{1.9}$$

In the systems with a lower ω/β misfit, there are three different models of $\omega \rightarrow \alpha$ transformation [60]:

- In [61] the authors proposed that α precipitates are supposed to nucleate at a certain distance from the ω/β interface. This is caused by local rejection of the ω destabilizers (= α stabilizers; Al, in this case), during the isothermal ageing of ω precipitates, which is supposed to allow the nucleation of α precipitates in the vicinity of ω precipitates.

- Another hypothesis states, that α phase nucleates within the core of ω particles, leading to the formation of α platelets [58]. There should be a strict orientation relationship at α/ω interface. This leads to a perfect planar interface between these two phases and α phase is able to grow from ω phase. Initially, α phase growth is assumed to occur solely by the consumption of ω particles. This leads to a plate-like morphology. After the complete disappearance of ω phase, α growth should be governed by the interface mobility between α and β [62].

- The last model suggests that in Ti-5Al-5Mo-5V-3Cr-0.5Fe α phase nucleates in Al-rich regions in the vicinity of β/ω interface via displacive-diffusional transformation in which the rate-controlling mechanism is the diffusional partitioning of the alloying elements [60]. Similar results were observed in Ti-6Cr-5Mo-5V-4Al alloy [63]. Although, the preferential α nucleation sites were oxygen rich regions at β/ω interface. These regions can form due to the diffusion of interstitial oxygen towards the dislocations at the interface.

1.5 Electrical resistivity of titanium alloys

Out of many books describing electrical resistivity or resistance of metals in general, only few mention unusual behaviour of electrical resistivity in Ti alloys caused by ongoing phase transformations. Normalized resistivity of quenched LCB Ti during heating and cooling between 30 °C and 900 °C with $dT/dt = 2\ °\mathrm{C\,min}^{-1}$ investigated in [64] is shown in Fig. 1.6. Rossiter dedicated a special chapter to displacive phase transitions such as $\beta \leftrightarrow \omega$ [65]. Anomalous temperature dependence of the electrical resistivity of metastable β titanium alloys was noted for the first time around 1955 [66, 67]. Ho and Collins studied negative $d\rho/dT$ in Ti-Mo alloys [68], which is the similar system as studied in this thesis. The negative $d\rho/dT$ dependence was also observed in other Ti-T_2 alloys (where T_2= V, Cr, Nb) and in Zr-Nb [69–72], within concentration ranges which is known to favour the precipitation of the ω phase. Therefore, the decrease of resistance with increasing temperature from room temperature up to approximately 200 °C (the exact temperature depends on the composition) was attributed to dissolution of ω phase back into β matrix. This transformation is (at low temperatures) fully reversible, which was shown in our previous work [28], where the resistance of the material after heating followed by cooling returned back to the initial value. The electrical resistance of metastable β titanium alloys usually exhibits another negative $d\rho/dT$ dependence at higher temperatures. Prima et al. related this negative $d\rho/dT$ dependence in Ti-6.8Mo-4.5Fe-1.5Al alloy to progressive vanishing of ω_{iso} through $\omega \rightarrow \alpha$ phase transformation [73, 74]. In their research they compared results of electrical resistance, dilatometry, neutron diffraction and transmission electron microscopy. This is however, in disagreement with our recent work performed on similar metastable β titanium alloy (Ti-15Mo). In the temperature range of the second decrease of resistance

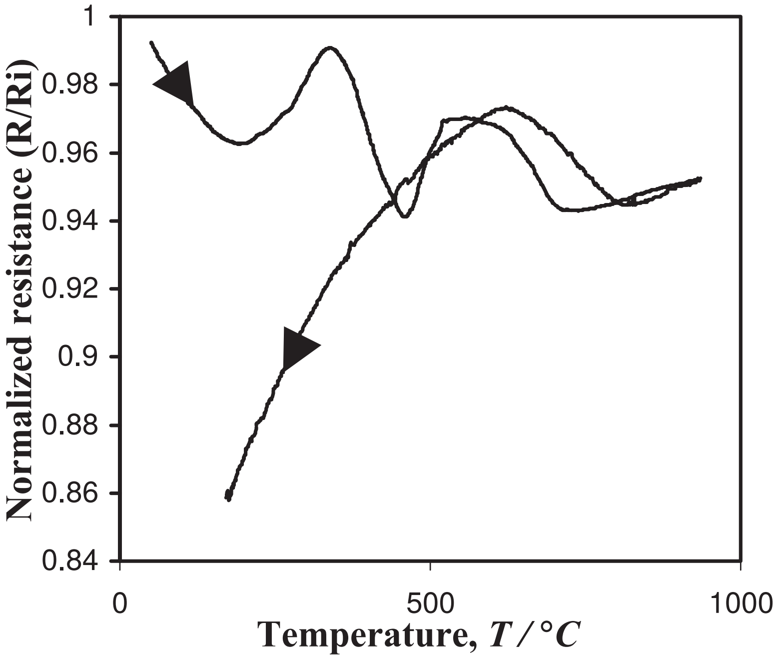

Figure 1.6: Normalized resistivity of quenched LCB Ti during a thermal cycle between 30 °C and 900 °C with $dT/dt = 2\ °\mathrm{C\,min}^{-1}$ [64].

with increasing temperature, we did not detect any α phase in the material and explained this decrease by $\beta \leftrightarrow \omega$ transformation [48].

The research of previously mentioned Prima et al. has dealt with very similar topic as this study. They investigated the evolution of electrical resistance during heating of metastable β titanium alloy (Ti-6.8Mo-4.5Fe-1.5Al - also investigated in this study). The result of their measurement is presented in Fig. 1.6. Even though, the results are much noisier than ours (see chapter 4), the main features (increases and decreases of resistance) are the same. Unfortunately, there are no detailed information about utilized apparatus, which could allow us to discuss difference in obtained data.

It has to be noted, that even thought the resistance measurement is an excellent method for detection of phase transformations in titanium alloys [48, 67–72, 74–76], it is an indirect method and has to be accompanied by other independent measurements (e.g. TEM, XRD, etc.) allowing to interpret correctly the processes occurring in the material.

References

1. C. Leyens and M. Peters, eds.: *Titanium and titanium alloys: fundamentals and applications*. Weinheim : Chichester: Wiley-VCH; John Wiley, 2003, p. 513. isbn: 978-3-527-30534-6. doi: 10.1002/3527602119.
2. C. Hampel: *The Encyclopedia of the Chemical Elements*. Reinhold Book Corporation, 1968. isbn: 978-0442155988.
3. S. Nag: Influence of beta instabilities on the early stages of nucleation and growth of alpha in beta titanium alloys. PhD thesis. The Ohio State University, 2008.
4. G. Lütjering and J. C. Williams: *Titanium*. Engineering Materials, Processes. Springer Berlin Heidelberg, 2007. isbn: 978-3-540-71397-5. doi: 10.1007/978-3-540-73036-1.
5. T. W. Duerig, J. Albrecht, D. Richter and P. Fischer: Formation and reversion of stress induced martensite in Ti-10V-2Fe-3Al. *Acta Metallurgica* **30**(12) (Dec. 1982), 2161–2172. issn: 0001-6160. doi: 10.1016/0001-6160(82)90137-7.
6. url: http://asm.matweb.com/search/SpecificMaterial.asp?bassnum=MTU020 (visited on 10/06/2018).
7. url: https://www.azom.com/article.aspx?ArticleID=1843 (visited on 10/06/2018).
8. url: http://www.matweb.com/search/datasheetText.aspx?bassnum=M1010A (visited on 10/06/2018).
9. url: http://asm.matweb.com/search/SpecificMaterial.asp?bassnum=MQ304A (visited on 10/06/2018).
10. M. Donachie: *Titanium: A Technical Guide*. AMS International, 1988. isbn: 0-87170-309-2.
11. G. Welsch, R. Boyer and E. W. Collings: *Materials Properties Handbook: Titanium Alloys*. ASM International, Dec. 1993. isbn: 978-0-87170-481-8.
12. H. Rosenberg: Titanium alloying in theory and practice. *The Science, Technology and Application of Titanium*. Ed. by R. Jaffee and N. Promisel. Pergamon, 1970, 851–859. isbn: 978-0-08-006564-9. doi: 10.1016/B978-0-08-006564-9.50095-6.
13. D. Banerjee, A. Gogia, T. Nandi and V. Joshi: A new ordered orthorhombic phase in a Ti3Al-Nb alloy. *Acta Metallurgica* **36**(4) (1988), 871–882. issn: 0001-6160. doi: 10.1016/0001-6160(88)90141-1.
14. L. Bendersky, W. Boettinger and F. Biancaniello: Intermetallic Ti-Al-Nb alloys based on strengthening of the orthorhombic phase by ω-type phases. *Materials Science and Engineering: A* **152**(1) (1992). Proceedings of the Second International ASM Conference on High Tempareture Aluminides and Intermetallics, 41–47. issn: 0921-5093. doi: 10.1016/0921-5093(92)90044-2.
15. L. Bendersky, W. Boettinger, B. Burton, F. Biancaniello and C. Shoemaker: The formation of ordered ω-related phases in alloys of composition Ti_4Al_3Nb. *Acta Metallurgica et Materialia* **38**(6) (1990), 931–943. issn: 0956-7151. doi: 10.1016/0956-7151(90)90165-D.
16. J. Šmilauerová: Phase transformations in modern titanium alloys. PhD thesis. Charles University, 2016.

17. J. Williams: Kinetics and Phase Transformations: A Critical Review. *Titanium Science and Technology.* Ed. by R. Jafee and H. Burte. Plenum Press, 1973, 1433–1494.

18. P. D. Frost, W. M. Parris, L. L. Hirsch, J. R. Doig and C. M. Schwartz: Isothermal transformation of titanium-chromium alloys. *Transactions of American Society for Metals* **46** (1954), 231.

19. Y. Zheng et al.: The role of the ω phase on the non-classical precipitation of the α phase in metastable β-titanium alloys. *Scripta Materialia* **111** (Jan. 2016), 81–84. issn: 13596462. doi: 10.1016/j.scriptamat.2015.08.019.

20. Y. Zheng et al.: The indirect influence of the ω phase on the degree of refinement of distributions of the α phase in metastable β-Titanium alloys. *Acta Materialia* **103** (Jan. 2016), 165–173. issn: 13596454. doi: 10.1016/j.actamat.2015.09.053.

21. J. M. Silcock: An X-ray examination of the to phase in TiV, TiMo and TiCr alloys. *Acta Metall* **6**(7) (1958), 481–493. doi: 10.1016/0001-6160(58)90111-1.

22. Y. A. Bagaryatskiy, T. V. Tagunova and G. I. Nosova. *Problem Metalloved. Fis. Metallov. (Problems of Metallography and Metal Physics)* **5** (1958).

23. J. Šmilauerová et al.: Ordered array of ω particles in β-Ti matrix studied by small-angle X-ray scattering. *Acta Materialia* **81** (Dec. 2014), 71–82. issn: 1359-6454. doi: 10.1016/j.actamat.2014.06.042.

24. B. A. Hatt and J. A. Roberts: The ω-phase in zirconium base alloys. *Acta Metallurgica* **8**(8) (Aug. 1960), 575–584. issn: 0001-6160. doi: 10.1016/0001-6160(60)90112-7.

25. S. Banerjee and P. Mukhopadhyay: *Phase transformations: examples from titanium and zirconium alloys.* Pergamon materials series 12. Amsterdam ; Oxford: Elsevier/Pergamon, 2007, p. 813. isbn: 978-0-08-042145-2.

26. S. K. Sikka, Y. K. Vohra and R. Chidambaram: Omega phase in materials. *Progress in Materials Science* **27**(3) (1982), 245–310. issn: 0079-6425. doi: 10.1016/0079-6425(82)90002-0.

27. D. De Fontaine, N. E. Paton and J. C. Williams: The omega phase transformation in titanium alloys as an example of displacement controlled reactions. *Acta Metallurgica* **19**(11) (1971), 1153–1162. issn: 0001-6160. doi: 10.1016/0001-6160(71)90047-2.

28. P. Zháňal et al.: Phase Transformations in Ti-15Mo Investigated by in situ Electrical Resistance. *Acta Physica Polonica A* **128**(4) (2015), 779–783. issn: 0587-4246, 1898-794X. doi: 10.12693/APhysPolA.128.779.

29. J. Nejezchlebová et al.: The effect of athermal and isothermal ω phase particles on elasticity of β-Ti single crystals. *Acta Materialia* **110** (May 2016), 185–191. issn: 1359-6454. doi: 10.1016/j.actamat.2016.03.033.

30. F. Froes and A. I. Staff: *Titanium: Physical Metallurgy Processing and Applications.* ASM International, 2015. isbn: 9781627080798.

31. T. W. Duerig, G. T. Terlinde and J. C. Williams: The ω-Phase Reaction in Titanium Alloy. *Proceedings of the 4th Int'l Conference on Titanium.* Ed. by H. Kimura and O. Izumi. **2**. Titanium‘80 Science & Technology, 1980, 1299–1308.

32. J. Šmilauerová, P. Harcuba, J. Pospíšil, Z. Matěj and V. Holý: Growth of ω inclusions in Ti alloys: An X-ray diffraction study. *Acta Materialia* **61**(17) (Oct. 2013), 6635–6645. issn: 1359-6454. doi: 10.1016/j.actamat.2013.07.059.

33. S. Dubinskiy, A. Korotitskiy, S. Prokoshkin and V. Brailovski: In situ X-ray diffraction study of athermal and isothermal omega-phase crystal lattice in Ti-Nb-based shape memory alloys. *Materials Letters* **168** (Apr. 2016), 155–157. issn: 0167-577X. doi: 10.1016/j.matlet.2016.01.012.

34. J. C. Jamieson: Crystal Structures of Titanium, Zirconium, and Hafnium at High Pressures. *Science* **140**(3562) (1963), 72–73. issn: 0036-8075. doi: 10.1126/science.140.3562.72.

35. A. Bagaryatskiy Yu and I. Nosova G. *Physics of Metals and Metallography* **13**(3) (1962), 92.

36. T. S. Kuan, R. R. Ahrens and S. L. Sass: The Stress-induced omega phase transformation in Ti-V alloys. *Metallurgical Transactions A* **6**(9) (1975), 1767–1774. issn: 0360-2133, 1543-1940. doi: 10.1007/BF02642306.

37. X. Zhao, M. Niinomi, M. Nakai and J. Hieda: Effect of Deformation-Induced ω Phase on the Mechanical Properties of Metastable β-Type Ti-V Alloys. *MATERIALS TRANSACTIONS* **53**(8) (2012), 1379–1384. doi: 10.2320/matertrans.M2012116.

38. Deformation-induced ω phase in modified Ti–29Nb–13Ta–4.6Zr alloy by Cr addition. *Acta Biomaterialia* **9**(8) (2013), 8027–8035. issn: 1742-7061. doi: 10.1016/j.actbio.2013.04.032.

39. Y. Zheng et al.: The effect of alloy composition on instabilities in the β phase of titanium alloys. *Scripta Materialia* **116** (2016), 49–52. issn: 1359-6462. doi: j.scriptamat.2016.01.024.

40. Y. Zheng, R. E. Williams and H. L. Fraser: Characterization of a previously unidentified ordered orthorhombic metastable phase in Ti-5Al-5Mo-5V-3Cr. *Scripta Materialia* **113** (2016), 202–205. issn: 1359-6462. doi: 10.1016/j.scriptamat.2015.10.037.

41. T. W. Duerig and J. C. Williams: Overview: Microstructure and Properies of Beta-Titanium. *Beta-Titanium Alloys in the 1980's*. Ed. by R. R. Boyer and H. W. Rosenberg. The Metallurgical Society of AIME, 1984, 19–69.

42. C. H. Wang et al.: Martensitic microstructures and mechanical properties of as-quenched metastable β-type Ti-Mo alloys. *Journal of Materials Science* **51**(14) (July 2016), 6886–6896. issn: 1573-4803. doi: 10.1007/s10853-016-9976-6.

43. X. Tang, T. Ahmed and H. J. Rack: Phase transformations in Ti-Nb-Ta and Ti-Nb-Ta-Zr alloys. *Journal of Materials Science* **35**(7) (Apr. 2000), 1805–1811. issn: 1573-4803. doi: 10.1023/A:1004792922155.

44. W. Burgers: On the process of transition of the cubic-body-centered modification into the hexagonal-close-packed modification of zirconium. *Physica* **1**(7) (1934), 561–586. issn: 0031-8914. doi: 10.1016/S0031-8914(34)80244-3.

45. H. Beladi, Q. Chao and G. S. Rohrer: Variant selection and intervariant crystallographic planes distribution in martensite in a Ti–6Al–4V alloy. *Acta Materialia* **80** (2014), 478–489. issn: 1359-6454. doi: https://doi.org/10.1016/j.actamat.2014.06.064.

46. P. Wolfgang and S. Angelica: Die Ausscheidungsform des ϵ-Karbids im Ferrit und im Martensit beim Anlassen. *Archiv für das Eisenhüttenwesen* **29**(11) (1958), 715–721. doi: 10.1002/srin.195803018.

47. T. Furuhara et al.: Morphology and Crystallography of α Precipitates in β Ti–Mo Binary Alloys. *Materials Transactions, JIM* **39**(1) (1998), 31–39. doi: 10.2320/matertrans1989.39.31.

48. P. Zháňal et al.: Evolution of ω phase during heating of metastable β titanium alloy Ti–15Mo. *Journal of Materials Science* **53**(1) (Jan. 2018), 837–845. issn: 0022-2461, 1573-4803. doi: 10.1007/s10853-017-1519-2.

49. W. Rong and G. Dunlop: The crystallography of secondary carbide precipitation in high speed steel. *Acta Metallurgica* **32**(10) (1984), 1591–1599. issn: 0001-6160. doi: 10.1016/0001-6160(84)90218-9.

50. M.-X. Zhang and P. M. Kelly: Edge-to-edge matching and its applications: Part I. Application to the simple HCP/BCC system. *Acta Materialia* **53**(4) (2005), 1073–1084. issn: 1359-6454. doi: 10.1016/j.actamat.2004.11.007.

51. D. Potter: The structure, morphology and orientation relationship of V_3N in α-vanadium. *Journal of the Less Common Metals* **31**(2) (1973), 299–309. issn: 0022-5088. doi: 10.1016/0022-5088(73)90165-3.

52. H. Fujiwara, R. Yonezawa and K. Ameyama: Crystallographic Analysis of the Relationship between BCC and HCP Phases in Titanium Alloys by Kikuchi Patterns. *Journal of the Japan Institute of Metals* **62**(9) (1998), 803–811. doi: 10.2320/jinstmet1952.62.9_803.

53. B. S. Hickman: The formation of omega phase in titanium and zirconium alloys: a review. *Journal of Materials Science* **4**(6) (1969), 554–563.

54. D. De Fontaine: Mechanical instabilities in the b.c.c. lattice and the beta to omega phase transformation. *Acta Metallurgica* **18**(2) (1970), 275–279. issn: 0001-6160. doi: 10.1016/0001-6160(70)90035-0.

55. Y. N. Gornostyrev and M. I. Katsnelson: Misfit stabilized embedded nanoparticles in metallic alloys. *Phys. Chem. Chem. Phys.* **17** (41 2015), 27249–27257. doi: 10.1039/C5CP04641F.

56. S. Nag et al.: Novel Mixed-Mode Phase Transition Involving a Composition-Dependent Displacive Component. *Physical Review Letters* **106**(24) (2011). issn: 0031-9007, 1079-7114. doi: 10.1103/PhysRevLett.106.245701.

57. J. Šmilauerová, P. Harcuba, D. Kriegner and V. Holý: On the completeness of the $\beta \to \omega$ transformation in metastable β titanium alloys. *Journal of Applied Crystallography* **50**(1) (Feb. 2017), 283–287. doi: 10.1107/S1600576716020458.

58. J. C. Williams and M. J. Blackburn: The Influence of Misfit on the Morphology and Stability of the Omega Phase in Titanium–Transition Metal Alloys. *Trans. Met. Soc. AIME* **245** (Jan. 1969), 2352–2355.

59. Y. Ohmori, T. Ogo, K. Nakai and S. Kobayashi: Effects of ω-phase precipitation on $\beta \to \alpha$, α" transformations in a metastable β titanium alloy. *Materials Science and Engineering: A* **312**(1) (2001), 182–188. issn: 0921-5093. doi: 10.1016/S0921-5093(00)01891-8.

60. S. Nag et al.: ω-Assisted nucleation and growth of α precipitates in the Ti–5Al–5Mo–5V–3Cr–0.5Fe β titanium alloy. *Acta Materialia* **57**(7) (2009), 2136–2147. issn: 1359-6454. doi: 10.1016/j.actamat.2009.01.007.

61. S. Azimzadeh and H. J. Rack: Phase transformations in Ti-6.8Mo-4.5Fe-1.5Al. *Metall and Mat Trans A* **29**(10) (1998), 2455–2467. issn: 1073-5623, 1543-1940. doi: 10.1007/s11661-998-0217-8.

62. F. Prima, P. Vermaut, G. Texier, D. Ansel and T. Gloriant: Evidence of α-nanophase heterogeneous nucleation from ω particles in a β-metastable Ti-based alloy by high-resolution electron microscopy. *Scripta Materialia* **54**(4) (2006), 645–648. issn: 13596462. doi: 10.1016/j.scriptamat.2005.10.024.

63. T. Li et al.: New insights into the phase transformations to isothermal ω and ω-assisted α in near β-Ti alloys. *Acta Materialia* **106** (Mar. 2016), 353–366. issn: 1359-6454. doi: 10.1016/j.actamat.2015.12.046.

64. J. Debuigne and F. Prima: Growth kinetic model for isothermal omega phase particles in low-cost beta titanium Ti-6.8 Mo-4.5 Fe-1.5 Al alloy. *Materials transactions* **46**(6) (2005), 1433–1435.

65. P. L. Rossiter: *The electrical resistivity of metals and alloys.* Cambridge solid state science series. Cambridge University Press, 1987. isbn: 978-0-521-24947-8.

66. S. L. Ames and D. A. McQuillan: The resistivity-temperature-concentration relationships in the system niobium-titanium. *Acta Metallurgica* **2**(6) (1954), 831–836. issn: 0001-6160. doi: 10.1016/0001-6160(54)90036-X.

67. S. Yoshida and Y. Tsuya: The Temperature Dependence of the Electrical Resistivity of the β-phase Titanium-Molybdenum Alloys. *J. Phys. Soc. Jpn.* **11**(11) (1956), 1206–1207. issn: 0031-9015. doi: 10.1143/JPSJ.11.1206.

68. J. C. Ho and E. W. Collings: Anomalous Electrical Resistivity in Titanium-Molybdenum Alloys. *Physical Review B* **6**(10) (1972), 3727.

69. R. R. Hake, D. H. Leslie and T. G. Berlincourt: Electrical resistivity, Hall effect and superconductivity of some b.c.c. titanium-molybdenum alloys. *Journal of Physics and Chemistry of Solids* **20**(3) (1961), 177–186. issn: 0022-3697. doi: 10.1016/0022-3697(61)90002-6.

70. T. S. Luhman, R. Taggart and D. H. Polonis: A resistance anomaly in beta stabilized Ti-Cr alloys. *Scripta Metallurgica* **2**(3) (1968), 169–172. issn: 0036-9748. doi: 10.1016/0036-9748(68)90219-6.

71. M. A. Hill and D. H. Polonis: Influence of beta phase decomposition on the temperature coefficient of resistivity of titanium alloys. *Journal of Materials Science* **22**(6) (June 1987), 2181–2184. issn: 0022-2461, 1573-4803. doi: 10.1007/BF01132957.

72. S.-y. Komatsu et al.: Aging behaviour of Ti15Mo5Zr and Ti15Mo5Zr3Al alloy up to 573 K. *Materials Science and Engineering: A*. International Symposium on Metallurgy and Technology of Titanium Alloys **213**(1–2) (Aug. 1996), 61–65. issn: 0921-5093. doi: 10.1016/0921-5093(96)10228-8.

73. F. Prima et al.: Nanostructured Metastable β-Titanium Based Alloy. *Journal of Metastable and Nanocrystalline Materials* **13** (2002), 307–314. issn: 1422-6375. doi: 10.4028/www.scientific.net/JMNM.13.307.

74. T. Gloriant et al.: Characterization of nanophase precipitation in a metastable β titanium-based alloy by electrical resistivity, dilatometry and neutron diffraction. *Scripta Materialia* **58**(4) (2008), 271–274. issn: 13596462. doi: 10.1016/j.scriptamat.2007.10.007.

75. F. Sun, F. Prima and T. Gloriant: High-strength nanostructured Ti–12Mo alloy from ductile metastable beta state precursor. *Materials Science and Engineering: A* **527**(16–17) (June 2010), 4262–4269. issn: 0921-5093. doi: 10.1016/j.msea.2010.03.044.

76. F. Prima, J. Debuigne, M. Boliveau and D. Ansel: Control of omega phase volume fraction precipitated in a beta titanium alloy: Development of an experimental method. *Journal of materials science letters* **19**(24) (2000), 2219–2221. doi: 10.1023/A:1006708420478.

2. Aims of the thesis

The main objective of the research presented in this thesis is the detection and characterization of phase transformations occurring in metastable β Ti alloys, primarily in Ti-15Mo alloy, during thermal treatment. These transformations were investigated by electrical resistance and dilatometry measurements, ex-situ and in-situ TEM, X-ray and neutron diffraction. The individual processes occurring in material during thermal treatment will be identified and discussed.

The main objective will be accomplished by the following partial tasks:

- Detection and characterization of phase transformations occurring in metastable β-Ti alloys by several experimental techniques.
- Complete characterization of phase transformation by additional direct experimental methods, as e.g. TEM, XRD and ND.
- Determination of evolution of individual phases during heating.
- Comparison of results obtained by different experimental techniques and an explanation of differences.

3. Material and experimental techniques

3.1 Material

In this research several metastable β titanium alloys were studied: Ti-15Mo, Ti-6.8Mo-4.5Fe-1.5Al, Ti-5Al-5V-5Mo-3Cr, Ti-29Nb-1Fe-0.5Si, Ti-15Mo-3Nb-3Al-0.2Si and Ti-13Cr-1Fe-3Al (the content of alloying elements is given in wt. %). All alloys were solution treated above their β-transus temperature and subsequently water quenched. Mo equivalent was calculated for each alloy from the equation determined in [1] and is shown together with alloy composition in Table 3.1. Brief description and of each alloy follows. Phase transformations in these materials were investigated by electrical resistance and compelmented by dilatometry, TER, XRD and ND. Further investigations by dilatometry, transmission electron microscopy, X-ray and neutron diffractions were carried out on Ti-15Mo alloy. It is a simple binary metastable β alloy, which exhibits variety of phase transformations.

3.1.1 Ti-15Mo

Ti-15Mo (8.1 at. % of Mo) is used mainly for biomedical applications. It was originally developed for the chemical industry to provide a titanium alloy with improved corrosion resistance, low elastic modulus, high strength, good fatigue resistance, and good ductility. High temperature applications were also investigated but thermal handling difficulties and microstructure instability at moderate temperatures prevented the extended use in the aerospace industry [2].

The material was supplied by two different manufacturers (TIMET and Carpenter Technology Corporation). The initial batch was in an unsuitable shape for preparation of single crystals and the manufacturer refused to prepare the material in a convenient shape. As the amount of material from the first batch was insufficient for all experiments the second batch was supplied by another manufactures. Each batch has a slightly different composition, which influences partly the results. In the ”Results” chapter, each batch will be referred to avoid any confusion in the interpretation of results.

3.1.2 Ti-6.8Mo-4.5Fe-1.5Al (LCB)

Timetal LCB is a β titanium alloy invented by TIMET which offers advantages of good cold formability, heat treatability and ductility. This alloy is used in aerospace and formula car applications and competes favourably with the conventional materials like steels. The name LCB, stands for “Low-Cost Beta” [3]. The production cost is lowered to less than 50 % compared to other alloys due to relatively cheap Fe-Mo master alloy. Another cost reduction is performed thanks to good forging and rolling properties of this alloy [4].

Alloy	Mo	Fe	Al	V	Cr	Nb	Si	Mo equivalence
Ti-15Mo	15	-	-	-	-	-	-	8.09
LCB	6.8	4.5	1.5	-	-	-	-	6.82
Ti-5553	5	-	5	5	3	-	-	3.92
TNFS	-	1	-	-	-	29	0.5	6.19
Timetal 21S	15	-	3	-	-	3	0.2	5.50
TCFA	-	1	3	-	13	-	-	11.06

Table 3.1: Compositions of studied alloys in wt. %.

3.1.3 Ti-5Al-5V-5Mo-3Cr (Ti-5553)

Ti-5553 is used in airplanes for structural components such as landing gears or airframe components. This alloy is based on the Ti-alloy VT22 (Ti-4.74Al-5.04V-5.57Mo-0.81Cr-0.98Fe in wt. %). It has an ultimate tensile strength of about 1300 MPa with a nominal density of 4670 kg/m^3. Ti-5553 was aimed to substitute the alloy Ti-10V-2Fe-3Al through developing an alloy with higher strength, less prone to segregation and lower cost [5]. The alloy was produced by VSPMO Tirus Ltd.

3.1.4 Ti-29Nb-1Fe-0.5Si (TNFS)

TNFS is newly developed Nb-based metastable β-Ti alloy with exceptionally low elastic modulus and a high potential in biomedical applications. Combined alloying by Fe and Si leads to higher strength levels. It is reported that an Si content up to 1 wt.% decreases the elastic modulus to 48 GPa, which is quite close to the elastic modulus of cortical bone (10 - 30 GPa). However, this fact is related to the lower concentration of β stabilizing elements which leads to the lower stability of the β phase rather than to an intrinsic effect of Si on the β phase matrix [6]. The alloy was produced by GfE Fremat GmbH.

3.1.5 Ti-15Mo-3Nb-3Al-0.2Si (Timetal 21S)

TIMETAL 21S has a high specific strength, good cold formability and has been designed for a high oxidation resistance, elevated temperature strength, creep resistance, and thermal stability. It is useful for applications between 228 and 593 °C. The alloy has excellent resistance to aircraft hydraulic fluids at all temperatures. TIMETAL 21S is well suited for metal matrix composites, it can be economically rolled to foil, is compatible with most fibers, and sufficiently stable up to 816 °C. The alloy was produced by the same company as the first batch of Ti-15Mo and LCB, TIMET company.

3.1.6 Ti-13Cr-1Fe-3Al (TCFA)

TCFA alloy was developed as an affordable priced titanium-based material for general use. This metastable β titanium alloy contains only inexpensive alloying elements. It posses typical advantages of titanium alloys such as a high specific strength, good cold formability and a high oxidation resistance. The alloy was produced by Daido steel Company Ltd.

3.1.7 Preparation of single crystals

X-ray diffraction experiment was performed on single crystalline Ti-15Mo. Investigation of a single crystal allows to distinguish all 4 crystallographic families of ω and all 12 variants of α phase.

The single crystals were grown in the optical furnace from a rod with diameter of 9 mm. The furnace was evacuated by a turbomolecular pump up to 10^{-6} mbar to avoid oxidation of the titanium alloy. After proper evacuation the quartz chamber was filled with high purity Ar protective atmosphere. At the beginning of each crystal growth, a neck was created in order to isolate one grain. The pulling rate was 10 mm/h and the rotation velocity of both the upper and the lower shaft was 5 rpm. The total length of grown crystals was up to 9 cm. A thorough explanation of the growth process can be found in [7].

3.2 Electrical resistance

Measurements of electrical resistance of the samples were performed employing a self-made apparatus, whose scheme is given in Fig. 3.1.

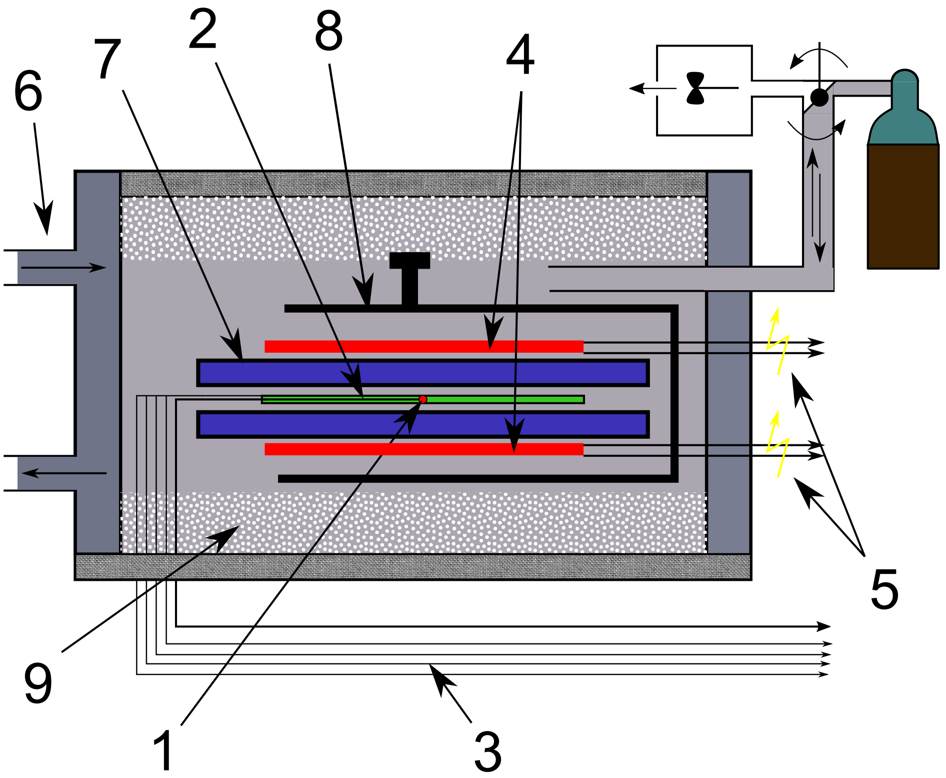

Figure 3.1: Scheme of apparatus employed for electrical resistance measurements: 1 - thermocouple, 2 - sample, 3 - signal lead, 4 - heating coil, 5 - power lead, 6 - water cooling system, 7 - heat basin, 8 - sample holder, 9 - heat barrier.

A four-point methods of electrical resistance measurement was employed. The scheme of electrical circuit of this technique is shown in Fig. 3.2. The two outer probes serve as supply of electrical current, while the voltage is measured between the two inner contacts. As the resistance of the voltmeter is much greater than the resistance of the sample, the current which flows through the voltmeter is negligible compared to the flow through the sample. Thus, the resistance of the voltmeter leads and contacts does affect measured value. The influence of transient and thermoelectric effects, which arise due to different temperatures on the contacts during voltage measurements and on joints of different material is eliminated by calculating the average voltage values measured for current flow in both directions. Due to the setup of this method, the resistance of contact leads and their welds with the sample does not affect the measured electrical resistance. The current is the same at all points in the circuit. As only voltage drop across the sample is measured (and not the wires resistances), the calculated electrical resistance represents solely the resistance of the sample (R_{sample}). The numbers 1 - 4 in Fig. 3.2 label wires, which were welded to respective contacts on the sample (see Fig. 3.3).

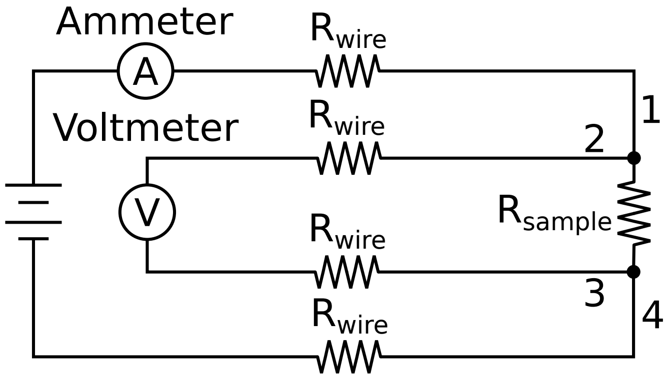

Figure 3.2: Scheme of four-point method.

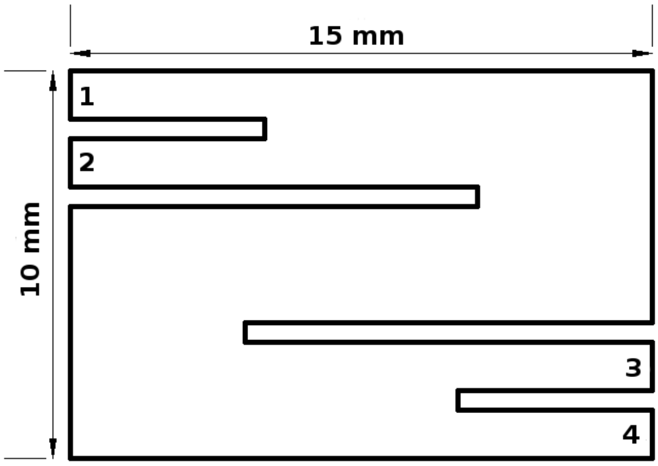

Figure 3.3: Shape of the sample used for electrical resistance measurements.

The voltage was measured simultaneously with the electrical current utilizing nanovoltmeter Keithley 2182 and SourceMeter Keithley 2400 device, respectively, which allows relative measuring error to be less than 10^{-4} at each measured point while acquiring about 2 points per second [8]. There are two heating elements (number 4 in Fig. 3.1). They are placed on top and underneath the sample, respectively. Each heating coil has its own source (Kikusui PAS-40-18), which provide current used for heating. The temperature is measured by K type thermocouple placed in a vicinity of the sample. Measured samples were flat of the thickness slightly less than 1 mm and the size of 15 × 10 mm^2. They were cut to the shape of letter S to increase the effective length of the sample for electric current flow and four contacts were appropriately joined. The samples shape and dimensions are shown in Fig. 3.3.

3.3 Dilatometry

Thermal expansion of the material was studied utilizing Linseis L75 PT vertical dilatometer, which has a dual measuring system (see Fig. 3.4). The apparatus allows to measure length changes of a sample and a reference with a known thermal expansivity or two samples simultaneously.

Dilatometry is a technique for characterizing dimensional changes of a material caused by physical or chemical processes. These processes can be studied as a function of temperature or time. The sample holder is usually in a shape of a tube with a closed end. The sample is in a contact with the end of the tube and a push rod which transfers the length changes of the sample to the measuring system. The spring-loaded push rod applies a constant force to the sample throughout the measurement. The sample holder and the push rod are manufactured from the same material which has a minimal thermal expansivity and does not undergo any phase transitions in the studied temperature range. Fused silica (quartz glass) or Al_2O_3 are the most often used for this application. The length changes of the samples are detected by a linear variable differential transformer (LVDT) sensor which works on the principle of electric transformer with a core. From the dilatometric curve it is possible to analyse temperature and kinetics of phase transformations or to calculate the coefficient of thermal expansion.

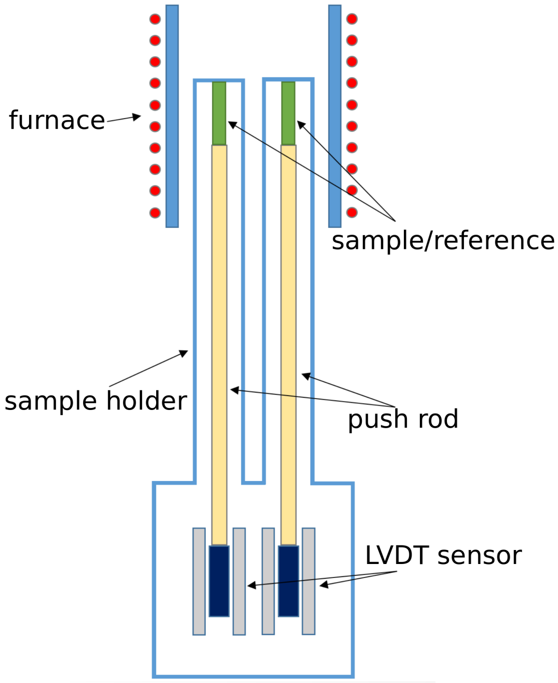

Figure 3.4: Scheme of vertical dilatometer with dual measuring system.

3.3.1 Sample preparation

Cylindrical or prismatical specimens were used. The maximum length is 50 mm and the maximum diameter is 6 mm (cylidrical specimens). Samples should have strictly parallel bases and the main axis perpendicular to them. In order, to prepare samples with desired specifications a special specimen holder was developed. The model of the holder is shown in Fig. 3.5. Parts of the holder are in red, cylindrical sample in blue a prismatical sample in green. The holder may hold two samples simultaneously. The height of the holder is 15 mm, which is 5 mm less than usually used 20 mm long samples. When the samples are fixed in the holder, they stick out on both sides. Then the holder is placed in a cylindrical shell with inner diameter of same size as diameter of the holder. The cylindrical shell secures, that the main axis of the samples is perpendicular to grinding papers during preparation. The bases of the samples are then grinded and polished. After sufficient polishing, the holder is flipped and opposite sample bases are grinded. Such procedure allows to produce two specimens for thermal expansion measurement of required precision/geometry.

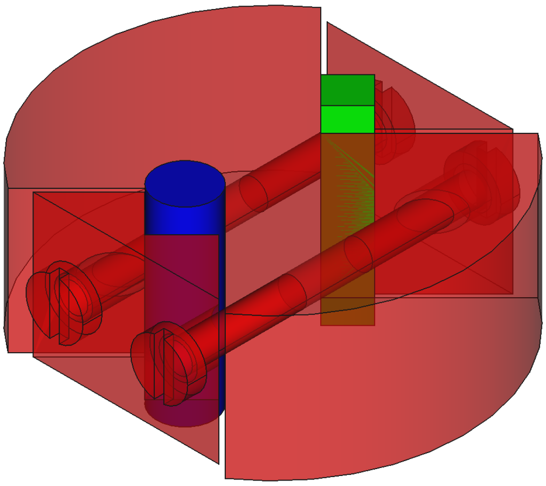

Figure 3.5: Holder for preparation of the samples for thermal expansion measurements.

The most used length of specimens of 20 mm was chosen because of supplied reference specimens are 20 mm long cylinders with the diameter of 6 mm. The samples and the reference are placed in the same height and distance from furnace walls. Measuring with the samples of the same length ensures same the temperature distribution along the samples and references axis. The specimens measured in this study were prisms of 20 mm height with base 4 × 4 mm^2. Prisms were chosen due to their easier preparation with laboratory equipment compared to cylinders.

3.4 X-ray diffraction

When X-rays propagate through a material, the following processes are considered as diffraction [9]:

- Coherent scattering, which produces beams with the same wavelength as the incident (primary) beam.

- Incoherent (Compton) scattering. The wavelength of the scattered beam increases due to partial loss of photon energy in collisions with core electrons (the Compton effect).

- Absorption of the x-rays. Some photons are dissipated in random directions due to scattering, and some photons lose their energy by ejecting electron(s) from an atom and/or due to the photoelectric effect.

Incoherent scattering is generally neglected. Absorption is usually taken into account only when it becomes significant. Thus, in the first approximation only coherent scattering results in the diffraction from periodic lattices. There are two different levels of approximation for the interaction of X-rays (or any other type of radiation with the proper wavelength) with a crystal - kinematical and dynamical theories of diffraction. In the kinematical diffraction, a beam scattered once does not scatter again before it leaves the crystal. Thus, the kinematical theory of diffraction is based on the assumption that the interaction of the diffracted beam with the crystal is negligible, which requires the following assumptions [9]:

1. Crystal consists of individual crystallites, which are slightly misaligned with respect to each other.

2. The size of the crystallites is small.

3. The misalignment of the crystallites is large enough, so that the interaction of x-rays with matter at the length scale exceeding the size of mosaic blocks is negligible.

On the other hand, the theory of the dynamical diffraction accounts for scattering of the diffracted beam and other interactions of waves inside the crystal, and thus the mathematical apparatus of the theory is quite complex. The kinematical approach is simple, and adequately and accurately describes the diffraction of X-rays from crystals [9]. Hence, the kinematical theory of diffraction is used in this thesis.

Diffraction can be observed only when the wavelength is of the same order of magnitude as the repetitive distance between the scattering objects. The most useful way to describe the diffraction of X-rays by a crystal is by the Bragg law [10]. The incident X-rays hit the crystal planes with an incident angle θ and reflection angle θ (see Fig. 3.6a). The diffraction occur when the Bragg condition is satisfied:

$$n\lambda = 2dsin\theta. \tag{3.1}$$

Here n is an integer number, λ is the wavelength, d is the distance between each adjacent crystal planes (d-spacing), θ is the Bragg angle at which one observes a diffraction peak. If a single wavelength is used, the Bragg equation is typically expressed with $n = 1$ because the higher order reflections can be considered as being from different lattice planes. For perfect crystals with perfect instrumentation, the diffraction peak is a delta function as shown in Fig. 3.6b.

The diffracted intensity is denoted by I. A typical diffraction peak is a broadened as displayed in Fig. 3.6b. The peak broadening can be caused by many effects, including imperfect crystal conditions, such as strain, mosaic structure, and finite size; ambient conditions, such as atomic thermal vibration; and instrumental conditions, such as X-ray beam size, beam divergence, beam spectrum distribution, and detector resolution [11]. The total diffracted intensity of a diffracted beam can be determined from the area under the curve, which is referred to as integrated intensity. The integrated intensity is a more consistent value for measuring the diffracted intensity of a reflection since it is less affected by all the peak broadening factors.

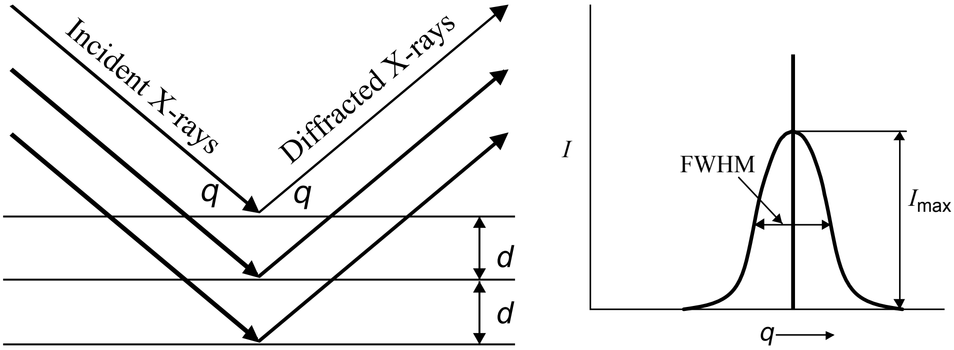

(a) (b)

Figure 3.6: (a) The incident and reflected X-rays. (b) The diffraction peak [11].

X-ray diffraction phenomena can also be explained in reciprocal space by the reciprocal lattice and the Ewald sphere [12]. Reciprocal lattice is a transformation of the crystal lattice in real space to reciprocal space. The shape and size of a unit cell in real space are defined by vectors **a**, **b**, and **c**. The unit cell of the corresponding reciprocal lattice is given by vectors $\mathbf{a}^*$, $\mathbf{b}^*$, and $\mathbf{c}^*$. The relationship between these vectors is shown bellow:

$$\begin{aligned} \mathbf{a}^* &= \frac{1}{V}(\mathbf{b} \times \mathbf{c}), \\ \mathbf{b}^* &= \frac{1}{V}(\mathbf{c} \times \mathbf{a}), \\ \mathbf{c}^* &= \frac{1}{V}(\mathbf{a} \times \mathbf{b}), \end{aligned} \tag{3.2}$$

where V is the volume of the unit cell in the real space. The relationship between the Bragg condition and the reciprocal lattice can be visually explained by the Ewald sphere (see Fig. 3.7). The diffracting crystal is located in the center of the Ewald sphere. The radius of the Ewald sphere is defined as $1/\lambda$. The incident beam and diffracted beam make an angle θ with the crystal lattice palnes (hkl). Initial points of both incident beam vector $\mathbf{S}_0/\lambda$ and diffracted beam vector $\mathbf{S}/\lambda$ are at the center of the sphere and end at points O and P, respectively. The vector from O to P is the reciprocal lattice vector perpendicular to the crystal planes, which can be calculated as $(\mathbf{S} - \mathbf{S}_0)/\lambda$.

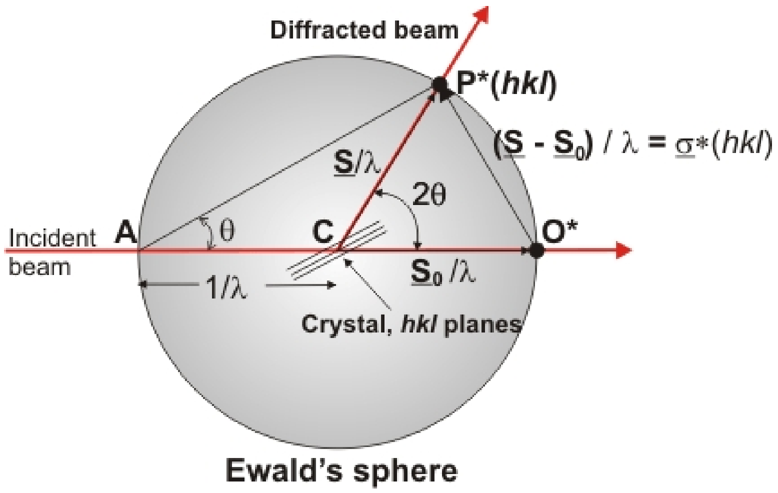

Figure 3.7: The Ewald sphere and Bragg condition in reciprocal space [13].

In a powder diffraction, for a fixed energy of X-ray (or wavelength $E = hc/\lambda$), the diffracted beam takes all directions at a 2θ angle from the incident beam direction (see Fig. 3.8). The diffracted beams form a cone, referred to as diffraction cone, with the incident beam on the rotation axis. In the illustration with the Ewald sphere, the diffraction cone and the diffraction vector cone start from different points. In real space geometry, both the diffraction cone and the diffraction vector cone are considered as starting from the same point (the sample location or instrument center). On the other hand, for a diffraction at single-crystal from a set of crystal planes (hkl), the diffracted beam does not form a cone, it diffracts to exactly one point at the Ewald sphere determined by the incident angle and

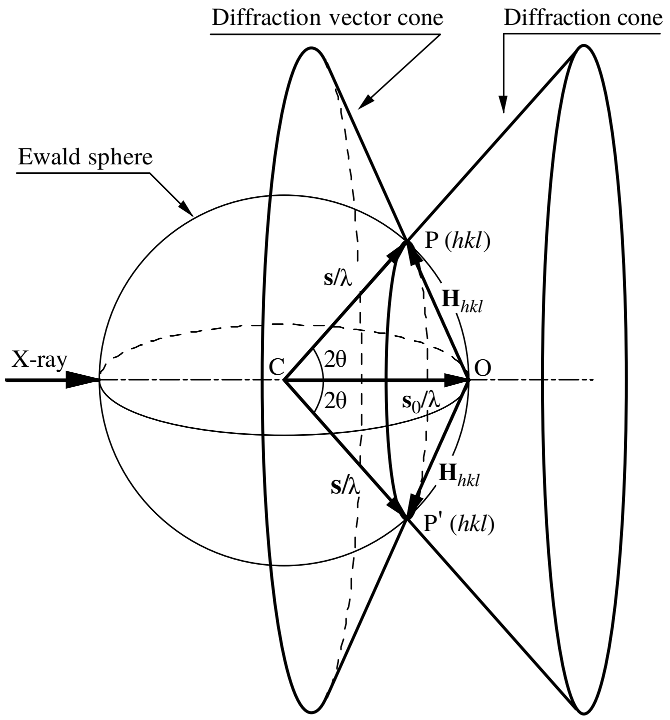

Figure 3.8: Diffraction cone and diffraction vector cone illustrated on the Ewald sphere [11].

d_{hkl}.

X-ray diffraction was measured at the synchrotron ESRF, Grenoble, at the high energy beamline ID11 using photon energy of 60 keV. The diffraction patterns were detected by a two-dimensional CCD detector (FReLoN 2k) with 49×49 μm^2 pixel size. The detector was placed at the distance of 26.6 cm from the sample, perpendicular to the incident beam, which was directed exactly to the center of the detector. A schematic representation of the experimental setup is shown in Fig. 3.9.

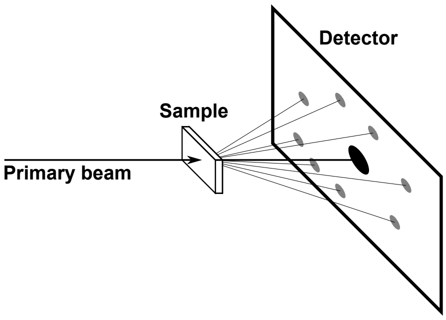

Figure 3.9: Schematic representation of experimental setup.

The signal was acquired in-situ during linear heating with the heating rate of 5 °C/min from room temperature to 660 °C. The acquisition time of a single frame at the beginning of the experiment was 10 s. An oversaturation of the detector caused by an increase of the diffracted intensity due to ongoing phase transformations in the material during heating required a reduction of the exposure time of a single frame to 2 s and later to 1 s. In order to maintain a favorable signal to noise ratio, the reduction of the acquisition time was compensated by a proportional increase of the number of frames, which were summed to obtain the final diffraction pattern (5 and 10 frames for 2 s and 1 s acquisition time, respectively).

The measured intensity was corrected for camera sensitivity, acquisition time and absorption in the sample. The background scattering was subtracted.

3.5 Transmission electron microscopy

A beam of high energy electrons is used in transmission electron microscopy (TEM) for imaging. Focused electron beam interacts with the sample. The electrons diffract on a crystal lattice. Objective lens forms a diffraction pattern in its back focal plane, where an objective aperture can be used to select a direct (bright field) or a diffracted (dark field) beam. The image in the image plane is then formed only by electrons selected by the objective aperture. The resulting image consists of transmitted (not diffracted) and diffracted electrons, which is observed either on a fluorescent screen or CCD camera. Resolution of TEM is of the order 10^{-10} m. Diffraction pattern and Kikuchi lines are formed in the back focal plane of the objective lense (diffraction mode of the microscope). Kikuchi lines are the pairs of lines formed by the Bragg diffraction of diffusely scattered electrons [14]. Using Kichichi lines, the exact local orientation of the specimen may be determined (the direction of the normal to the specimen surface) [15].

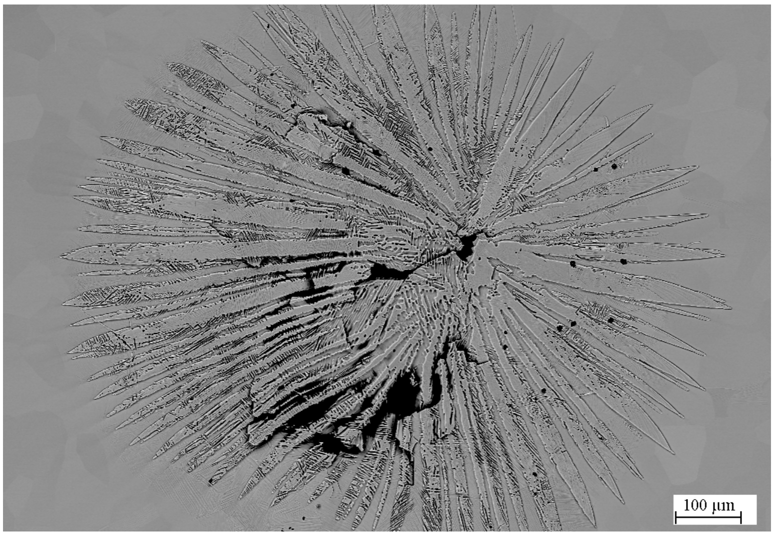

Figure 3.10: Distorted microstructure of the electropolished sample.

For TEM observation, samples in the form of a disc with a diameter of 3 mm with a hole in the middle need to be produced. About 0.15 mm thin plates were prepared using abrasive papers. After that, the discs with the diameter of 3 mm were mechanically punched from the thin plate. Struers Tenupol 5 was initially used to electropolish the specimens. However, during electropolishing of Ti-15Mo alloy distortion of the samples always occured. The distorted structure of the samples is shown in Fig. 3.10. According to [16], the material gets contaminated by hydrogen during electropolishing at low temperatures. The hydrides form inside the material, which results in swelling accompanied by twinning. When the hole appear, the tension in material caused by hydrides and strains around ω particles distorts the sample. After heating up to room temperature, hydrogen evaporates, but the distorted structure remains. The needle-shaped areas clearly visible in Fig. 3.10 probably occurs during creation of hole, due to strains in sample.

In order to prevent distortion of the sample, different technique of sample preparation had to be used. Another set of the samples was prepared by dimple grinding. After the dimpling the samples were subjected to ion milling. Ion milling occurs at room temperature therefore the distortion of thin areas due to the hydrides formation is avoided. However, the force exerted by the dimpling tool causes α phase to form. The microstructure of the material prepared in a described way is shown in Fig. 3.11a. White lines are result of topographic contrast caused by ion milling. The dark bands are colonies of α precipitates formed during dimple grinding. Detail of the dark strips, which contains rod-like α precipitates, is presented in Fig. 3.11b.

In order to avoid the formation of both mentined artefacts, a two-step method of thin foil preparation was employed: electropolishing followed by ion-milling. Initially, the samples were electropolished without penetration, which resulted in not distorted microstructure shown in Fig. 3.12a. The first sample of each batch was used to determine time needed for the penetration. Electropolishing of the others was stopped few seconds before reaching this time. The hole was made by ion polishing at room temperature. The tension in the material is lower at this

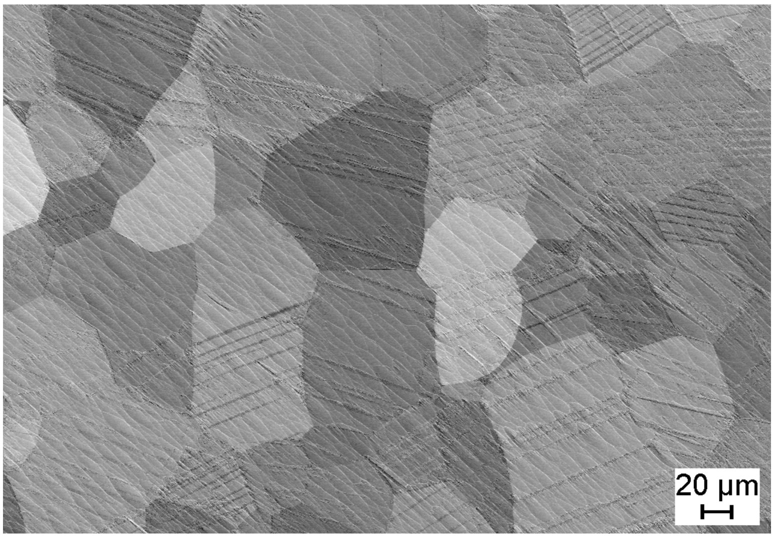

(a) Microstructure of the material after dimple grinding and ion milling.

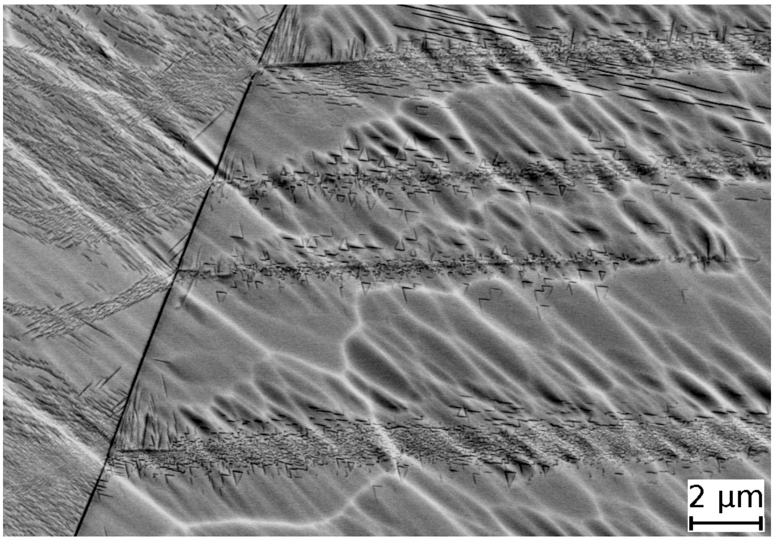

(b) Detailed microstructure of the material after dimple grinding and ion milling.

Figure 3.11: Distorted microstructure of the material due to dimple grinding and ion milling.

temperature, because there should not be any hydrides present. Moreover the amount of ω_{ath} particles should decrease after heating up to room temperature, which decrease strains in the material to a level, at which the material does not distort when the hole appears. This can be seen in Fig. 3.12b, where the microstructure of material prepared in such way is shown. The last preparation procedure was found as the most fitting and was used to prepare all TEM samples observed in this study.

Another possibility of the samples preparation is by utilizing focused ion beam milling in scanning electron microscope, which could provide TEM lamella of site specific locations. However, such procedure is highly time consuming and therefore this method was avoided.

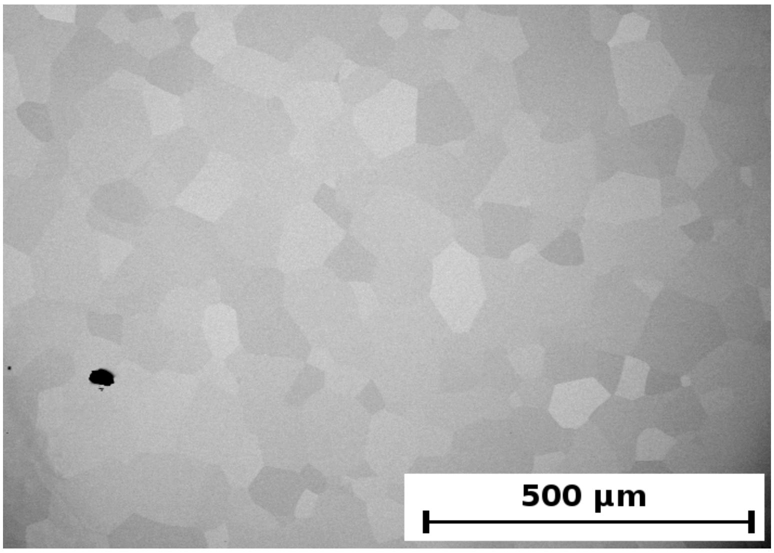

(a) Microstructure of the material after electropolishing without penetration.

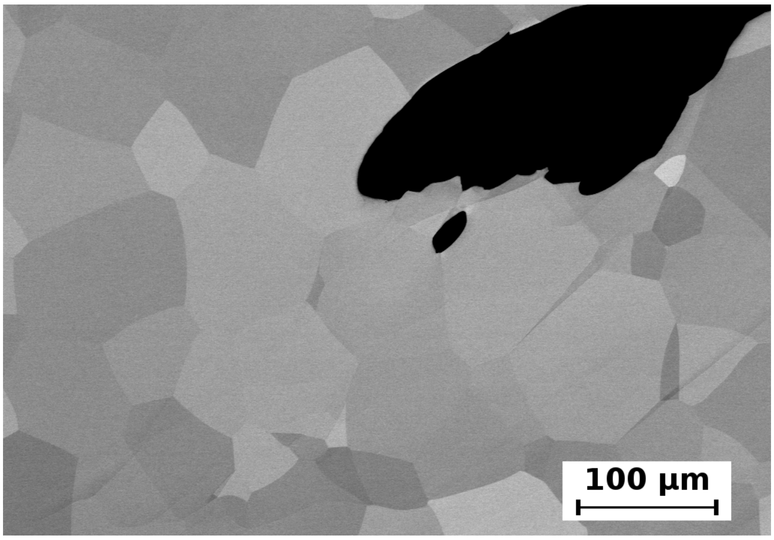

(b) Microstructure of the electropolished material penetrated by ion milling.

Figure 3.12: Non-distorted microstructure of the electropolished material penetrated by ion milling.

The prepared samples were mounted on one of holders which allow either double tilt or heating (for in-situ observations). The observations were performed on JEOL 2200FS microscope with an accelerating voltage of 200 kV.

3.6 Neutron diffraction

The basic principle of neutron diffraction is the same as that of X-ray or electron diffraction. There are several disadvantages of neutron diffraction comparing to the X-ray or electrons. The neutron sources are not so easily available (spallation source, nuclear reactor), as X-ray devices or TEMs. The intensity of neutron diffraction, even with the most powerful sources, is lower than that for the X-rays. Moreover, the effective cross-section for neutrons is highly inferior to that of X-rays. That leads to the higher acquisition time during the neutron diffraction measurements. On the other hand, the main advantages of neutron diffraction are a large penetration depth, no radiation damage, the high sensitivity to light atoms and the ability to distinguish isotopes. The penetration depth of thermal neutrons is in order of centimeters. Thermal neutrons have the Maxwell-Boltzmann distribution of energies. In order to get the monochromatic beam, it is necessary to use a monochromator.

The neutron diffraction experiments were performed at the Institut Laue-Langevin (ILL), Grenoble, France, at the instrument D20 with extremely high neutron flux utilizing the neutrons with the wavelength of 1.54 Å. The detector at D20 covers a scattering range of 153.6 °, and allows to obtain the diffraction pattern in a range of seconds as a function of temperature, pressure or other parameters. The scheme of the instrument is shown at Fig. 3.13. The thermal neutron beam from the reactor is divided into two parallel beams, one for D2B, the other for D20. The D20 beam first reaches one of its four monochromators. The monochromatic beam leaves the monochromator shielding by one of its five take-off ports, each offering a different instrument resolution. It then reaches the sample (usually a cylinder of powder in a furnace or in a cryostat) which diffracts it in many directions. The diffracted beams are simultaneously counted by the large microstrip multidetector. The counts are accumulated during a certain time to give a powder diffraction pattern with a suitable intensity [17].

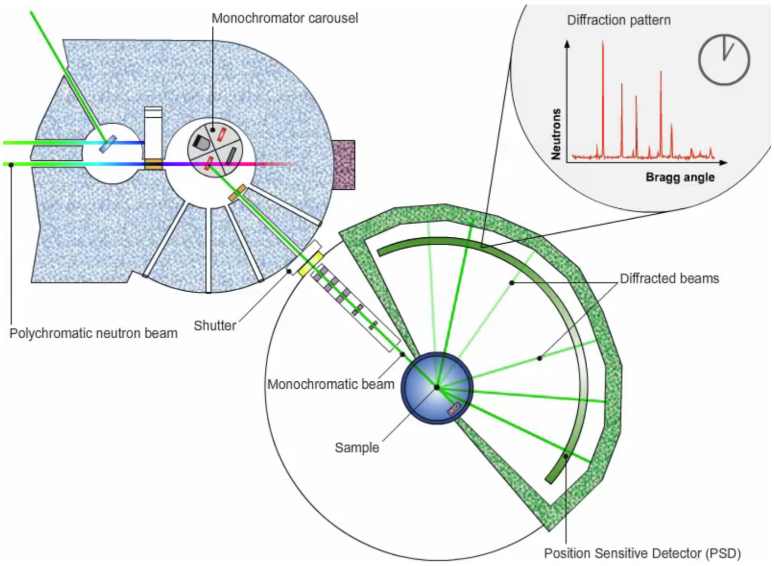

Figure 3.13: Layout of the instrument D20 [17].

Three experiments were performed. During the first measurement, linear heating with the heating rate of 1.875 °C/min up to 850 °C was utilized (the best approximation of the heating rate that was used during measurement of evolution of elastic constants of Ti-5553 in [18]). The the signal was also acquired during cooling with rate of 5 °C/min down to 160 °C. For the second experiment both heating and cooling rate of 5 °C/min was utilized. The maximum reached temperature was again 850 °C. The sample studied in the third experiment was heated up to 450 °C with the heating rate of 1.875 °C/min and aged at this temperature for 7 h and 10 min. The ageing was followed by cooling to 150 °C. The acquisition time of a single spectra was 32 s for heating rate of 1.875 °C/min (one pattern per K) and 30 s for heating (cooling) rate of 5 °C/min. During ageing the acquisition time was set to one minute.

References

1. Q. Wang, C. Dong and P. K. Liaw: Structural Stabilities of β-Ti Alloys Studied Using a New Mo Equivalent Derived from $[\beta/(\alpha+\beta)]$ Phase-Boundary Slopes. *Metallurgical and Materials Transactions A* **46**(8) (Aug. 2015), 3440–3447. issn: 1543-1940. doi: 10.1007/s11661-015-2923-3.
2. J. Disegi: *Implant Materials. Wrought Titanium –15% Molybdenum.* Synthes, 2009.
3. J. Šmilauerová: Phase transformations in modern titanium alloys. PhD thesis. Charles University, 2016.
4. P. J. Bania: Beta titanium alloys and their role in the titanium industry. *JOM* **46**(7) (July 1994), 16–19. issn: 1543-1851. doi: 10.1007/BF03220742.
5. H. Schwab et al.: Processing of Ti-5553 with improved mechanical properties via an in-situ heat treatment combining selective laser melting and substrate plate heating. *Materials & Design* **130** (2017), 83–89. issn: 0264-1275. doi: https://doi.org/10.1016/j.matdes.2017.05.010.
6. I. Kopova et al.: Newly developed Ti–Nb–Zr–Ta–Si–Fe biomedical beta titanium alloys with increased strength and enhanced biocompatibility. *Materials Science and Engineering: C* **60** (2016), 230–238. issn: 0928-4931. doi: https://doi.org/10.1016/j.msec.2015.11.043.
7. J. Šmilauerová, J. Pospíšil, P. Harcuba, V. Holý and M. Janeček: Single crystal growth of TIMETAL LCB titanium alloy by a floating zone method. *Journal of Crystal Growth* **405** (Nov. 2014), 92–96. issn: 0022-0248. doi: 10.1016/j.jcrysgro.2014.07.050.
8. M. Hájek, J. Veselý and M. Cieslar: Precision of electrical resistivity measurements. *Materials Science and Engineering: A*. International Symposium on Physics of Materials, 2005 **462**(1–2) (July 2007), 339–342. issn: 0921-5093. doi: 10.1016/j.msea.2006.01.175.
9. V. Pecharsky and P. Zavalij: *Fundamentals of Powder Diffraction and Structural Characterization of Materials, Second Edition.* 2nd ed. Springer US, 2009. isbn: 978-0-387-09578-3.
10. W. H. Bragg and B. A. WL Bragg: The reflection of X-rays by crystals. *Proc. R. Soc. Lond. A*. Vol. 88. The Royal Society, 1913, pp. 428–438. doi: 10.1098/rspa.1913.0040.
11. B. B. He: *Two-Dimensional X-Ray Diffraction.* John Wiley & Sons, Inc., 2009, p. 443. isbn: 9780470502648. doi: 10.1002/9780470502648.
12. P. P. Ewald: Introduction to the dynamical theory of X-ray diffraction. *Acta Crystallographica Section A* **25**(1) (Jan. 1969), 103–108. doi: 10.1107/S0567739469000155.
13. *Crystallography. Experimental diffraction. Evaluating the diffraction pattern.* url: http://www.xtal.iqfr.csic.es/Cristalografia/parte_06_2-en.html (visited on 01/06/2018).
14. S. Kikuchi: Further Study on the Diffraction of Cathode Rays by Mica. *Proceedings of the Imperial Academy* **4**(6) (1928), 275–278.
15. J. Veselý: *Nanoscale AFM and TEM Observations of Elementary Dislocation Mechanisms.* Springer International Publishing, 2017, p. 100. isbn: 978-3-319-48302-3. doi: 10.1007/978-3-319-48302-3.

16. G. M. Pennock, H. M. Flower and D. R. F. West: The thinning transformation in β Ti-Mo alloys. *Metallography* **10**(1) (Feb. 1977), 43–53. issn: 0026-0800. doi: 10.1016/0026-0800(77)90042-8.

17. url: https://www.ill.eu/users/instruments/instruments-list/d20/description/instrument-layout/ (visited on 18/06/2018).

18. J. Nejezchlebová et al.: On the complementarity between resistivity measurement and ultrasonic measurement for in-situ characterization of phase transitions in Ti-alloys. *Journal of Alloys and Compounds* **762** (2018), 868–872. issn: 0925-8388. doi: https://doi.org/10.1016/j.jallcom.2018.05.173.

4. Results and discussion

The methods introduced in the previous chapter were used to accomplish the aims of this work. This chapter is divided into individual parts in which the results of each experimental method are presented. Initial condition of each alloy corresponds to solution treatment of each respective material above β-transus for 4 hours followed by water quenching.

4.1 Electrical resistance measurement

All measurements in Electrical resistance section were repeated several times to make sure that the obtained results are correct. In all cases, the results did not deviate from each other up to the temperature of about 700 °C. Above that the oxidation rate varies between individual measurements due to inability to ensure the same levels of oxygen in each measurement and due to different time the samples spent at these temperatures with respect to heating rate.

The first method used to investigate phase transformations occurring in Ti-15Mo, was in-situ electrical resistance measurement. The record of of the typical measurement of solution treated Ti-15Mo during heating with heating rate of 5 °C/min from RT to 850 °C is shown in Fig. 4.1.

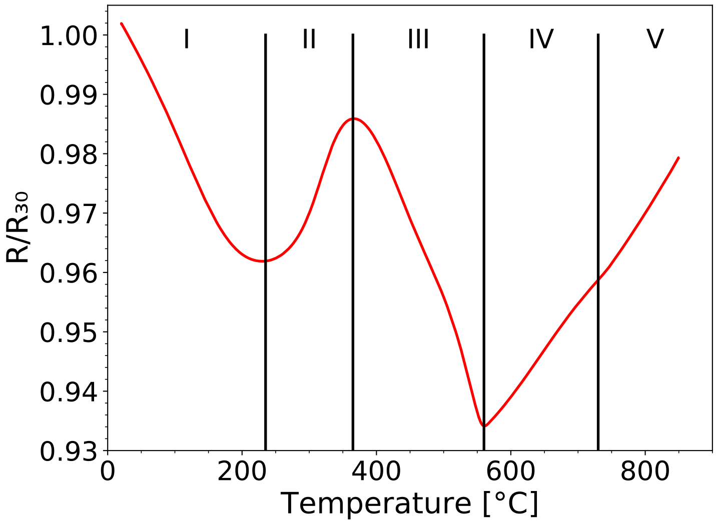

Figure 4.1: The evolution of electrical resistance of Ti-15Mo alloys during heating with the heating rate of 5 °C/min.

The absolute electrical resistivity value of the material cannot be determined with sufficient accuracy due to a complex shape of the sample required for the measurement (see Fig. 3.3). The efficient length and efficient cross-section of the conductor cannot be estimated with accuracy required to determine the electrical resistivity correctly. Therefore, only relative changes of the electrical resistance during heating provide meaningful information about undergoing processes in the material. The relative electrical resistance is calculated by dividing the measured electrical resistance of the sample by some reference electrical resistance measured for the same sample, typically the resistance of the sample measured around room temperature, i.e. R/R_{30}. The comparison of relative electrical resistance evolution of two different samples is substantiated only if these two reference values correspond to the same microstructural condition and phase composition (and, of course, the same temperature). Only under this assumptions the normalization by the value R_{30} rules out the shape factor of the sample. On the other hand, even though the initial condition of all studied materials consists of β phase matrix and small ω particles, the normalization for different materials allows only comparison of relative changes of the electrical resistance. It does not mean that the real value of electrical resistivity of those materials at room temperature is always the same.

The solid red line in Fig. 4.1 corresponds to the electrical resistivity evolution of Ti-15Mo. One can easily distinguish, that the electrical resistance dependence on temperature is not linear, which is a typical behaviour of metals. Several stages corresponding to the monotonous increase and/or decrease of the resistance can be identified. Hypotheses of the occurring processes and their influence on the electrical resistivity of Ti-15Mo alloy in each stage will be discussed in following paragraphs. Additional experiments were employed to verify these assumptions.

At low temperatures (RT-230 °C) - **stage I** - the decrease of electrical resistance with increasing temperature was observed. This can be attributed to the dissolution of ω_{ath} phase. In the vicinity of the coherent β/ω interface, the elastic strain field is formed which acts as the scattering zone for conducting electrons [1]. Therefore, during the dissolution of ω_{ath} phase particles, the elastic strain fields are released, which clears the matrix for electron drift. This results in the decrease in conduction electron scattering and therefore to the electrical resistance drop.

In **stage II** (230 - 365 °C) the resistance increases with increasing temperature. In this temperature range, particles, referred to as ω_{iso}, grow due to diffusion-driven chemical stabilization [7]. This process should be accompanied by the increasing amount of β/ω interfaces, and therefore the electrical resistivity increases [2]. Note that the electrical resistivity also partly increases during heating due to electron-phonon scattering.

In **stage III** (365 - 560 °C) the electrical resistance declines with increasing temperature. The main reason is the decreasing volume fraction of semicoherent ω_{iso} particles. This can be caused either by precipitation of α particles [2] (sometimes referred to as α-nano [3]) or simply by dissolution of ω_{iso} particles back to β matrix due to lower stability of the ω phase in this temperature range [4]. The dilatometry measurements were also able to detect changes of thermal expansion at these temperatures [5].

In **stage IV** (560 - 730 °C), α particles precipitate and grow directly in β matrix [2]. The volume fraction of α phase increases until it starts to decrease towards the β-transus temperature that was found to be around 730 °C. This agrees well with the β-transus temperature given in the binary equilibrium phase diagram of TiMo system [6].

Stage V (T > 730 °C) is located above β-transus temperature, where the electrical resistance increases due to electron-phonon interactions.

4.1.1 Effect of different chemical composition of Ti-15Mo

The comparison of electrical resistance evolution of two Ti-15Mo alloys supplied by different manufacturers is presented in Fig. 4.2. The red curve in Fig. 4.2 is the same as shown in Fig. 4.1. Composition of both materials satisfies the standard [7] shown in Table 4.1. One can see, however, that even small changes in chemical composition within the standard affect the processes occurring in the material. The first minimum and maximum of blue line are shifted both in the temperature and the resistance. Even though the differences are small, they are not negligible. Most of the electrical resistance measurements were performed at the alloy marked as 1 in Fig. 4.2, which will be addressed as Ti-15Mo in electrical resistance and dilatomery sections. On the other hand, type 2 alloy was used for preparation of single-crystals for diffraction experiments. In order to emphasize the differences between these materials and to prove the reproducibility of measurements, the record of remeasured electrical resistance of type 1 alloy with the same heating rate up to 550 °C is plotted in Fig. 4.2 as the green line.

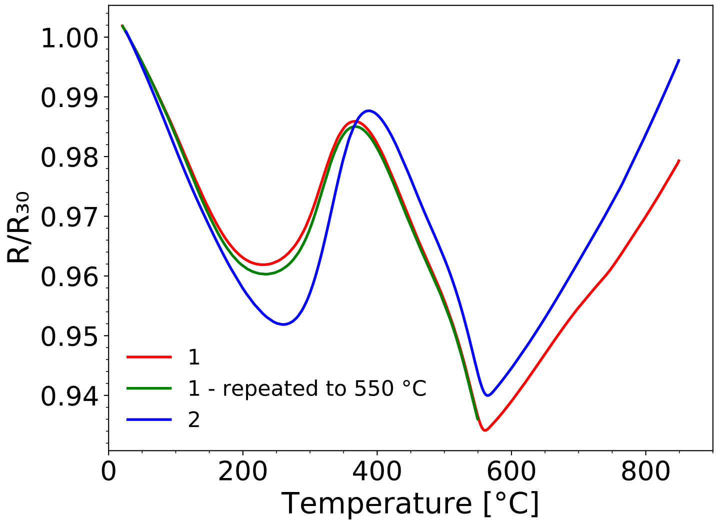

Figure 4.2: The comparison of electrical resistance trend of two Ti-15Mo alloys during heating with heating rate of 5 °C/min.

Element	Ni	C	H	Fe	O	Mo	Ti
Wt. %	<0.05	<0.1	<0.015	<0.1	<0.2	14.0-16.0	Balance

Table 4.1: Composition limits of the Ti-15Mo alloy [7].

4.1.2 Effect of heating rate

The effect of heating rate on processes occurring during heating was studied in three alloys LCB, Ti-15Mo and Ti-5553 (in Appendices A).

Ti-15Mo

Comparison of electrical resistance of Ti-15Mo during heating with different heating rates is shown in Fig. 4.3.

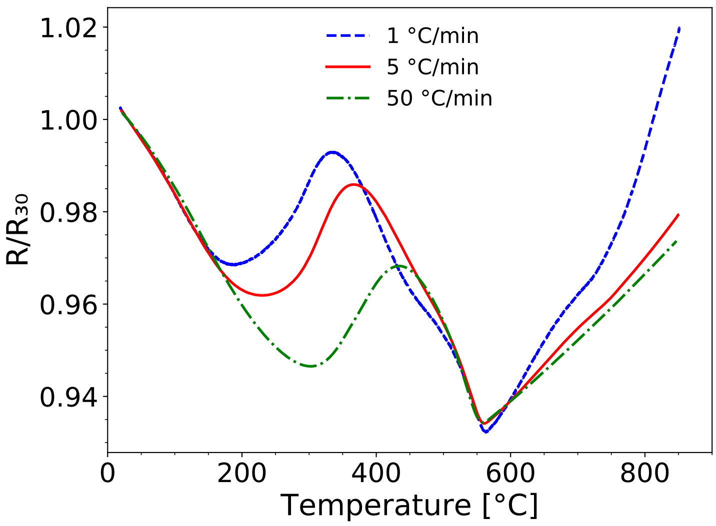

Figure 4.3: The electrical resistance of Ti-15Mo during heating with different heating rates.

The comparison of different heating rates in Fig. 4.3 shows shifts of the first local minimum and maximum of resistance curves to higher temperatures with increasing heating rate. For heating rates of 1, 5 and 50 °C/min the first minima are at 190, 225 and 300 °C, respectively; while the respective maxima are at 335, 365, 435 °C. These shifts indicate that diffusion controlled processes, which affect the electrical resistance, occur in the material. On the other hand, the abrupt change in the monotonicity at 560 °C does not depend on the heating rate. The authors in [8] claim that this sharp minimum in the relative resistance corresponds to the return of the microstructure towards equilibrium in $\alpha + \beta$ domain. However, all α phase related transformations should be also a diffusion controlled processes and therefore the independence of the heating rate is rather surprising.

During further heating ($T > 560$ °C) the resistance increases and the concentration of α phase first increases to reach an equilibrium and then close to β-transus α phase concentration decreases again. Above β-transus (about 730 °C) α phase dissolves completely. The precipitation of α phase is diffusion controlled process, therefore, it strongly depends on the heating rate. The volume fraction of (newly) formed α phase increases with decreasing heating rate. The high amount of α phase precipitated during the experiment with the slowest heating rate of 1 °C/min exhibits the higher increase of the electrical resistance above 600 °C compared to both other measurements and the subsequent dissolution of α phase causes a small bump of the electrical resistance at about 730 °C. The different evolution of the dashed blue curve at the highest temperatures is caused by enhanced oxidation of the sample as it was exposed to these temperatures (T > 700 °C) for the longest time.

LCB

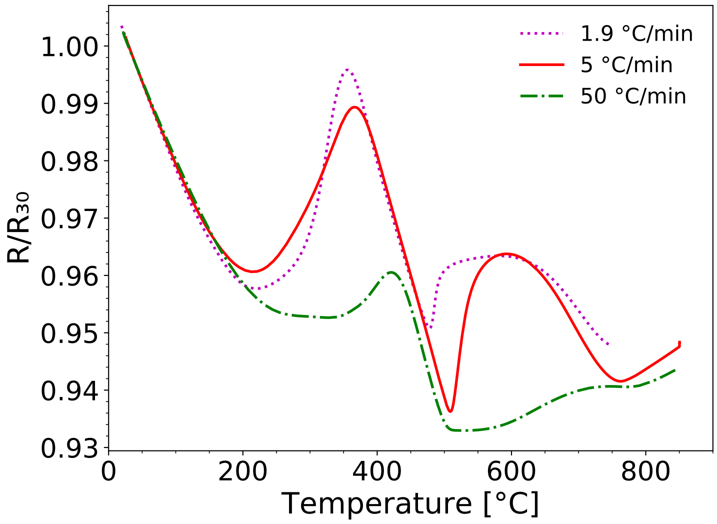

Figure 4.4: The electrical resistance LCB during heating with different heating rates.

The comparison of influence of heating rate on evolution of electrical resistance of LCB alloy is presented in Fig. 4.4. The LCB alloy is affected by different heating rates in a slightly different way than Ti-15Mo. Unlike in the Ti-15Mo alloy, the first minimum of the electrical resistance of LCB alloy is reached approximately at the same temperature ($\sim$ 200 °C) for two slowest heating rates with slighly lower value of the electrical resistance at the lowest heating rate. This could be caused by smaller difference of the heating rates than in case of Ti-15Mo measurements or by interactions of alloying elements, which cannot occur in binary Ti-15Mo alloy. Moreover, the sharp minimum is shifted by 30 °C (480 and 510 °C for 1.9 and 5 °C/min, respectively). This shift is probably caused by higher diffusivity of other alloying elements in β phase (Fe: $D_0 = 1.2\times10^{-7}$ m^2/s [9], Al: $D_0 = 3.9\times10^{-5}$ m^2/s [10]) compared to molybdenum ($D_0 = 1.1\times10^{-15}$ m^2/s [11]), which results in the shift of the sharp minimum to lower temperatures during heating with the heating rate of 1.9 °C/min. This minimum in Ti-15Mo (probably also in other β titanium alloys) indicates the stability limit of ω phase, as reported in [12].

On the other hand, for the heating rate of 50 °C/min, the second minimum occurs at the same temperature as for the heating rate of 5 °C/min.

The inrease of the electrical resistance above 480 and 510 °C (for heating rates of 1.9 and 5 (50) °C/min, respectively) is probably caused by $\beta \rightarrow \alpha$ transformations coupled with thermal increase of electrical resistivity due to lattice vibrations and oxidation of the material [12]. During further heating the resistance drops probably due to the decrease of the concentration of α phase close to β-transus. Due to $\beta \leftrightarrow \alpha$ transformation being diffusion controlled, this bump (maximum at 590 °C for the heating rate of 5 °C/min) is the lowest for the fastest heating rate. This testifies that the amount of precipitated α phase was the lowest in this case.

4.1.3 Single-crystals vs. polycrystals

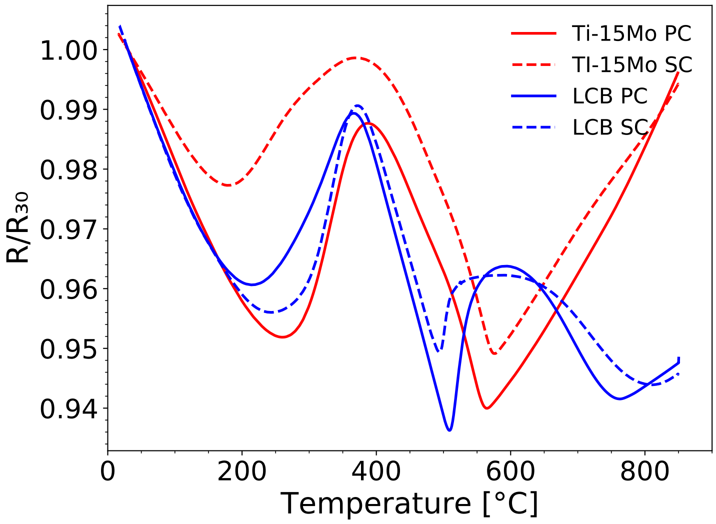

Figure 4.5: The evolution of electrical resistance of Ti-15Mo alloy during heating with heating rate of 5 °C/min.

Single-crystals, subsequently investigated by diffraction experiments, were prepared from LCB and Ti-15Mo alloys. The comparison of evolution of electrical resistance during heating with the heating rate of 5 °C/min between single-crystals and polycrystals of these alloys is presented in Fig. 4.5. On the other hand, the electrical resistance of as-grown single-crystal of LCB (cooled down in the optical furnace it was grown) compared to ST single-crystal of the same alloy in Fig. 4.6. Note that chemical composition of single-crystals slightly differs from precursor polycrystalline materials [13]. The content of oxygen and nitrogen is slightly higher single-crystals of both alloys. Atoms of nitrogen and oxygen are α stabilizing and consequently the β-transus temperature is shifted to higher temperatures in both cases. Moreover the LCB single-crystal has a lower content of strongly β stabilizing iron (3.4 at.% instead of 3.7 at.%), which probably evaporates during single-crystal preparation. Therefore, differences between polycrystalline material and single-crystals might be attributed not only to effect of grain boundaries, but also to different chemical composition. The first minima in Ti-15Mo single-crystal (i.e. the beginning of ω_{iso} formation) is shifted to lower temperature in comparison with the polycrystalline material. The position of the first local maximum is the same for both Ti-15Mo samples. Sharp local minimum is shifted from 560 °C in the polycrystalline sample to 575 °C in the single-crystal. This effect is probably caused by different oxygen and nitrogen concentrations.

In the single-crystal grown from LCB alloy, the upper limit of reversible ω_{ath} transformation is shifted to a higher temperature. The position of the first local maximum is also very similar for both samples. Contrary to Ti-15Mo alloy, the sharp local minimum indicating the stability limit of ω phase particles of LCB single-crystal is shifted to a lower temperature from 510 °C to 495 °C.

A difference between the electrical resistance of the solution treated and ”as-grown” (i. e. not solution treated) LCB single-crystal can be observed in Fig. 4.6.

The as-grown crystal consists of α, β and ω phases at room temperature, which causes different development of resistance at low temperatures (bellow 500 °C). The increase of the electrical resistance of as-grown material above 500 °C is attributed to complete dissolution of ω phase and onset of $\beta \to \alpha$ transformation. The electrical resistance of the as-grown crystal undergoes very significant change between two measured points, i. e. during less than 1 second (see the inset in 4.6). This suggests a martensitic character of this phase transformation. The change of the electrical resistance of ST single-crystal at this temperature is broader, which indicates that o transformation is slower and occurs at a wider temperature range. The slower rate of transformation in ST material and lower start temperature could be due to formation of mosaic blocks, which occurred in the material during solution treating followed by water quenching. The presence of the mosaic blocks implies more dislocations, which could serve as preferential nucleation sites for α phase, which allows progressive forming of α precipitates.

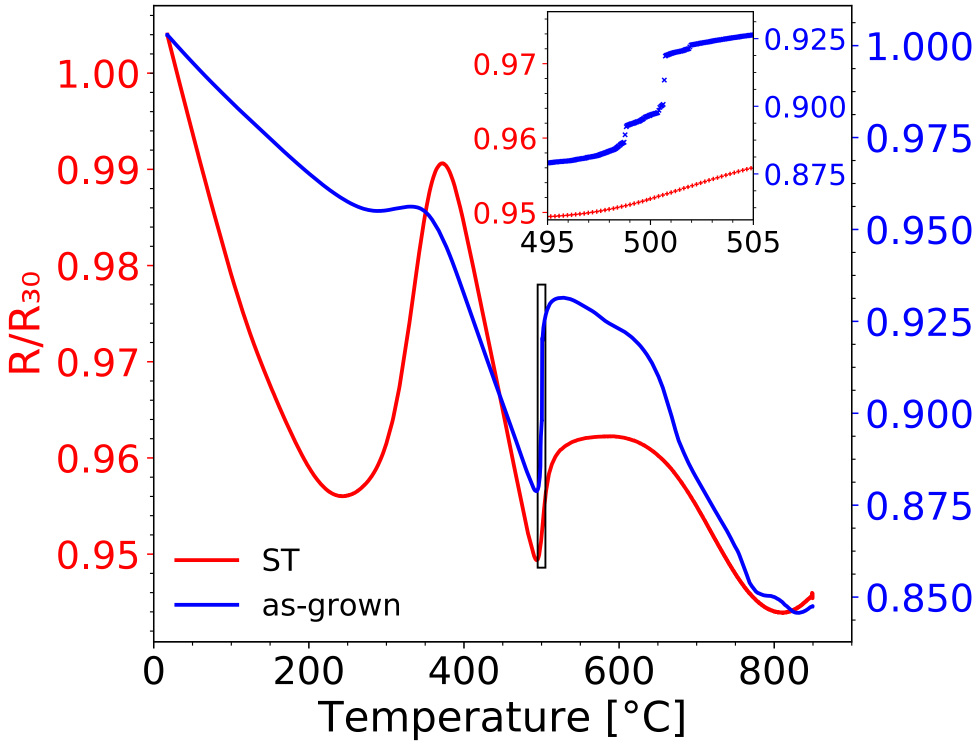

Figure 4.6: The dependence of electrical resistance on temperature during heating with the heating rate of 5 °C/min of ST and as-grown LCB single-crystal. The rectangle denotes area enlarged in inset where all measured points are plotted (spacing 1 s).

4.1.4 Summary of electrical resistance results

The electrical resistance of several metastable β titanium was measured during linear heating. The influence of different chemical composition and the heating rate was discussed. Also course of the electrical resistance evolution with temperature in SC a PC was compared. Finally, the effect of different initial condition (ST vs. as grown material) was studied.

The comparison of the electrical resistance of several metastable β-Ti alloys is presented in Appendices B.

The dependence of electrical resistance on temperature of all studied metastable β alloys exhibits temperature regions in which the resistance increases with increasing temperature. The electrical resistivity of metals typically increases with increasing temperature due to lattice vibrations, the significant drops observed in investigated alloys are caused by ongoing phase transformations.

Other remarkable feature of resistance curves of several of studied materials (LCB, Ti-15Mo, TNFS) is a sharp minimum (observed between 500 and 600 °C), which is related to the stability limit of ω and the onset of α formation. This minimum does not or only slightly depends on heating rate. Similar feature was observed for Ti-5553 alloy as small bump. Due to Ti-15Mo being the simplest system of above mentioned alloys, other experiments were performed using this material. We assume that the conclusions deducted for this alloy can explain similar behaviour of other metastable β titanium alloys.

Figs. 41, 42 and 43 clearly show effect chemical composition on electrical resistance of metastable β titanium alloy. Our results indicate, that even small changes in materials composition could cause distinct effects (cf. Fig. 4.2).

4.2 Dilatometry

The evolution of thermal expansion of the Ti-15Mo was measured in-situ during linear heating with the heating rates of 1, 5 and 20 °C/min up to 850 °C. The results of all measurements of thermal expansion are shown in Fig. 4.7. All curves deviate from linearity for all heating rates. The deflection is shifted to higher temperatures for faster heating rates. Between 300 - 400 °C the material starts to expand faster, up to about 560 °C, where the curves return to linearity up to 850 °C.

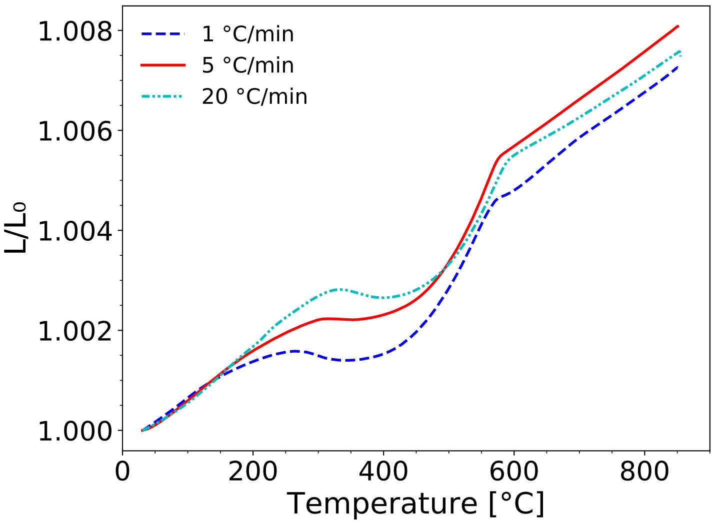

Figure 4.7: Thermal expansion of Ti-15Mo during heating with different heating rates.

Additional information can be obtained from the derivative of thermal expansion, which represents the linear expansion coefficient (α_L) of the material. The definition of the linear expansion coefficient is given by the equation:

$$\alpha_L = \frac{1}{L_0}\frac{dL}{dT}. \tag{4.1}$$

The evolution of α_L for all three heating rates is displayed in Fig. 4.8. Unfortunately, the heating rate of 20 °C/min is already beyond the performence ability of the apparatus, which resulted in influencing the results. The furnace was unable to heat the specimen at low temperatures fast enough. The correct heating rate was reached at about 250 °C, which is manifested by a peak at this temperature, which does not appear in the other curves. Otherwise all curves show similar courses. Interestingly, around 300 °C α_L is negative, which corresponds to the material shrinkage with increasing temperature. This behavior can be attributed to the decrease of lattice parameters of both β and ω phases, which was also observed during isothermal ageing of LCB alloy at 300 °C [14]. At higher temperatures α_L increases and the dissolution of ω particles at 560 °C causes an abrupt decrease of α_L. Between 560 and 750 °C there is an apparent bump at α_L evolution measured with the heating rate 1 °C/min. This bump is probably connected to α phase formation and its subsequent dissolution toward β-transus as the slowest heating rate provides the longest time for α phase to precipitate. The last observable change of α_L, which probably corresponds to complete dissolution of α phase (β-transus), occurs at about 760 °C. At temperatures above 800 °C the values of α_L are nearly equal for all heating rates indicating that no additional transformations occur in the material.

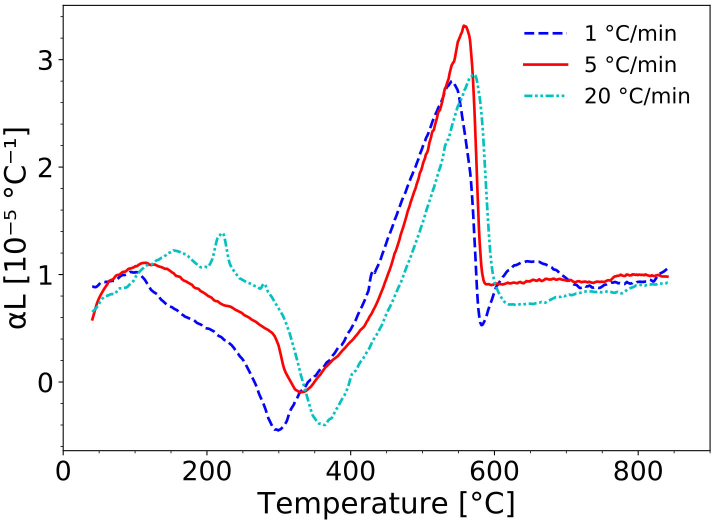

Figure 4.8: Thermal expansion coefficient of Ti-15Mo during heating with different heating rates.

4.2.1 Summary of dilatometry

The thermal expansion of Ti-15Mo during heating with different heating rates was investigated. The results confirmed that dilatometry is an appropriate method for the detection of phase transformations occurring in titanium alloys. However, the dilatometer, which was used, is suitable mainly for slower heating rates. The heating rate of 20 °C/min is already behind the limit of the furnace. The material exhibits an unusual behaviour at about 300 °C, where, for all heating rates, the material shrinks with increasing temperature. The dissolution of ω phase was detected at the same temperature as in electrical resistance measurement (560 °C). The thermal expansion coefficient allows to determine β-transus temperature ($\sim$760 °C).

Additional microstructure observations have to be carried out to relate the underlying microstructural changes with dilatometric measurements.

4.3 Discussion of electrical resistance and dilatometry results

4.3.1 Complementarity of electrical resistance and dilatometry

The comparison of results of dilatometry and electrical resistance is shown in Fig. 4.9. The blue and red lines correspond to thermal expansion and to electrical resistance, respectively. Solid and dashed curves represent heating rate of 1 and 5 °C/min, respectively. The dependence of thermal expansion and electrical resistance on temperature is shown in Fig. 4.9a and their derivatives are presen-

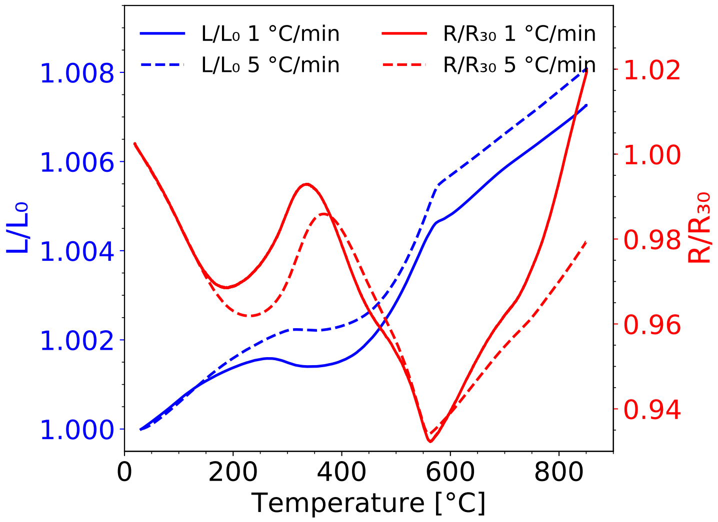

(a) The dependence of thermal expansion and electrical resistance on temperature.

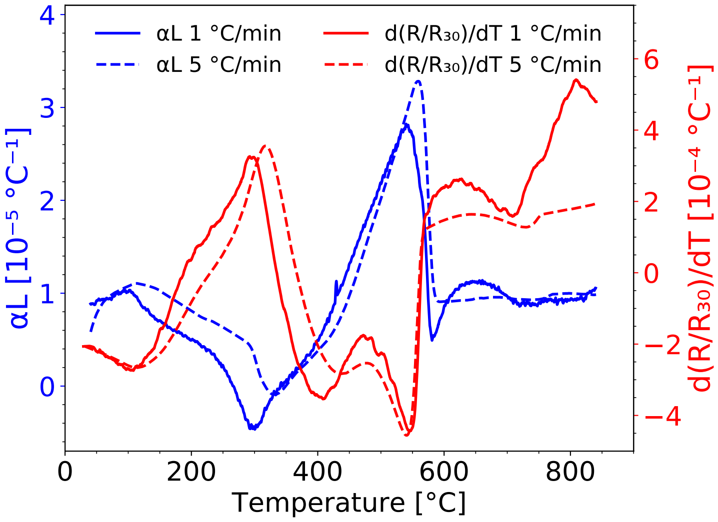

(b) The derivative of electrical resistance and thermal expansion coefficient with respect to temperature.

Figure 4.9: Comparison of dilatometry and electrical resistance resistance.

ted in Fig. 4.9b. The derivatives provide more precise comparison of changes obtained both by dilatometry and electrical resistance. It is obvious that the onsets and ends of respective changes are easier comparable in Fig. 4.9b than in Fig. 4.9a. One can also easily see, that, for the same heating rate, these methods detected the individual processes to occur approximately at the same temperatures. For example the first minimum in derivative of resistance (maximum of α_L) corresponds to an irreversible diffusion assisted growth of the ω_{iso} particles occurs. Another important feature of the derivative curves is a significant drop (increase) of α_L (electrical resistance derivative), which is caused by the complete dissolution of ω particles.

4.3.2 Microstructure observations of ST and pre-annealed material

The most striking feature of the electrical resistance and thermal expansion measurements of Ti-15Mo alloy presented in Fig. 4.9a is that all curves exhibit the same sudden change at 560 °C irrespective of the heating rate. In order to examine this fact in detail, additional two conditions of material were prepared. A bulk specimen was sealed in a quartz tube filled with Ar and heated up to the temperature of 550 °C and 580 °C (i.e. just below and above the temperature of 560 °C) using the heating rate of 5 °C/min followed by immediate water quenching.

TEM observations of ST specimen and samples quenched from 550 and 580 °C were performed to gain more insight into undergoing phase transformation at 560 °C. The microstructures of these specimens are presented in Figs. 4.10, 4.11 and 4.12.

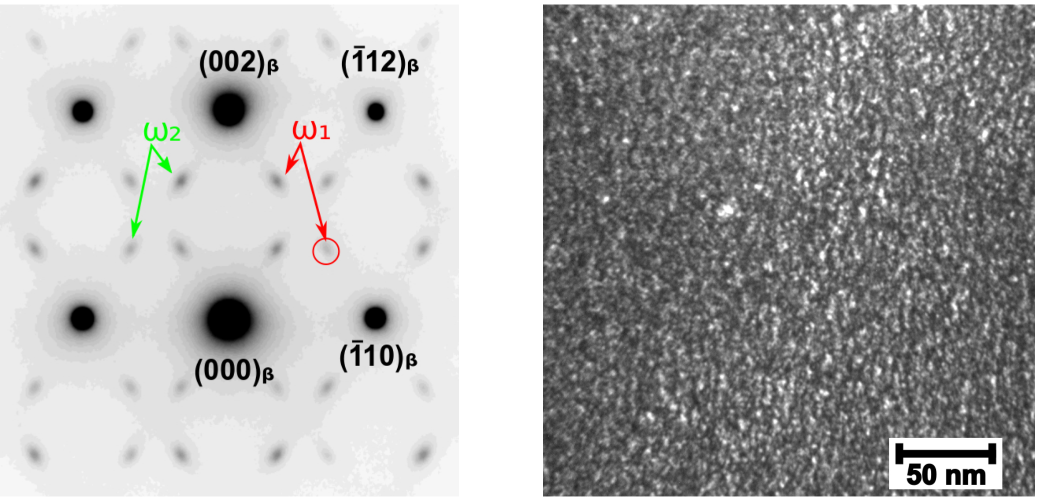

(a) Electron diffraction pattern with a $[110]_\beta$ zone axis, showing the presence of β matrix and ω particles.

(b) DF obtained using the reflection spot marked by red circle in Fig. 4.10a representing one family of ω particles.

Figure 4.10: Microstructure of the ST specimen.

The diffraction pattern of the ST sample is shown in Fig. 4.10a. The strong spots arise from β matrix. The less intense reflections (marked by red and green arrows) correspond to two different crystallographic orientations of ω phase [15].

The dark field (DF) image, Fig. 4.10b, shows one crystallographic family of ω_{ath} particles, which formed during quenching. Their longitudinal dimension is of the order of nanometers, which is consistent with [16] where the authors showed by HRTEM that ST Ti-15Mo consists of β phase and small elipsoidal-shaped ω_{ath} particles (< 1.5 nm in length).

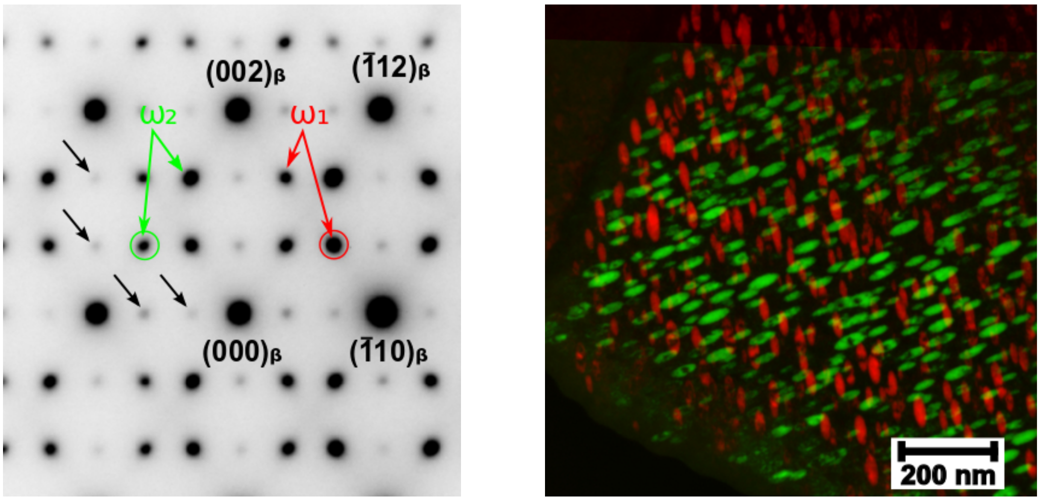

(a) Electron diffraction pattern with a $[110]_\beta$ zone axis, showing the presence of β matrix and ω particles. The extra reflections marked by the black arrows are the result of double diffraction.

(b) Superimposed DF TEM image, obtained using the reflection spots marked by red and green circles in Fig. 4.11a representing two families of ω particles.

Figure 4.11: Microstructure of the specimen quenched from 550 °C.

Figs. 4.11a and 4.11b show selected area diffraction patterns (SAEDs) and a superimposed DF image of two (out of four) crystallographic families of ω_{iso} particles present in the sample quenched from 550 °C, respectively. From Fig. 4.11a it is obvious that the material consists of β matrix and ω phase particles. No α phase was found in grain interior. However, some α precipitates were found at grain boundaries. The ω_{iso} particles shown in Fig. 4.11b (two crystallographic families) are uniformly dispersed in the pre-annealed material, have elipsoidal shape and their longitudinal dimension is about 50 nm. The length of these ω_{iso} particles is aproximately 30 times bigger than of ω_{ath} in the ST sample (cf. Fig. 4.10b or [16]). The ω_{iso} particles observed in Fig. 4.11b are also chemically stabilized, which was proven by our previous SEM observations using chemical contrast of back-scattered electrons [17].

SAED pattern of the sample quenched from 580 °C (Fig. 4.12a) contains besides strong reflections from β phase matrix and reflections from ω phase other weak spots marked with blue circles. Most probably these weak spots originate from small newly developed α precipitates. Additional weak spots in blue circles result from the double diffraction. Simulated diffraction pattern on Fig. 4.12c shows reflections of all three phases with Pitsch-Schrader orientation relationship between α and β phases ($(0001)_\alpha \parallel (110)_\beta$ and $[11\bar{2}0]_\alpha \parallel [100]_\beta$) already observed in Ti-Mo alloys in [18]. The DF image in Fig. 4.12b was obtained using a reflection spot of only one family of ω phase particles. It can be observed that the microstructure of this sample is very similar to the ST material (cf. Figs. 4.10b

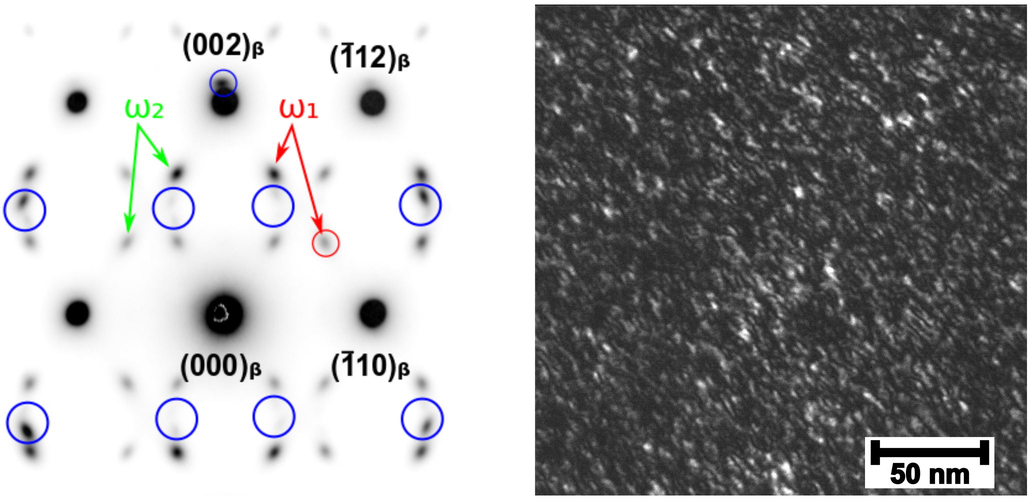

(a) Electron diffraction pattern with a $[110]_\beta$ zone axis, showing the presence of β matrix, ω particles and probably α precipitates with weak point of double diffraction (in blue circles).

(b) DF obtained using the reflection spot marked red circle in Fig. 4.12a representing one family of ω particles.

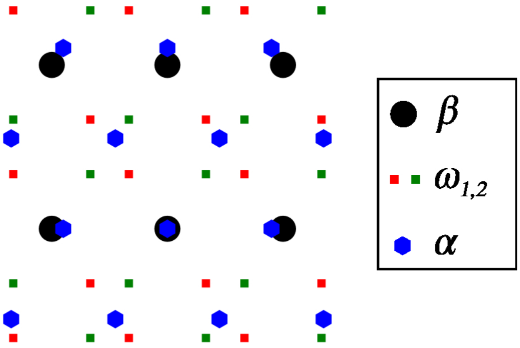

(c) Computed diffraction pattern showing Pitsch-Schrader orientation relationship between α and β phases.

Figure 4.12: Microstructure of the specimen quenched from 580 °C.

and 4.12b). Therefore it is assumed that the observed ω particles are ω_{ath} particles formed after quenching. Apparently lower number of ω_{ath} particles at Fig. 4.12b compared to Fig. 4.10b is caused only by different thickness of both specimens.

The comparison of the microstructures of the material in all three conditions suggests that coarse ω_{iso} particles, which are present in the sample quenched from 550 °C, completely dissolve during heating between 550 and 580 °C. This dissolution manifests itself most likely as the steep change in the resistance curve at 560 °C with no (or very small) dependence on the heating rate (see Fig. 4.3). Small ω particles found in the sample quenched from 580 °C probably form during quenching. The results indicate, that the vast majority of ω_{iso} particles revert back to β phase at 560 °C and consequently they cannot be direct precursors of α precipitation. However, possible compositional pockets with low Mo content left in β matrix in places of former presence of ω_{iso} particles could affect α phase precipitation. Consequently, there could be an indirect influence of ω particles in

α phase precipitation, which is consistent with previous reports [19, 20].

The absence of α phase in the sample quenched from 550 °C proves that α phase does not precipitate during heating between 365 an 560 °C with the heating rate of 5 °C/min.This fact does not rule out the possibility that α phase precipitates in this temperature range during isothermal annealing. However, the decrease of electrical resistance in this temperature range cannot be attributed to precipitation of α particles.

4.3.3 Resistance evolution of ST and pre-annealed material

In order to investigate the behaviour of the material quenched from 550 and 580 °C in more detail, the electrical resistance evolution during heating of both preannealed specimens employing the heating rate of 5 °C/min was compared with the resistance evolution of the material at the initial (ST) condition in Fig. 4.13. Note that the normalization R/R_{560} was necessary in this case to allow direct comparison of results of three measurements of samples with different initial conditions. Obviously, at room temperature, the phase composition of each of the pre-annealed samples is different from that in the ST condition. Therefore, another selection of reference value must be considered. A natural choice of such reference value would be resistance of each sample at any temperature above β-transus ($T > 730$ °C) as the material consists of pure β phase only. However, this choice would be misleading due to enhanced oxidation of specimens and contacts in the furnace at elevated temperatures [21, 22], which is expexted to influence the measured resistance. The best compromise is therefore to use the resistance measured at 560 °C (R_{560}) as the reference value for each sample. ω phase dissolves at 560 °C and the volume fraction of precipitated α is very low in all studied samples [12]. The phase composition at 560 °C is the most comparable in all three

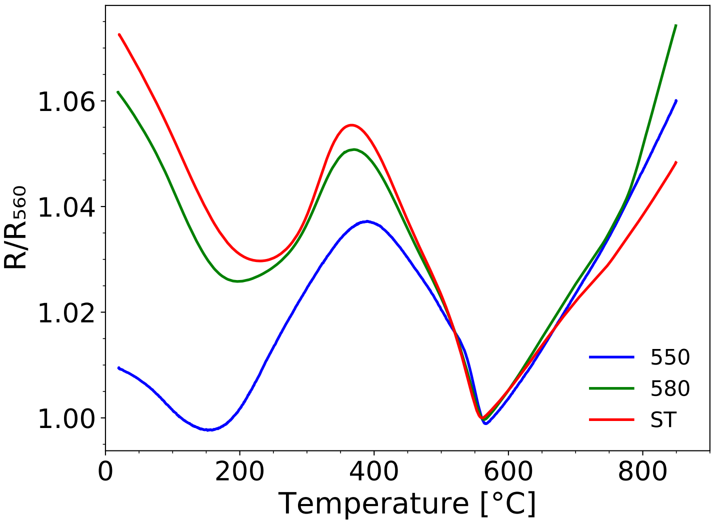

Figure 4.13: The dependence of electrical resistance on temperature for Ti-15Mo samples heated up to 550 and 580 °C and quenched in water compared to ST material.

studied samples and R_{560} is therefore used as the reference value in Fig. 4.13. One can easily confirm in Fig. 4.3 that normalization of the ST samples heated with different heating rates by R_{560} would have the similar effect as the used value of R_{30} even if the different heating rates result in different microstructure evolution during heating before reaching the temperature of 560 °C.

The resistance curves of individual pre-annealed conditions in Fig. 4.13 differ. At low temperatures, the resistance evolution of the sample quenched from 550 °C (blue curve) considerably differs from both other curves (the ST specimen (red curve) and the sample quenched from 580 °C (green curve)). A much smaller initial decrease attributed to ω_{ath} dissolution can be observed. It may be explained by much lower volume fraction of ω_{ath} in the sample quenched from 550 °C than in the other two. In this specimen, large ω_{iso} particles remain; therefore, the formation of ω_{ath} during quenching is suppressed. On the other hand, the resistance of the sample quenched from 580 °C (green curve) is very similar to the ST specimen (red curve). It indicates the similar microstructure consisting of β and ω_{ath} phases in both samples. Slight difference of resistance between the ST material and the sample quenched from 580 °C at room temperature might be caused by a small volume fraction of α phase in the quenched sample.

Note, that the minimum at 560 °C was not affected by the previous heating run for any sample.

The results from electrical resistance measurements combined with microstructure observations (of all three conditions) indicate that grown ω particles in the sample quenched from 550 °C hinder the formation of ω_{ath} during quenching. After heating up to 580 °C, ω_{iso} particles are dissolved and consequently ω_{ath} can form during quenching. The presence of ω_{ath} particles and their subsequent dissolution during heating results in the initial decrease of the resistance in a similar way as observed in the ST material (cf. Fig. 4.13).

4.4 In-situ TEM

Electrical resistance measurement, dilatometry and ex-situ TEM are all indirect methods, whose results always create a certain degree of uncertainty. Therefore, in-situ experiments are necessary to unambiguously prove statements derived from methods, which were presented earlier. For this purpose, in-situ TEM observations of ST Ti-15Mo sample during heating were carried out. The sample was placed in a special holder, which allows controlled heating in TEM. For the sake of comparison with previous measurement, the sample was heated with the heating rate of 5 °C/min.

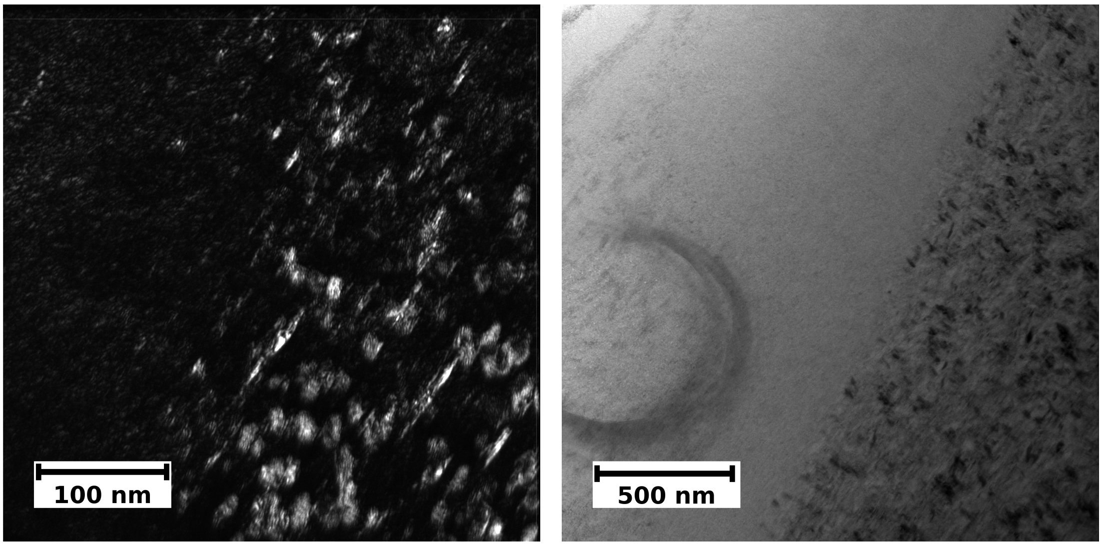

(a) DF image of ω particles.

(b) Inhomogeneous microstructure at 758 °C with dark α precipitates on the right side.

Figure 4.14: An example of inhomogeneous microstructure due to thin foil effect.

During the experiment, coarsening followed by dissolution of ω particles was observed. However, the processes occurred at substantially different temperatures than expected from previous measurements. Detailed investigation of the sample at elevated temperatures revealed different microstructures in thicker regions compared to thin areas. It is well-known that different phases are observed in thin foils than in bulk material (so called thin-foil effect) [23–26]. Ageing of bulk specimen and thin foil of Ti-15Mo alloy at 300 °C resulted in completely distinct microstructures as reported in [25]. This behaviour is caused by either decreased diffusion in thin part of the specimen, different arrangement of strains around ω particles or combination of both. Effect of different thickness on microstructure of studied material is shown in Fig. 4.14. DF image obtained from ω phase diffraction spot at 572 °C is shown in Fig. 4.14a. The material consists of (bright) coarse ω particles (~30 nm) and β matrix. ω particles are located at the right part of the micrograph. At the left side, ω particles are not present at all. It is necessary to note, that in Fig. 4.14a only one grain is shown, thus the absence on ω particles in left part is not caused by different orientation of this area. Another example of inhomogeneous microstructure is presented on

BF TEM micrograph taken at the lower magnification in Fig. 4.14b. This image was taken at the temperature of 758 °C. The different microstructure at each side of the figure can be observed again. The material on the left side of the Fig. 4.14b consists solely of β phase. On the other hand, α precipitates formed on the right side.

The observed thin foil effect excluded any further in-situ TEM experiments due to considerable difference of microstructure evolution compared to bulk material and other methods, which allow investigation of bulk material had to be utilized.

4.5 Synchrotron X-ray diffraction

The X-ray diffraction experiments were performed on single-crystal of Ti-15Mo utilizing high energetic (60 keV) monochromatic beam. The two-dimensional detector allowed fast acquisition of diffraction patterns (10 s per diffraction pattern). The typical Bragg-Bretano powder diffraction geometry, where either the detector or the sample (or both) rotates, could not be utilized due to acquisition time being in order of minutes, which disallows to perform in-situ experiments. The polycrystalline material was not used because of its coarse grained and heavily textured microstructure. The coarse grains would not provide sufficient statistics, which is necessary for powder diffraction pattern.

4.5.1 Analysis of X-ray diffraction data

High energy of the primary beam allowed us to use relatively thick disc-shaped samples cut from the single-crystalline ingot (the thickness of 2 mm, the diameter of 8 mm) and, therefore, to obtain better statistics from the bulk and to suppress potential surface effects. The sample was placed in a furnace equipped with a quartz chamber which allowed the measurement in vacuum of the order of 10^{-6} mbar. For the measurement, the single-crystal was oriented with its $[100]_\beta$ crystallographic axis parallel to the incoming beam. In order to ensure a precise orientation even during heating, an automatic software was used. Intensities of $\{011\}_\beta$ reflections (see Fig. 4.15) were compared and the tilt of the sample was adjusted to minimize the difference between intensities of these reflections. This

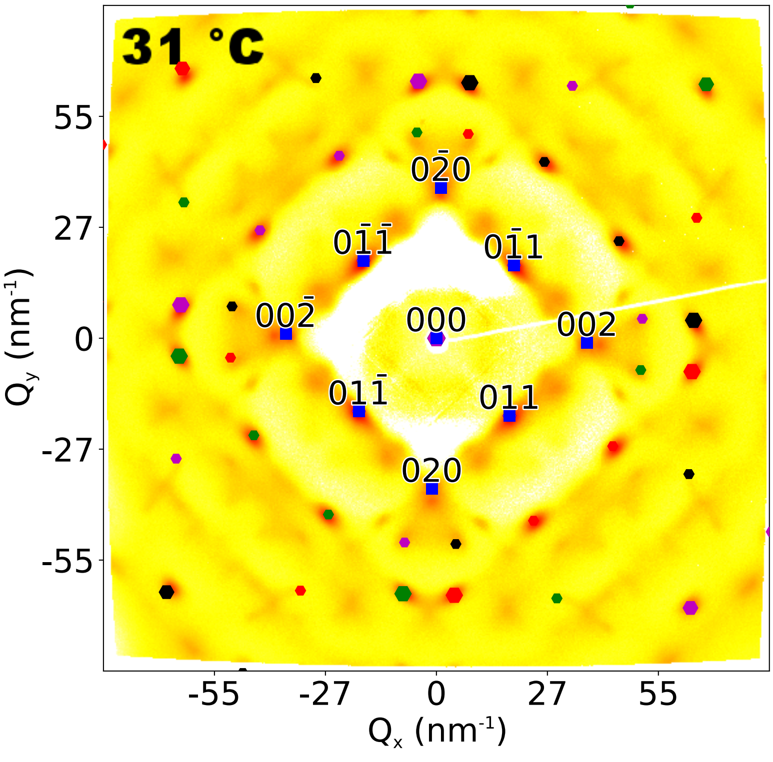

Figure 4.15: Diffraction pattern obtained at room temperature with indexed β reflections.

procedure preceded the acquisition of each diffraction pattern.

In this posistion none of β or ω reflections exactly satisfy the Bragg condition [27]. Due to broadening of the reflections, their detection is possible, even if the center of the peak is not exactly at the Ewald sphere [28]. β phase reflections are broadened due to several effects including e.g. instrumental contributions and crystal imperfections. On the other hand, the main contribution to broadening of ω peaks is the extremely small size of ω particles. This is schematically shown in Fig. 4.16, where cyan curve represents the Ewald sphere, black dots exact positions of diffraction spots and pink ellipses the broadening due to particle size and shape. It is necessary to note, that if a peak sharpens (for instance due to growth of particles), the observed intensity can either increase (if the actual reflection is very close to the Ewald sphere) or decrease (if the actual reflection is farther from the Ewald sphere).

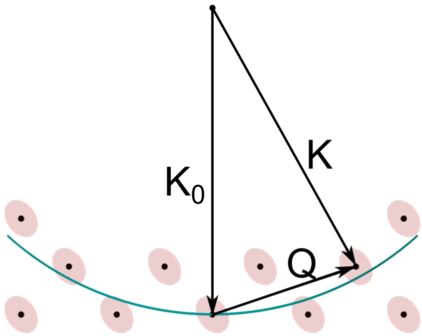

Figure 4.16: Schematic illustration of the broadening effect of particle size on shape of diffraction maxima.

TEM observations presented in previous section showed that ω particles in Ti-15Mo are prolate spheroids. It was also found that their longest axis is of the order of nanometers in the solution treated condition, while it can reach about 50 nm in the specimen heated to 550 °C. The coarsening of ω particles with increasing temperature will therefore result in sharpening of reflection maxima, with the above mentioned consequences. However, it should be noted that the diffraction pattern contains a large number of different omega reflections (see Fig. 4.15) which are at different distances from the Ewald sphere. Therefore, even if the peaks sharpen due to ω particle coarsening, it is extremely unlikely that all ω reflections disappear. On the other hand, if no ω reflections are observed, it can be concluded that no ω phase is present in the material.

The reciprocal space of the β phase matrix with ω particles satisfying the orientation relationship $(0001)_\omega \parallel (111)_\beta$, $[11\bar{2}0]\omega \parallel [011]_\beta$ [29] is shown in Fig. 4.17. Interactive 3D model can be found in the attached CD. There are 4 possible orientations (crystallographic families) of ω phase in β matrix. Note that all ω reflections are represented by colored dots, while blue squares represent reflections of the β phase. Cyan-colored square defines the region investigated in this study, which is given by the dimensions and the distance of the detector from the sample. Blue cubes represent reflections of the β phase. The color of the dots (not of the circles) corresponding to ω reflections represents one of the four different crystallographic families of ω phase. Note also that the size of the dots corresponds to the proximity to the Ewald sphere - the larger the size of the

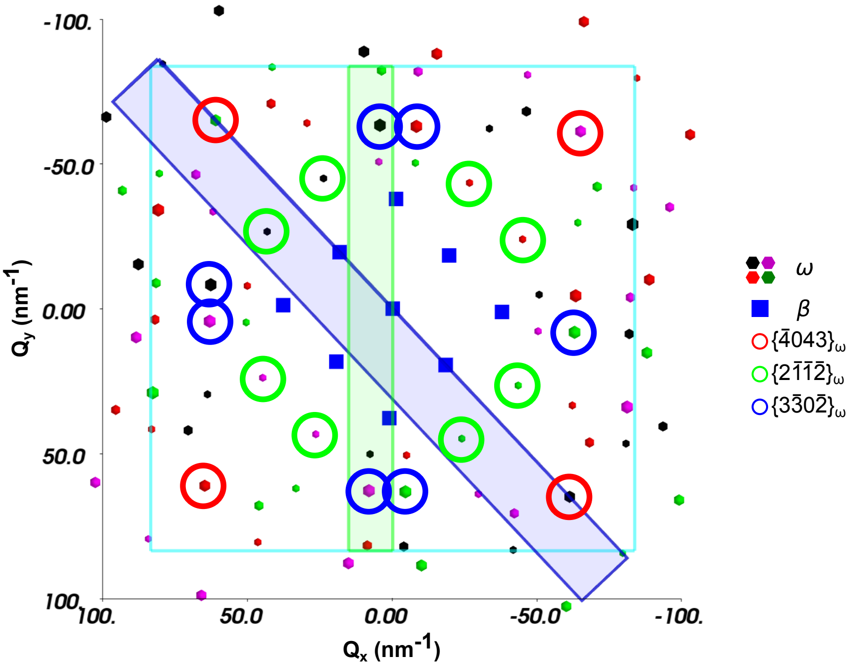

(a) Calculated diffraction pattern with zone axis $[100]_\beta$. Cyan-colored square defines the region of the Ewald sphere investigated in this study.

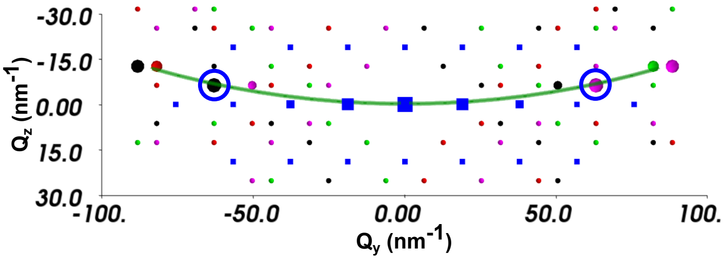

(b) View perpendicular to green part of Ewald sphere from Fig. 4.17a (zone axis $[010]_\beta$).

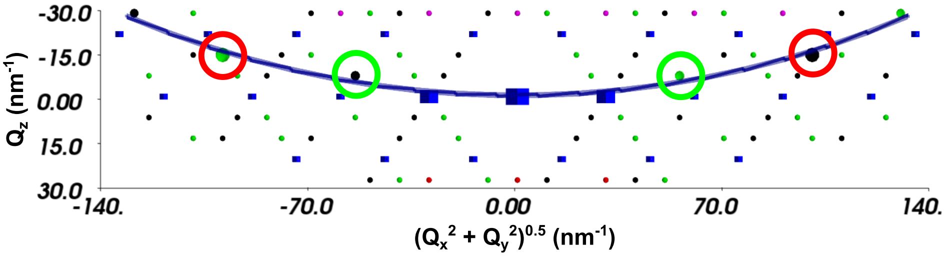

(c) View perpendicular to blue part of Ewald sphere from Fig. 4.17a (zone axis $[011]_\beta$).

Figure 4.17: The scheme of the reciprocal space of beta matrix with omega particles satisfying the orientation relationship $(0001)_\omega \parallel (111)_\beta$, $[11\bar{2}0]\omega \parallel [011]_\beta$. Blue cubes represent reflections of β phase. Positions of ω phase diffraction spots are denoted by colored dots (not of the circles), each color represents different crystallographic family of ω phase. Three closest ω reflections to the Ewald sphere are highlighted by circles, which correspond to red: $\{\bar{4}043\}_\omega$, green: $\{2\bar{1}\bar{1}\bar{2}\}_\omega$ and blue: $\{3\bar{3}0\bar{2}\}_\omega$.

dots is, the closer are the reflections to the Ewald sphere. Three closest types of ω reflections in Fig. 4.17a are highlighted by red, green and blue circles and correspond to $\{\bar{4}043\}_\omega$, $\{2\bar{1}\bar{1}2\}_\omega$ and $\{3\bar{3}0\bar{2}\}_\omega$ diffraction maxima, respectively. The evolution of the intensity of these reflections will be thoroughly discussed in the following section.

Recall that Fig. 4.17a is a 2D projection of positions of diffraction maxima in a 3D reciprocal space. The green and blue shaded rectangles in Fig. 4.17a are in fact rectangular cuboids representing two parts of the reciprocal space, which were selected for the demonstration of distances of the three closest ω reflections from the Ewald sphere. Figs. 4.17b and 4.17c show perpendicular views to green and blue rectangles (cuboids), respectively. This clarifies that the reflections $\{3\bar{3}0\bar{2}\}_\omega$ (highlighted by blue circles) are the closest ones to the Ewald sphere (Fig. 4.17b), while $\{\bar{4}043\}_\omega$ and $\{2\bar{1}\bar{1}2\}_\omega$ reflections highlighted by red and green circles are farther from the Ewald sphere (Fig. 4.17c). The closest $\{3\bar{3}0\bar{2}\}_\omega$ reflections represent the evolution of ω phase particles during heating most accurately. Note that reflections farther from the Ewald sphere shown in Figs. 4.17b and 4.17c were omitted in Fig. 4.17a to ensure its clarity.

4.5.2 Results of X-ray diffraction

Five selected diffraction patterns taken at significant temperatures during linear heating of the Ti-15Mo single-crystal with the heating rate of 5 °C/min are presented in Fig. 4.18 and discussed bellow. Complete record of the measurement is presented in a video, which can be found in the attached CD.

The diffraction pattern of the ST material (Fig. 4.18a) shows reflections of β and ω phases. TEM observations presented in previous section showed that ST Ti-15Mo consists of β phase matrix and small ω particles.

The diffraction pattern of the material heated up to 426 °C, where the maximal intensity of ω diffraction spots was observed, is shown in Fig. 4.18b.

Reflections solely from the β phase can be found in the diffraction pattern of the material heated up to 560 °C (see Fig. 4.18c). It proves unambiguously that ω particles dissolved before α precipitates formed. Therefore, in Ti-15Mo, ω particles are not direct precursors of α precipitation during continuous heating with the rate of 5 °C/min. On the other hand, β, ω and α phases may coexist and ω particles can act as preferential nucleation sites for α phase formation during isothermal ageing at suitable temperature [30–32].

The fourth diffraction pattern (see Fig. 4.18d) was acquired at 662 °C (the highest achieved temperature) shows diffraction spots of β and α phases. The material after (uncontrolled) cooling from 662 °C consists of a mixture of α and β phases formed at high temperatures and ω phase, which occurred during cooling. The corresponding diffraction pattern is presented in Fig. 4.18e, where the reflections of all three phases can be observed.

The detail of the right bottom corner of all five diffraction patterns from Fig. 4.18 is shown in Fig. 4.19. This area of diffraction was chosen due to easily distinguishable $(\bar{1}410)_\alpha$ and $(\bar{4}043)_\omega$ diffraction spots (see Fig. 4.19e). For most of other the diffraction maxima from α and ω phases overlap over each other, which prevents us from distinguishing them from each other. In Figs. 4.19a, b there is pointed out ω diffraction spot. In Fig. 4.19c, which is detail of Fig. 4.18c

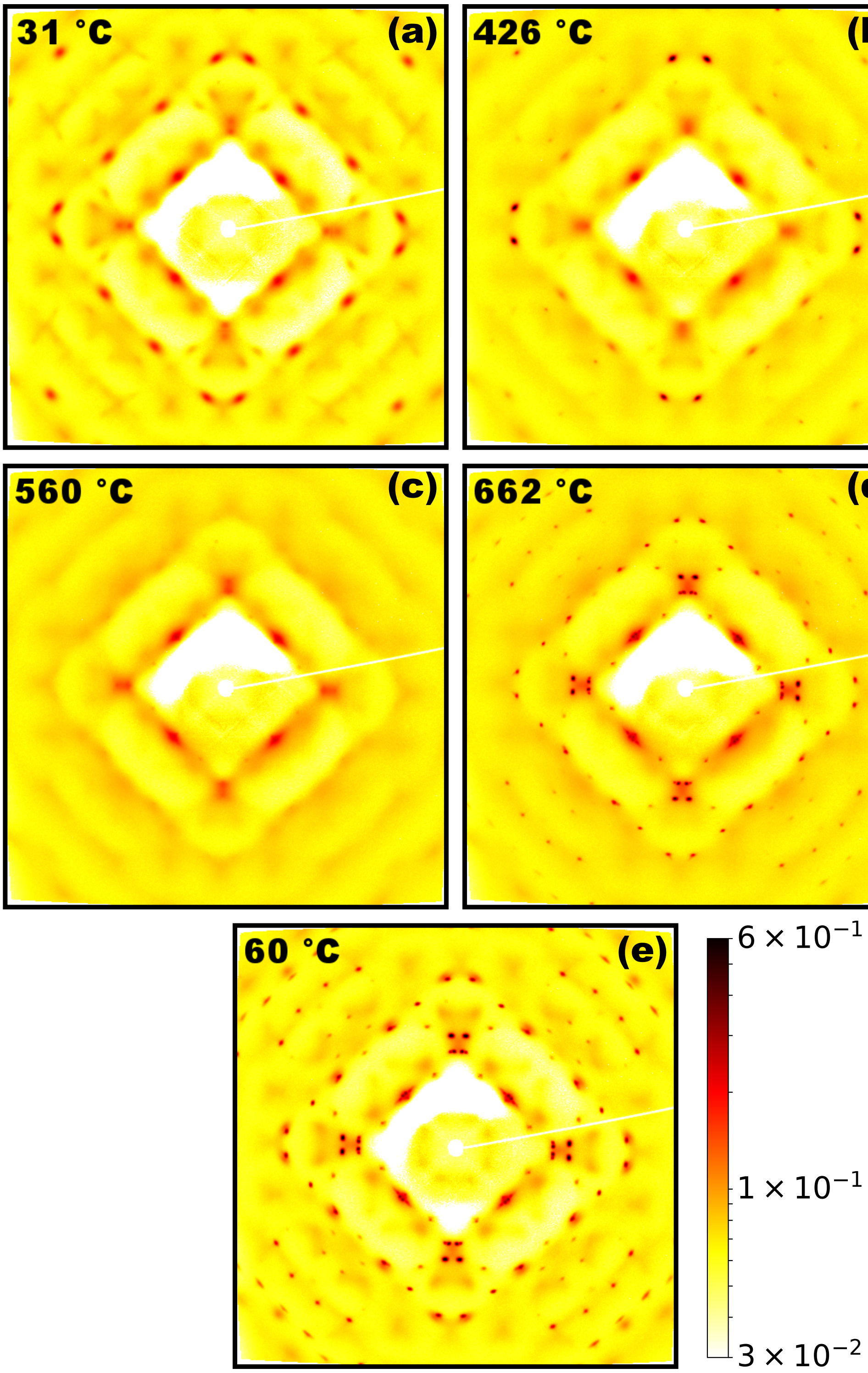

Figure 4.18: Measured diffraction patterns of material: (a) in initial condition at room temperature, (b) at 426 °C, (c) at 560 °C (no ω nor α reflections), (d) at 662 °C (maximal reached temperature), (e) after cooling down to 60 °C.

there are no reflections present. On the other hand, many diffraction spots occur in Fig. 4.19d. All of these diffraction spots are from α phase. After cooling to 60 °C, $(\bar{4}043)_\omega$ diffraction spot is observable (see Fig. 4.19e), which means that ω phase formed during cooling even though α phase was present in the material.

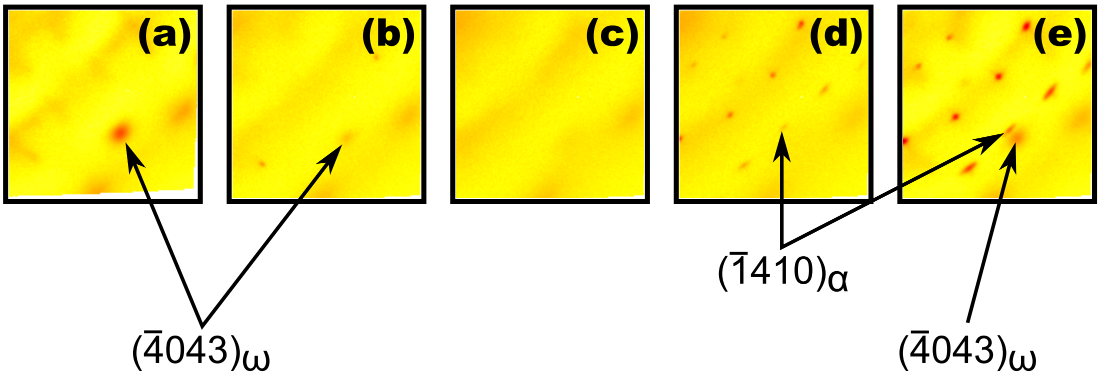

Figure 4.19: Details of measured diffraction patterns in Fig. 4.18: (a) in initial condition at room temperature, (b) at 426 °C, (c) at 560 °C (no ω nor α reflections), (d) at 662 °C (maximal reached temperature), (e) after cooling down to 60 °C.

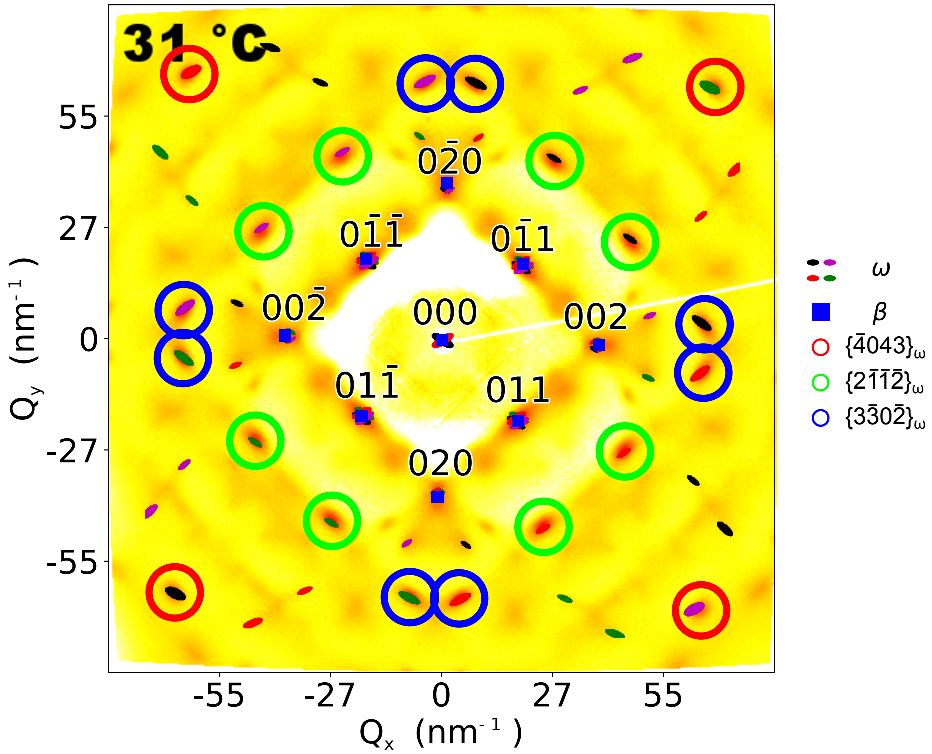

Figure 4.20: Diffraction pattern of the specimen at room temperature overlapped with the computed pattern. The material consists of β phase matrix and ω particles. Blue squares represent β and ellipses ω. Size of spots corresponds to the distance of the reflections from the Ewald sphere and colours of ω reflections represent different crystallographic families. The circles highlight the same ω reflections as in Fig. 4.17a.

Assignments of diffraction spots to respective phases for the material at room temperature is shown in Fig. 4.20. Measured reflections are overlaid with a calculated diffraction pattern. Computed ω reflections have elliptical shape. The position of calculated ω reflections is based on known orientation relationship between β phase and ω particles: $(0001)_\omega \parallel (111)_\beta$, $[11\bar{2}0]\omega \parallel [011]_\beta$ [29]. The ellipses represent an actual shape of ω reflections, which is determined by the true shape of ω particles. ω particles are prolate spheroids elongated in the $[111]_\beta$ direction. Its reflections are oblate spheroids with the shortest axis in the $[111]_\beta$ direction in reciprocal space centred at the positions of ω reflections. The ellipses shown in Figure 4.20 represent cuts of the Ewald sphere through these oblate spheroids. Each color of the ellipses corresponds again to each of the four different crystallographic families of the ω phase.

Fig. 4.21 shows the diffraction pattern of $\beta+\alpha$ material at 662 °C. Calculated β and α reflections are represented by square and triangle markers, respectively. It follows from Burgers relationship ($\{0001\}_\alpha \parallel \{110\}_\beta$, $\langle 11\bar{2}0\rangle \parallel \langle 111\rangle_\beta$ [33]) between β and α phases, that there are twelve different families of α in β. The size of calculated triangle symbols corresponds to the distance of the individual reflections from the Ewald sphere. Larger symbols are closer to the Ewald sphere. The color of individual calculated reflections is associated with the particular crystallographic family of the α phase.

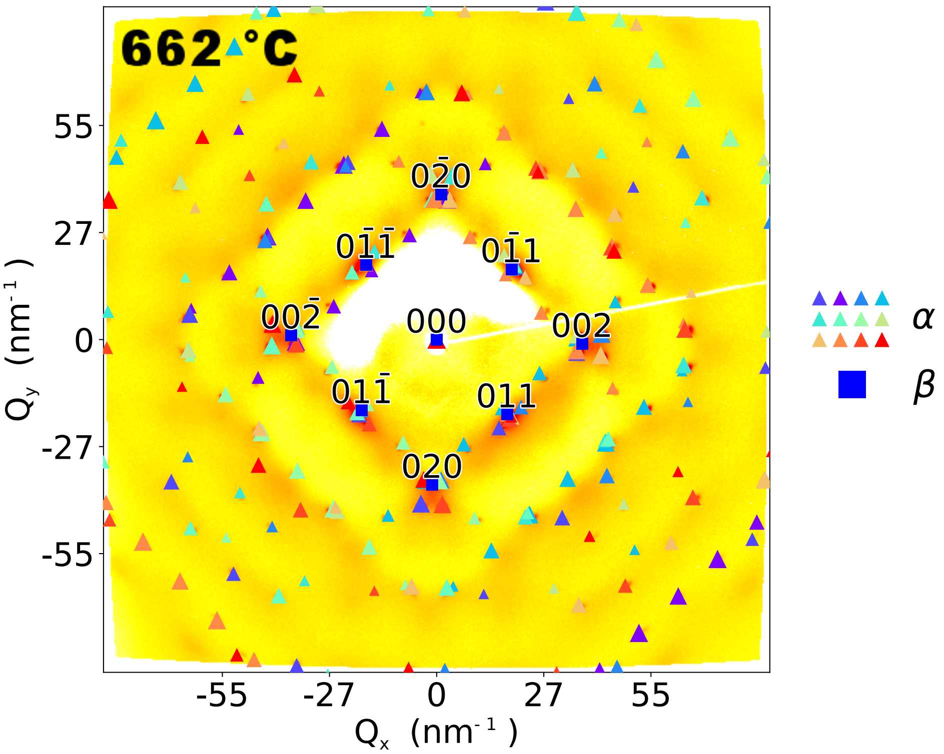

Figure 4.21: Diffraction patter of the material heated up to 662 °C. The material consists of β phase matrix and α precipitates. Blue squares represent β and triangles α phase. The size of spots corresponds to the distance of the reflections from the Ewald sphere and colours of α reflections represent different crystallographic families.

The calculated diffraction pattern overlapped with the diffraction pattern measured after cooling down to 60 °C is shown in Fig. 4.22. The material consists of of β phase matrix, α and ω precipitates. Blue squares, triangles and dots represent β, α and ω phase, respectively. Size of spots corresponds to the distance of the reflections from the Ewald sphere and colors of α and ω reflections represent different crystallographic families. Positions of the reflections were calculated utilizing the above mentioned orientation relationships for both α and ω phases.

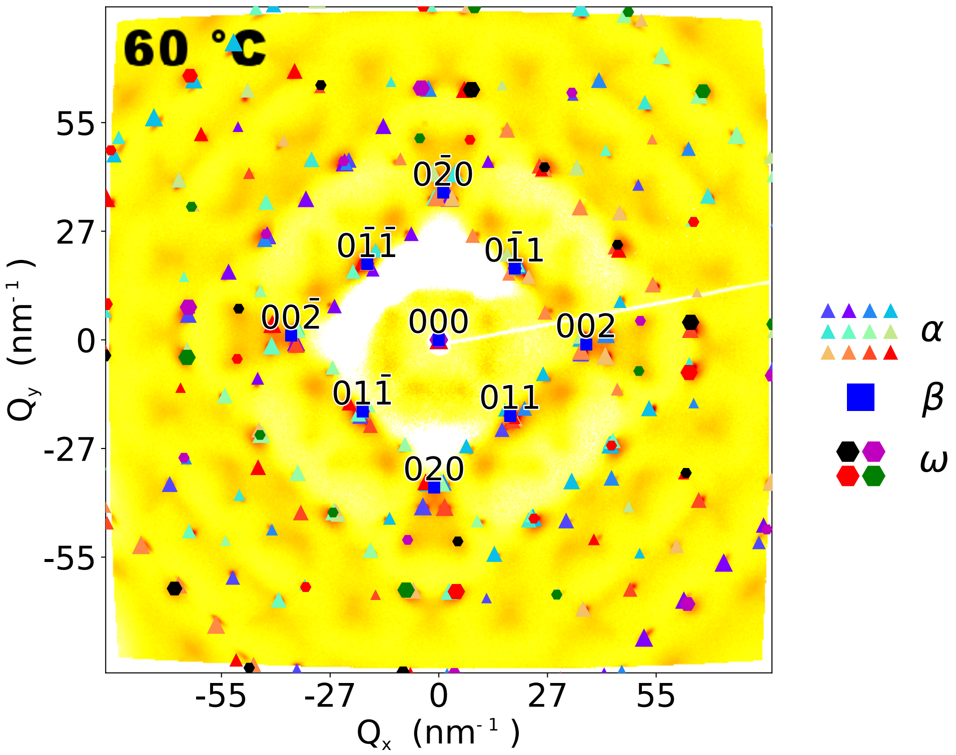

Figure 4.22: Diffraction patter of the material after cooling down to 60 °C. The material consists of β phase matrix, α and ω precipitates. Blue squares, triangles and dots represent β, α and ω phase, respectively. The size of spots corresponds to the distance of the reflections from the Ewald sphere and colors of α and ω reflections represent different crystallographic families.

It is obvious that calculated patterns fit quite well with the measured ones. This confirms that at room temperature, the material consists of β and ω phases, while at 662 °C, it is composed of a mixture of α and β phases.

The intensity of ω reflections (highlighted in Figs. 4.17 and 4.20) varies during linear heating, as can be qualitatively observed in diffraction patterns in Fig. 4.18 and in the attached video. The evolution of one of the $\{\bar{4}043\}_\omega$, one of the $\{2\bar{1}\bar{1}2\}_\omega$ and one of the $\{3\bar{3}0\bar{2}\}_\omega$ reflections with respect to temperature is displayed in Fig. 4.23. Fig. 4.23 was created by taking a square region around a selected ω reflection and plotting a bunch of intensities measured in this region for different temperatures. A projection of this 3D bunch is shown in Fig. 4.23. Red, green and blue frames around the individual images correspond to the colors of circles used in Figs. 4.17 and 4.20.

All three reflections in Figure 4.23 exhibit qualitatively similar behavior. The initial intensity decreases during heating up to 300 °C, but the reflections do not disappear completely. Another increase of the intensity is observed at around 400 °C. As the $(3\bar{3}0\bar{2})_\omega$ reflection (blue frame) is the closest to the Ewald sphere, its intensity exhibits the most pronounced maximum at about 430 °C. On the other hand, the $(\bar{4}043)_\omega$ and $(2\bar{1}\bar{1}2)_\omega$ peaks (red and green frames, respectively) have a lower intensity at 430 °C as compared to room temperature. It is consistent with coarsening of ω particles and bigger distance from Ewald sphere (see

Fig. 4.16). All ω reflections disappear at 560 °C. The intensity which appears at higher temperatures (above 580 °C, green and blue frame) is associated with the formation of α phase. The vertical black line marks the temperature of the complete dissolution of ω phase (560 °C). α reflections almost coincide with the positions of reflections of ω. Note that the reflections associated with the alpha phase (above 580 °C) are slightly shifted with respect to the omega peaks, which indicates that they arise from a different phase with different lattice parameters.

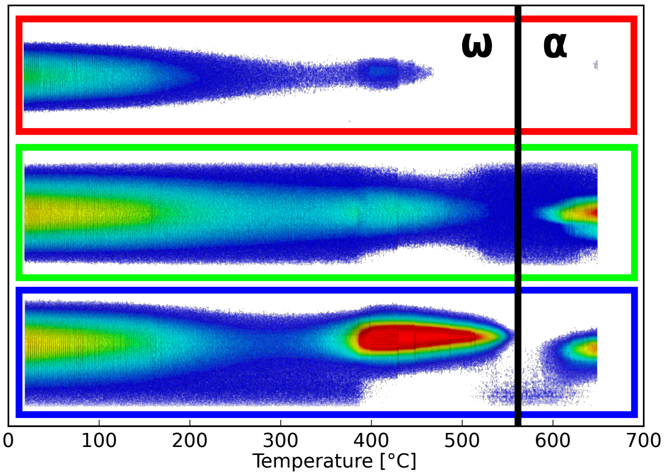

Figure 4.23: Temperature evolution of one of three closest equivalent ω reflections. The frame color around each peak corresponds to respective colors of circles in Fig. 4.20 (red: $(\bar{4}043)_\omega$, green: $(2\bar{1}\bar{1}2)_\omega$ and blue: $(3\bar{3}0\bar{2})_\omega$).

In order to determine the evolution of volume fraction of ω phase, the intensity of ω peak have to be estimated. The intensity of a diffraction peak from particles is given by equation [34]:

$$I(\mathbf{Q}) = A\langle\sum_n\sum_m \Omega_n(\mathbf{Q})\Omega_m^*(\mathbf{Q})e^{-i\mathbf{Q}(\mathbf{R}_n-\mathbf{R}_m)}\rangle, \tag{4.2}$$

where A is a constant given by the intensity of the primary beam, the volume fraction of ω phase, instrumental contribution etc., $\mathbf{R}$ represents the position of atoms in unit cell and Ω is a geometrical factor of particles (the shape of ω particles in our case). Considering a random-phase approximation, where the waves from various particles do not interfere:

$$I(\mathbf{Q}) = AN\langle|\Omega(\mathbf{Q})|^2\rangle, \tag{4.3}$$

where N is the number of irradiated particles. In the following we assume that the particles are prolate spheroids with random radii, the radii are distributed according to the Gamma distribution with the order m and the mean values R_L and R_V. The averaging can be performed directly and we obtain:

$$\begin{aligned} I(\mathbf{Q}) &= AN\frac{16\pi^2R_L^4R_V^2}{\kappa^6}\mathrm{Re}\{\frac{1}{2}+\frac{\kappa^2}{2}\frac{m+1}{m}\left(1+\frac{1}{p^{m+2}}-\frac{1}{2p^m}\right)+\frac{i\kappa}{p^{m+1}}\} \\ p &= 1-\frac{2i\kappa}{m} \\ \kappa &= \sqrt{(Q_1R_L)^2+(Q_2R_L)^2+(Q_3R_V)^2} \end{aligned} \tag{4.4}$$

Orientation relations between R_L, R_V and $\mathbf{Q}$ are indicated in Fig. 4.24. ω particles are prolate spheroids, with its longest axis (R_V) parallel to $\langle 111\rangle\beta$ (four possible orientations). The detector is perpendicular to $[001]_\beta$. The known relation between the coordination system of the detector ($\mathbf{Q}_m = (Q_x, Q_y, Q_z)$) and the coordination system of ω particles ($\mathbf{Q}_n = (Q_1, Q_2, Q_3)$) allowed to calculate the rotation matrix $\mathbf{R}$ for each of four crystallographic ω families, which was already utilized in Fig. 4.20. The spheroid is centred at the origin of $\mathbf{Q}_n$ (green axes) coordinate system. Its semi-axes R_L and R_V are aligned along the coordinate axes. The origin of the $\mathbf{Q}_n$ (green axes) coordinate system is shifted along the Q_z axis in order to emphasize the real situation, where ω diffraction spots do not lay exactly at the Ewald sphere.

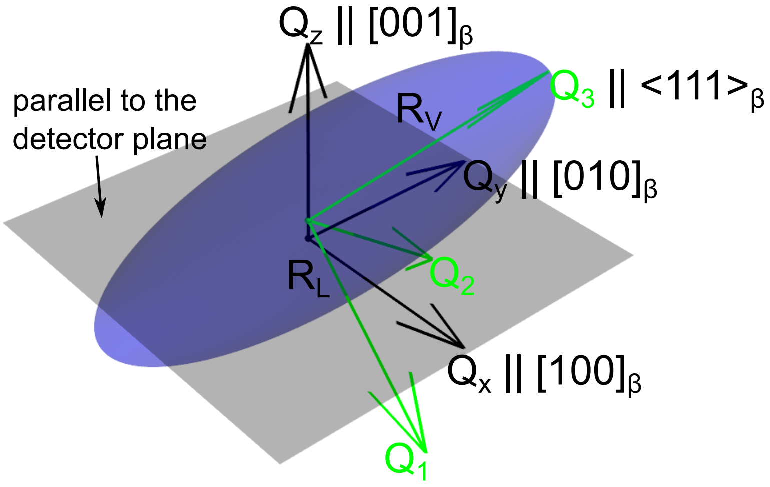

Figure 4.24: Orientation relations between elliptical ω particle and the detector.

Q_x and Q_y were captured on the detector and Q_z was set as the distance of the position of the reflection from the Ewald sphere at room temperature. The thermal expansion of the lattice parameters of ω phase is unknown, therefore the Q_z was fixed at the same value for all diffraction patterns. Q_n were determined from:

$$\mathbf{Q}_n = \mathbf{R}\mathbf{Q}_m. \tag{4.5}$$

The relative volume P of ω phase can be calculated from:

$$P = \frac{4}{3}\pi\langle R_L^2 R_V\rangle \frac{N}{V}, \tag{4.6}$$

where V is the irradiated volume of the sample (assumed constant), and

$$\langle R_L^2 R_V\rangle = R_L^2 R_V \frac{(m+1)(m+2)}{m} \tag{4.7}$$

where $m = 10$. The value of m was determined as the most appropriate already in previous calculations concerning ω particles utilized in [35, 36].

In order to determine the relative volume fraction of ω phase, the individual $\{3\bar{3}0\bar{2}\}_\omega$ reflections (highlighted in Figs. 4.17 and 4.20 by blue colored circles) were, for each acquired diffraction pattern, fitted with the equation 4.4 utilizing the least squares method. These reflections were chosen because they are closest to the Ewald sphere and therefore, they represent most accurately the evolution of ω phase particles. The normalized average values of the relative volume of ω phase P/P_0 are presented in 4.25 as cyan dots.

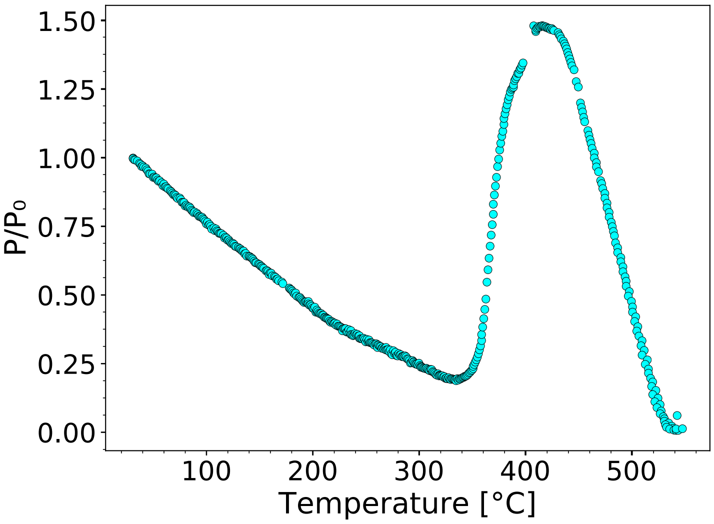

Figure 4.25: Relative volume fraction of ω phase calculated from $\{3\bar{3}0\bar{2}\}_\omega$ reflections.

The analysis of phase transformations is hindered because the measured intensity is simultaneously affected by the volume fraction of ω phase, the size of particles and the actual distance of reflection from the Ewald sphere. This distance, which was considered constant, is affected by changing lattice parameters of both β and ω phases (due to thermal expansion and diffusion of alloying elements [14]) and even by incompleteness of $\beta \rightarrow \omega$ transformation [36]. However, a number of conclusions can be drawn from the obtained results:

- The initial decrease of the volume fraction is consistent with the initial decrease of electrical resistance and a decrease of elastic constants [37].
- Volume fraction of ω phase determined from XRD measurements steeply increases above 350 °C with maximum at 420 °C.
- The calculation of volume fraction is greatly affected by a size of ω particles, therefore the determined values represent rather coarsening of ω particles coupled with increase of volume fraction, than just volume fraction itself.
- Subsequent decrease of volume fraction of ω phase between 420 °C and 560 °C could be caused by further coarsening of ω particles coupled with a decrease of volume fraction of ω phase.
  In order to support or reject the idea of the continuing growth ω particles a TEM observations of the material heated up to 420 °C and subsequently quenched into water were performed. The DF image obtained using a diffraction spot of ω phase of such material is shown in Fig. 4.26. The size of ω_{iso} particles in this sample was about 15 nm. During heating up to 550 °C, the particles have grown to 50 nm 4.11b.

- In the temperature range from 560 to 580 °C, no peaks were detected at the positions of $\{3\bar{3}0\bar{2}\}_\omega$.
- XRD provided the first direct observation of evolution of volume fraction of ω phase and its complete dissolution at 560 °C.

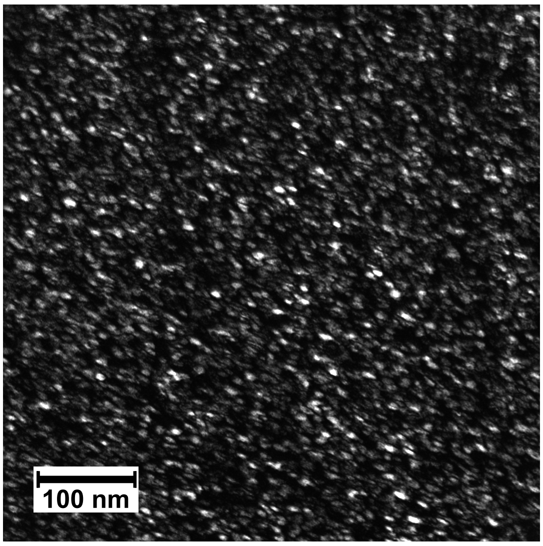

Figure 4.26: Microstructure of the specimen quenched from 420 °C.

The distance of ω reflections from the Ewald sphere probably increases with temperature due to change of lattice parameters of ω phase. The detected intensity is, for coarse particles, extremely affected by this distance. Unfortunately, we were not able to determine the change of lattice parameters. At 580 °C diffraction spots from forming α phase appeared. However, the volume fraction of α phase is not shown as it could not be determined due to unknown orientation relationship between the shape of α precipitates and β matrix.

4.5.3 Summary of XRD

Synchrotron X-ray diffraction proved as an excellent technique to study processes occurring in the material, but challenging in processing of the measured data. Investigation of a single-crystal allows to distinguish all 4 crystallographic families of ω and all 12 variants of α phase. The temperature evolution of reflections of all ω families was the same. Therefore, none of the families is preferred. The same applies for the different α variants. The XRD confirms, that ω phase completely dissolves at 560 °C. Only β phase is present in the temperature range of 560 °C - 580 °C. As a consequence, ω particles do not serve as direct precursors for α phase formation in Ti-15Mo alloy during linear heating.

4.6 Neutron diffraction

Neutron diffraction experiments were performed at the research reactor in ILL Grenoble. Two types of experiments aiming to determine the details of phase transformations occurring in Ti-15Mo alloy were performed:

a) the influence of the heating rate on the kinetics of phase formation,

b) investigation of kinetics of ω dissolution and α formation during ageing.

The measured data obtained during ND experiments are shown in Figs. 4.27, 4.29 and 4.31. All measured results are displayed at the same logarithmic scale to allow their direct comparison. Four selected diffraction patterns from each measurement are presented in Figs. 4.28, 4.30 and 4.32. The diffraction patterns were acquired at four temperatures, namely the RT, the temperatures corresponding to maximal amplitude of ω and α phase peaks and the highest measured temperature. The position of individual phases peaks is shown bellow each diffraction pattern. The most distinct peaks are indexed. In the first measurement (heating with the heating rate of 1.9 °C/min followed by cooling with the rate of 5 °C/min), the sample was placed in niobium container, which resulted in additional Nb peaks in the diffraction patterns. This fact was realized only after the start of the diffraction experiment and due to limited measuring time the experiment had to continue with the Nb container. In subsequent experiments vanadium container, whose nuclei hardly scatter neutrons, was used. Nb has the BCC structure, therefore Nb peaks have the same Miller indexes as neighbouring β peaks and there is no need to index them in Fig. 4.28. The additional Nb peaks overlap with some of β and ω peaks and disallow to exactly determine the respective phase fractions. Therefore, the volume fractions of ω and β corresponding to the first experiment were taken from ageing experiment.

The obtained results from ND are consistent with results previously presented in this chapter. The material at room temperature consists of β phase matrix and ω particles, although ω peaks are small and wide at this temperature (see Fig. 4.28a). The volume fraction of β and ω phase is 60 % and 40 %, respectively. The peaks of ω phase sharpen during heating most obviously around 300 °C, which is caused by coarsening of ω particles. ω peaks reach maximum amplitude at 456 °C. The diffraction pattern with the highest amplitude of ω peaks is shown in Fig. 4.28b. In this condition the volume fraction of ω phase is about 65 %. At higher temperatures, the intensities of the ω peaks decrease. After the complete dissolution of ω phase at about 560 °C, α phase starts to form. α phase peaks reach maximum amplitude at 633 °C and the material at this condition contains 45 % of α. During subsequent heating, α phase diffractions intensities decrease and completely disappear around 730 °C, which is consistent with β-transus temperature determined from the electrical resistance measurements. At the highest temperature (850 °C), the material contains only β phase, as can be seen in Fig. 4.28d. During cooling (see Fig. 4.27b), α and ω phases form at about 500 and 320 °C, respectively. One can see, that the cooling rate of 5 °C/min is insufficient to suppress α phase formation. However, the amount of precipitated α phase not enough to stop ω formation.

The results of the second experiment (heating and cooling with the rate of 5 °C/min) are shown in Fig. 4.29. The initial condition is the same as in the

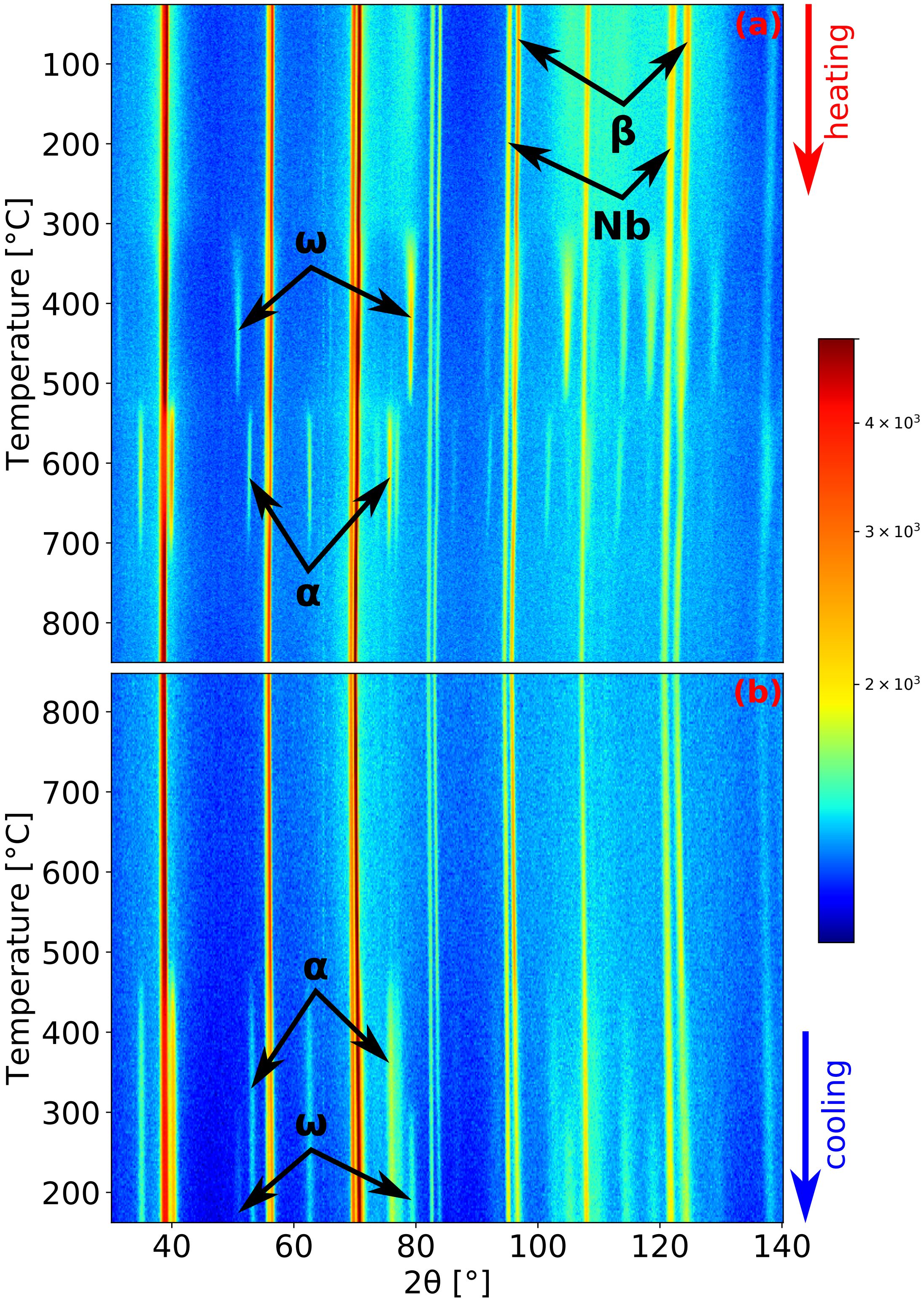

Figure 4.27: Neutron diffraction pattern evolution of Ti-15Mo during: (a) heating with the heating rate of 1.9 °C/min, (b) cooling with the cooling rate of 5 °C/min.

previous experiment (cf. Fig. 4.30a) with 62 % of β and 38 % of ω phase. Due to the faster heating rate compared to previous experiment and the occurring processes being diffusion controlled, the maxima of amplitude of ω and α peaks are shifted to higher temperatures. For ω phase it is 465 °C and the volume

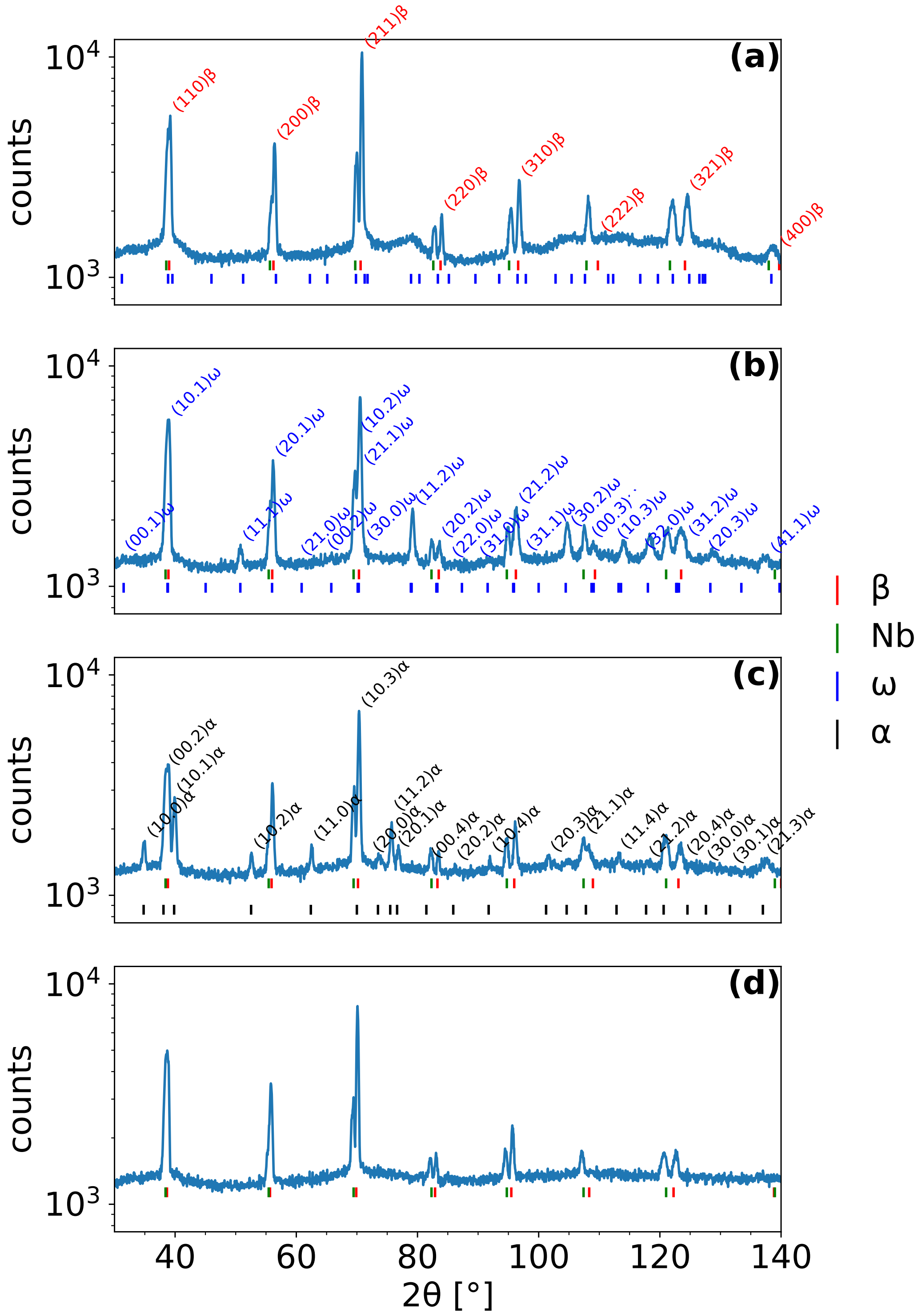

Figure 4.28: Selected diffraction patterns at different temperatures from Fig 4.27a). (a) Room temperature, (b) 456 °C, (c) 633 °C, (d) 850 °C.

fraction of ω phase at this temperature is 37 % (see Fig. 4.28b). The maximum of the amplitude of α peaks is shifted to 663 °C and the volume fraction of α phase at this temperature is 10 % (Fig. 4.28c). Similarly as in the previous experiment, α phase did not precipitate before the complete dissolution of ω phase. The

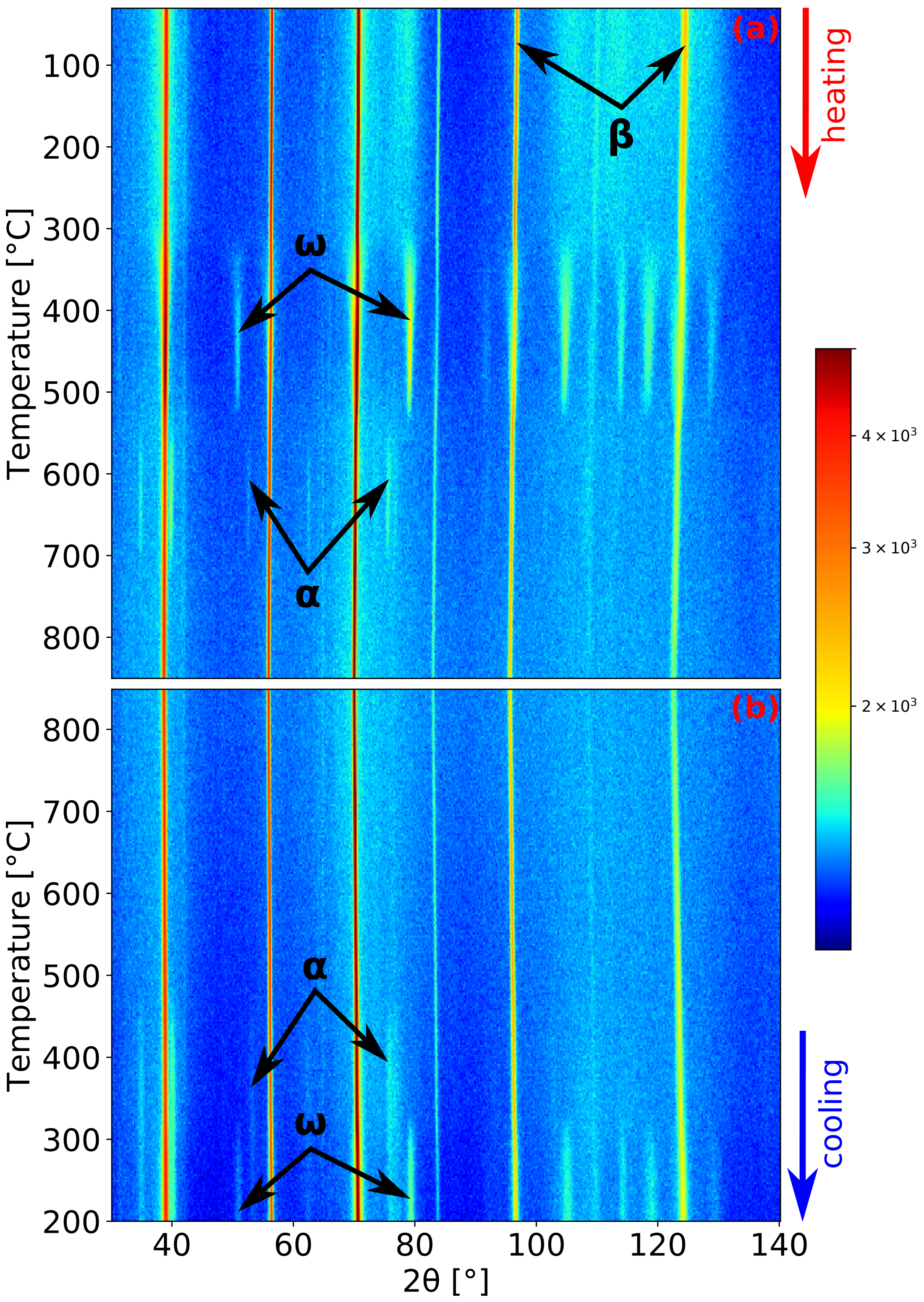

Figure 4.29: Neutron diffraction pattern evolution of Ti-15Mo during: (a) heating with the heating rate of 5 °C/min, (b) cooling with the cooling rate of 5 °C/min.

volume fraction of α phase formed during this experiment was much lower than in the previous one with the slower heating rate, testifying that α precipitation is a diffusion controlled process. Although it could appear from Fig. 4.29, that α phase does not completely dissolve during further heating to 850 °C. The diffraction

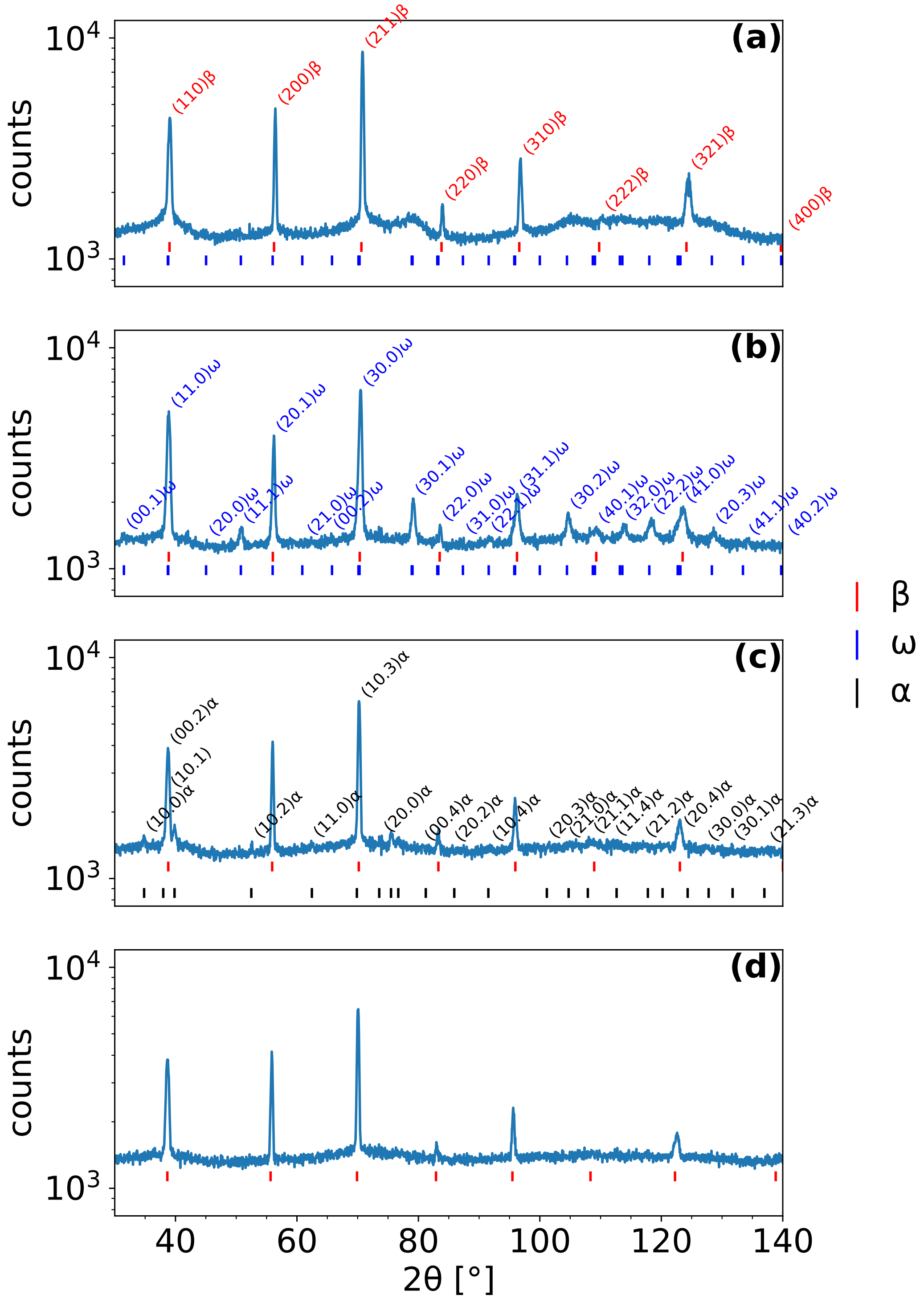

Figure 4.30: Selected diffraction patterns at different temperatures from Fig 4.29a). (a) Room temperature, (b) 465 °C, (c) 663 °C, (d) 850 °C.

pattern from the 850 °C temperature presented in Fig. 4.28d unambiguously proves that the sample consists solely of β phase. α phase dissolves at similar temperature as in the previous case (around 730 °C).

During the last experiment, the evolution of microstructure during ageing was

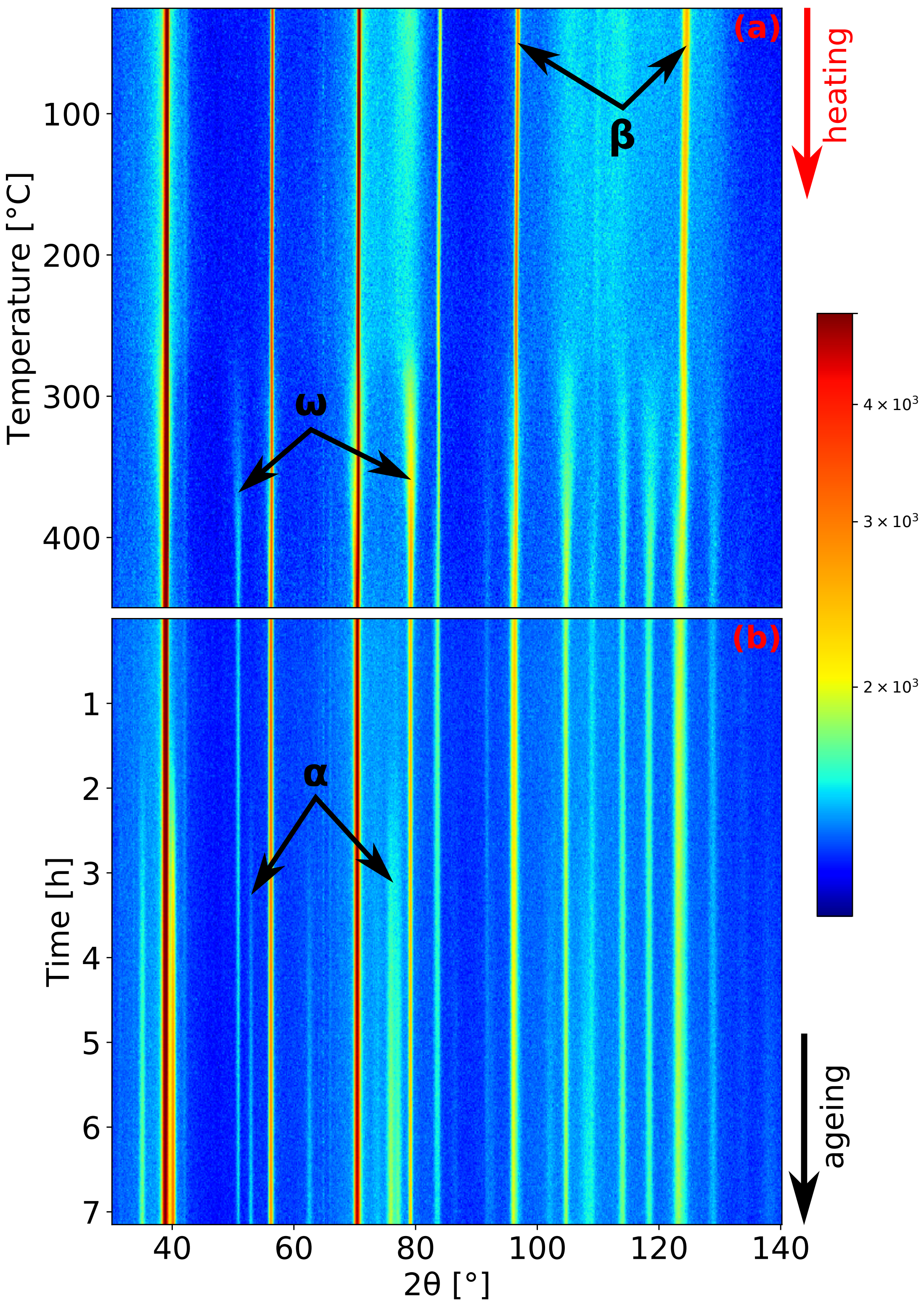

Figure 4.31: Neutron diffraction pattern evolution of Ti-15Mo during: (a) heating with the heating rate of 1.9 °C/min, (b) ageing at 450 °C.

studied. The initial condition of the material was identical to previous measurements (cf. Fig. 4.32a). The sample was heated up to 450 °C with the heating rate of 1.9 °C/min and then aged at this temperature for about 7 h. The material has 63 % of volume fraction of ω phase after reaching 450 °C (Fig. 4.32b). The

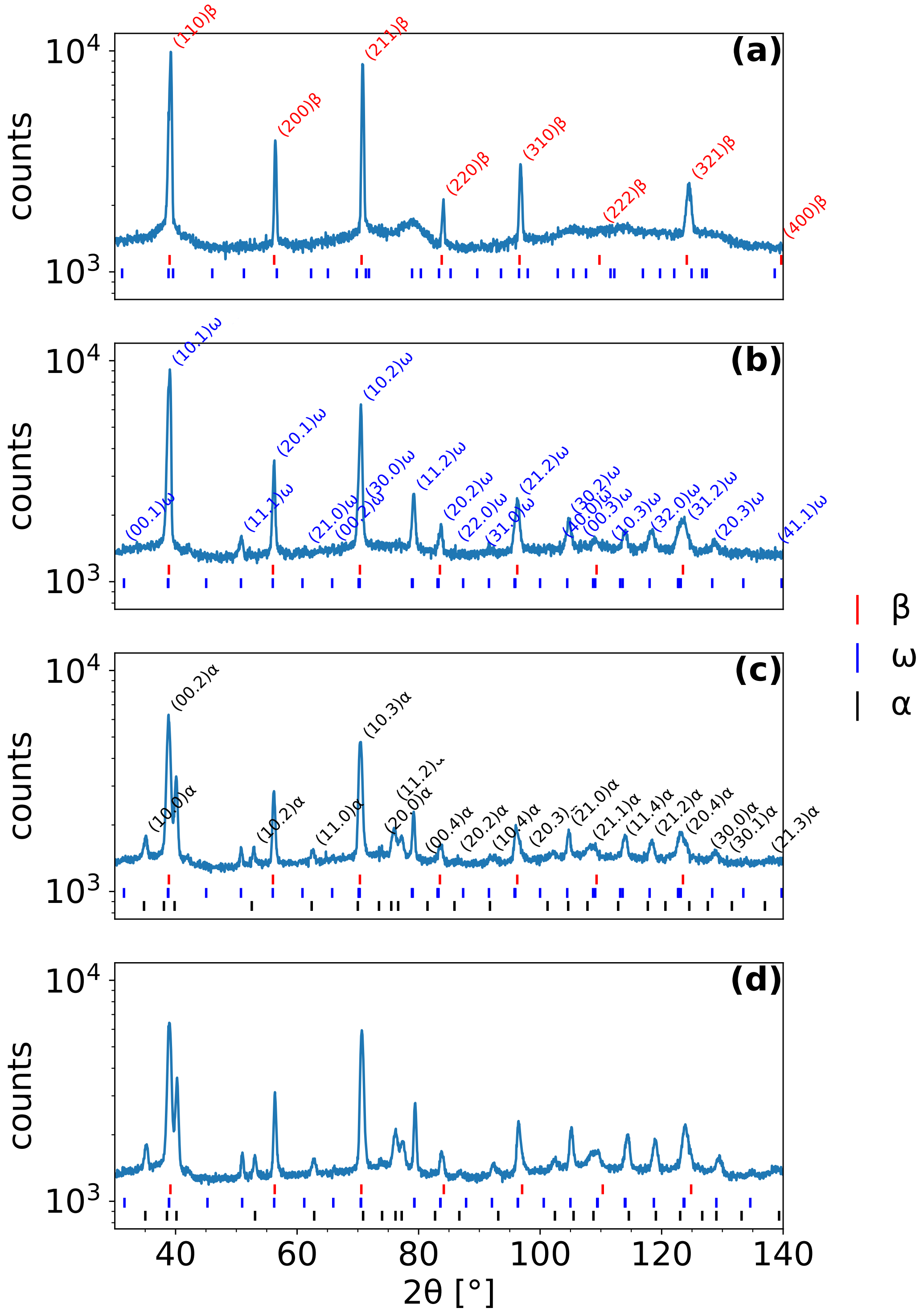

Figure 4.32: Selected diffraction patterns from different stages of heat treatment shown in Fig 4.31. (a) Room temperature, (b) 450 °C - beginning of the ageing, (c) 450 °C - end of ageing, (d) 150 °C cooled material (not shown in Fig 4.31).

kinetics of the formation of α phase can be observed in Fig. 4.31b. α peaks start to appear after approximately 1.5 h of ageing. After the ageing ($\sim$7 hours), volume fractions of β and ω phases decreased to 23 % and 39 %, respectively, while volume fraction of α risen to 38 % (see Fig. 4.32c). The decrease of the volume fraction of ω phase could be connected to α phase precipitation by consuming ω particles as was suggested in [5]. Due to time constraints the diffraction, the diffraction patterns were not acquired during cooling. After cooling down to 150 °C the volume fractions of α, β and ω phases were determined from Fig. 4.32d as 35 %, 15 % and 50 %, respectively. The increase of volume fraction of ω phase during cooling is obviously cause of the reduction of volume fraction of β phase.

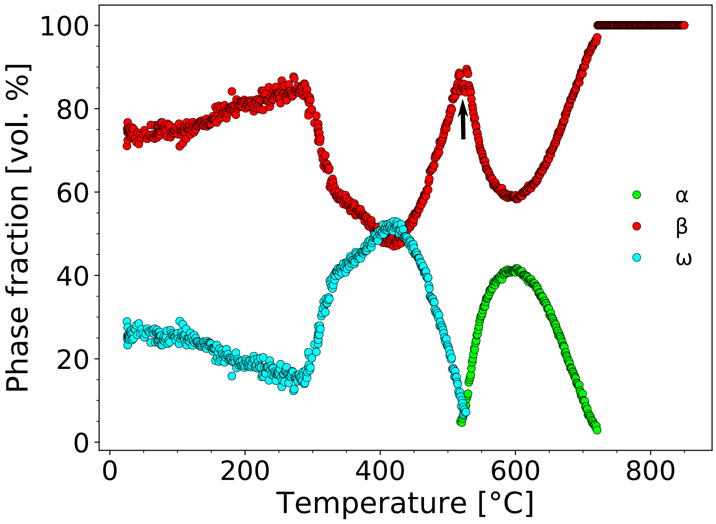

(a) Heating rate of 1.9 °C/min.

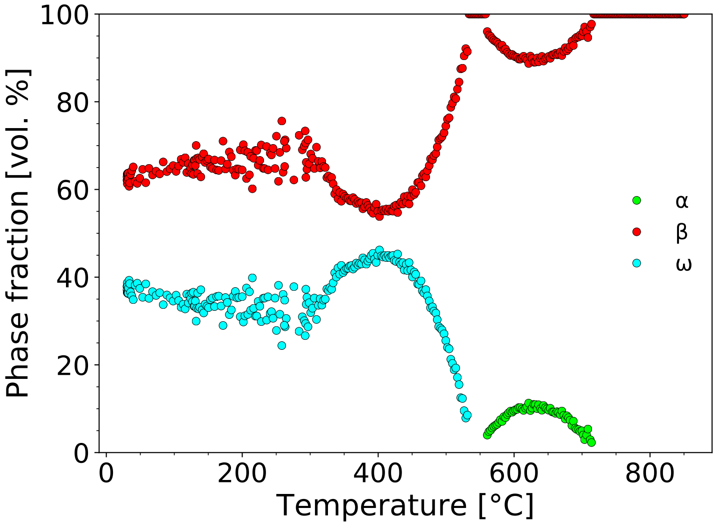

(b) Heating rate of 5 °C/min.

Figure 4.33: The evolution of volume fractions of α, β and ω phases during heating.

4.6.1 Volume fraction evolution

Evolutions of volume fractions of α, β and ω phases during heating with heating rates of 1.9 and 5 °C/min are shown in Fig. 4.33. For both heating rates, the volume fraction of ω phase initially decreases. The scatter of values at low temperatures is due to extremely small dimensions of ω particles, which hinders fitting of the diffraction patterns. At about 300 °C, the volume fraction of ω phase starts to grow, reaching its maximum volume at about 400 °C. The maximum volume fraction of ω phase is 52 % (due to the presence of Nb peaks in diffraction patter (see above in Fig. 4.28) this value is incorrect; the correct value of volume fraction of ω phase at this temperature determined from the ageing experiment is 68 %) and 45 % for the heating rates of 1.9 and 5 °C/min, respectively.

The volume fraction of ω phase continuously decreases up to 560 °C above which ω phase completely disappears. For the slower heating rate, a small temperature range ($\sim$9 °C) of coexistence of α and ω phases can be observed. It is probably due to precipitation of α phase on grain boundaries. This fact is supported by a small decrease of volume fraction of β phase in this temperature range (marked with the black arrow in Fig. 4.33a), while the rate of decrease of the volume fraction of ω phase remains constant. The volume fraction of α phase reaches the maximum value of 41 % and 11 % above 600 °C for the heating rates 1.9 and 5 °C/min, respectively. During subsequent heating, α phase dissolves back to β phase, which is manifested by the decrease of the the volume fraction for T>600 °C and T>620 °C for the heating rate of 1.9 and 5 °C/min, respectively.

The development of volume fractions of α, β and ω phases in the material aged at 450 °C is shown in Fig. 4.34. The kinetics of α phase growth was determined from the Avrami equation [38, 39]:

$$\zeta = A\{1 - \exp\left[-k(t-\tau)^n\right]\}, \tag{4.8}$$

where ζ represents the volume fraction of nucleated phase, k is the growth rate constant and A corresponds to the saturation value of the precipitating phase. In the standard Avrami equation τ refers to the incubation period, however in this case it stads for a time, when ω particles grow to a critical point and α phase begins to precipitate. With respect to shape of α precipitates, the exponent n was set $n = 1$, which corresponds to diffusion controlled growth of needles or plates [39]. The determined values of the coefficients from equation 4.8 are:

$$\begin{gathered} A = 0.51, \\ k = 0.24 \text{ h}^{-1}, \\ \tau = 1{,}57 \text{ h} \end{gathered}$$

The comparison of determined volume fraction of α phase with Avrami equation 4.8 with fitted parameters is shown in Fig. 4.35.

This analysis indicate that α phase starts to nucleate in Ti-15Mo after ageing for 94 minutes at 450 °C (the ageing time depends obviously on utilized heating rate). The saturated value of volume fraction of α was determined to be 51 %. After 8 and additional 11 hours (i.e. 19 in total) of ageing the volume fraction of alpha should be 40 % and 50 %, respectively. α phase grows at the expense of both β and ω phases, with the decrease of volume fraction of ω phase being slightly faster.

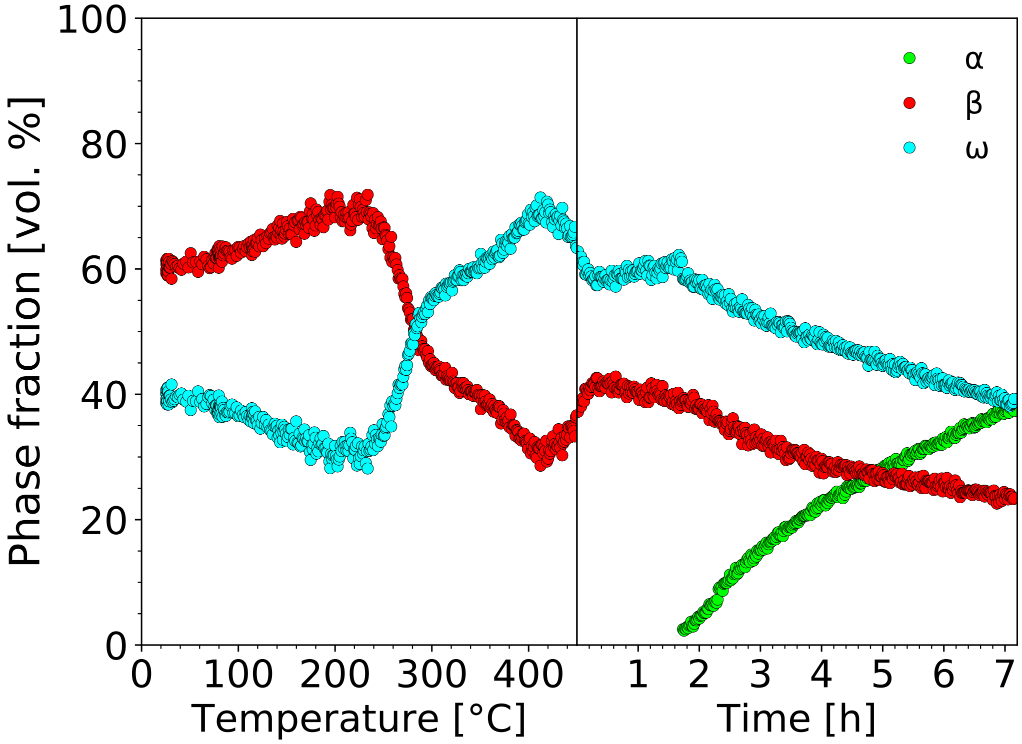

Figure 4.34: The evolution of volume fractions of α, β and ω phases during heating with the heating rate of 1.9 °C/min up to 450 °C followed by ageing for 7 h.

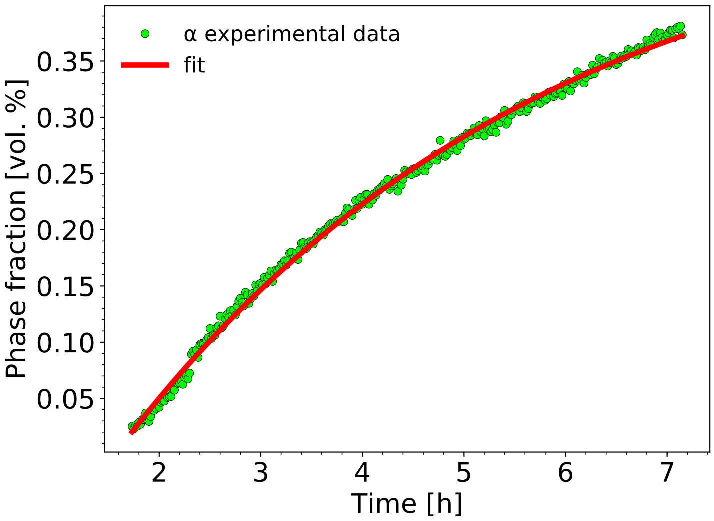

Figure 4.35: The comparison of measured volume fraction of α phase with Avrami equation 4.8 with fitted parameters.

4.6.2 Summary of ND

ND proved to be an efficient in-situ technique for the investigation of the kinetics of phase transformations in TiMo alloy. The volume fractions of α, β and ω phases were determined. It was shown that the heating rate influences the kinetics of the formation/dissolution of individual phases. During faster heating (the heating rate of 5 °C/min) ω phase completely dissolves before α phase forms. On the other hand, ND also showed, that α, β and ω phases can coexist by employing a suitably slow cooling, which is insufficient to suppress α phase formation. However, the amount of precipitated α phase should not be enough to stop ω phase formation. Another possibility to observe α and ω together is by ageing the material bellow the stability limit of ω phase (560 °C).

ND provided the most complex information of the phases evolution in-situ during heating/cooling/ageing compared to all other techniques. The main and only disadvantage is a limited accessibility of neutron source with sufficient neutron flux and equipment allowing in-situ observations.

4.7 Discussion

4.7.1 Comparison of diffraction experiments with electrical resistance

The electrical resistance of multiphase metals (i.e. metastable β-Ti alloys) is affected by the area of the phase interfaces and by stress fields around these interfaces [1]. The knowledge of mean values of the semiaxes R_L and R_V of ω particles and relative number of irradiated particles N/N_0, allows us to compare the evolution of the total β/ω interface area with electrical resistance in Fig. 4.36. The interface area S of one particle was calculated as the surface area of a prolate spheroid:

$$\begin{aligned} &S = 2\pi R_L\left(1+\frac{R_V}{R_L e}\arcsin(e)\right), \\ &\text{where } e^2 = 1-\frac{R_L^2}{R_V^2} \end{aligned} \tag{4.9}$$

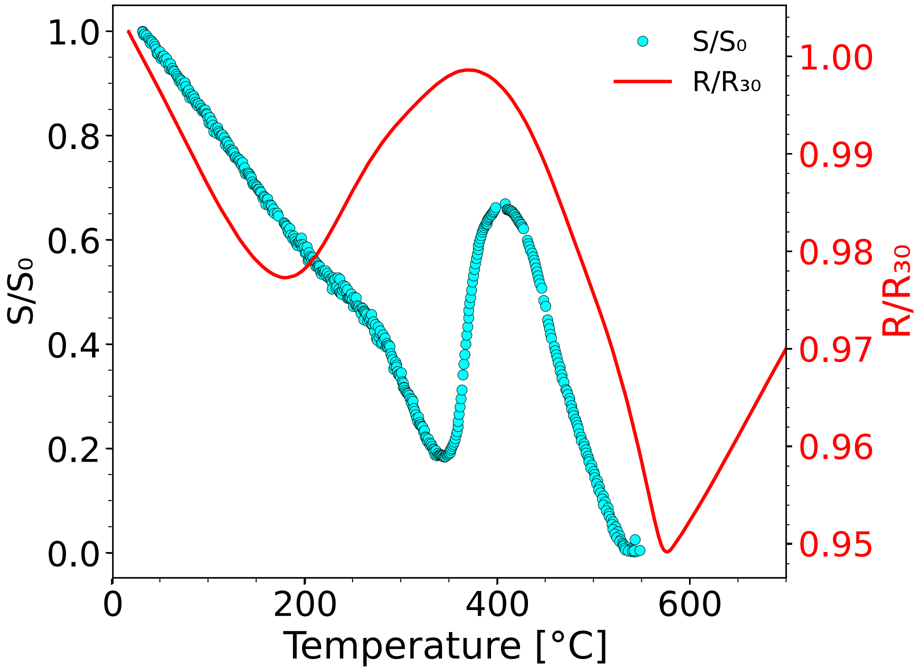

Figure 4.36: The comparison of evolution of electrical resistance of a single-crystal of Ti-15Mo and the relative area of β/ω interface calculated from $\{3\bar{3}0\bar{2}\}_\omega$ reflections.

Transformations ongoing in the low temperature region (bellow 200 °C) are fully reversible during repetitive cooling and heating [3, 40, 41]. The temperature of 200 °C is too low for the activation of diffusion driven processes in titanium alloys. It is believed that inverse shuffle transformation $\omega \to \beta$ is the dominant process causing a decrease both of volume fraction of ω phase and of the number of ω particles, therefore a decrease of the interface area. This is consistent with the initial decrease of electrical resistance. Furthermore, a decrease of elastic constants observed in this temperature range also supports this theory [37]. ND confirmed the decrease of the volume fraction of ω phase of about 10 %. The comparison of volume fractions of α and ω phases determined by ND with electrical resistance evolution is presented in Fig. 4.37.

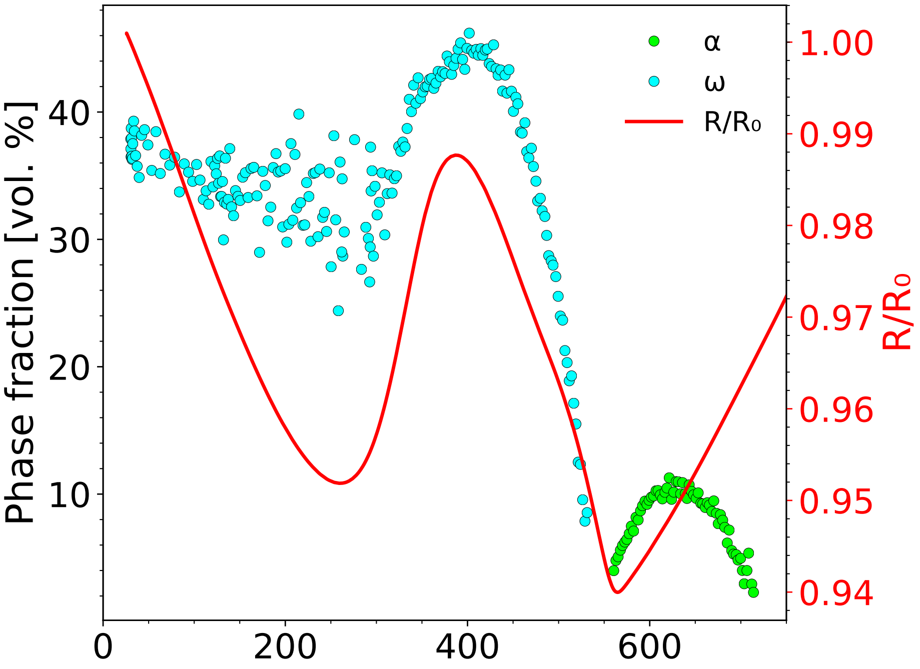

Figure 4.37: The comparison of the volume fraction of α and ω phases determined by ND with electrical resistance evolution during heating with the heating rate of 5 °C/min.

The increase of electrical resistance between 200 and 380 °C is most likely caused mainly by electron-phonon scattering and by an increase of the volume fraction of ω phase. The surface area of ω particles decreases up to 350 °C, which - coupled with an increase of the volume of ω phase - suggests, that ω particles grow while their number decreases.

Subsequent decrease of the total interface area, the volume fraction of ω phase and the electrical resistance between 430 °C and 560 °C should be caused by further coarsening of ω particles coupled with a decrease of the volume fraction of ω phase.

The complete dissolution of ω phase results in the sharp change of electrical resistance at about 560 °C. The precipitation of α phase followed by its dissolution shown in Fig. 4.37 have only a small influence on resistance at this heating rate and in Ti-15Mo alloy (small bump observable at 730 °C in Fig. 4.1). At the slower heating rate, a greater amount of α phase forms (cf. Fig. 4.33a), which results in a small bump of the electrical resistance (see Fig. 4.3). As a consequence, the increase of resistance observed at temperatures above 560 °C is mainly caused by electron-phonon scattering.

The slight shift in temperature between the results of each technique can have two reasons:

- the particular temperature of a change in the monotonicity of the electrical resistance curve does not correspond to the onset of a new process; it rather relates to the temperature at which the new process (electron scattering mechanism) prevails over the previous one,

- a slightly different position of thermocouples for each measurement might slightly affect the measured temperature values. The thermocouple for the electrical resistance, dilatometry and DSC [40] measurements is in a vicinity or even in a contact with the measured sample and the occurring processes are detected by these techniques at the same temperatures. On the other hand, during the XRD and ND, the thermocouples were placed at a certain distance from the investigated sample and the measured temperature could be lower that the real temperature of the specimen.

4.7.2 Comparison of XRD and ND

The comparison of the volume fraction of ω phase determined by ND and XRD is presented in Fig. 4.38. Both diffraction experiments were able to a detect decrease of the volume fraction of ω phase during heating up to about 300 °C, followed by its increase with the maximum at about 420 °C.The complete dissolution of ω phase was detected by both experiments at approximately the same temperature. The increase of volume fraction between 350 and 420 °C calculated

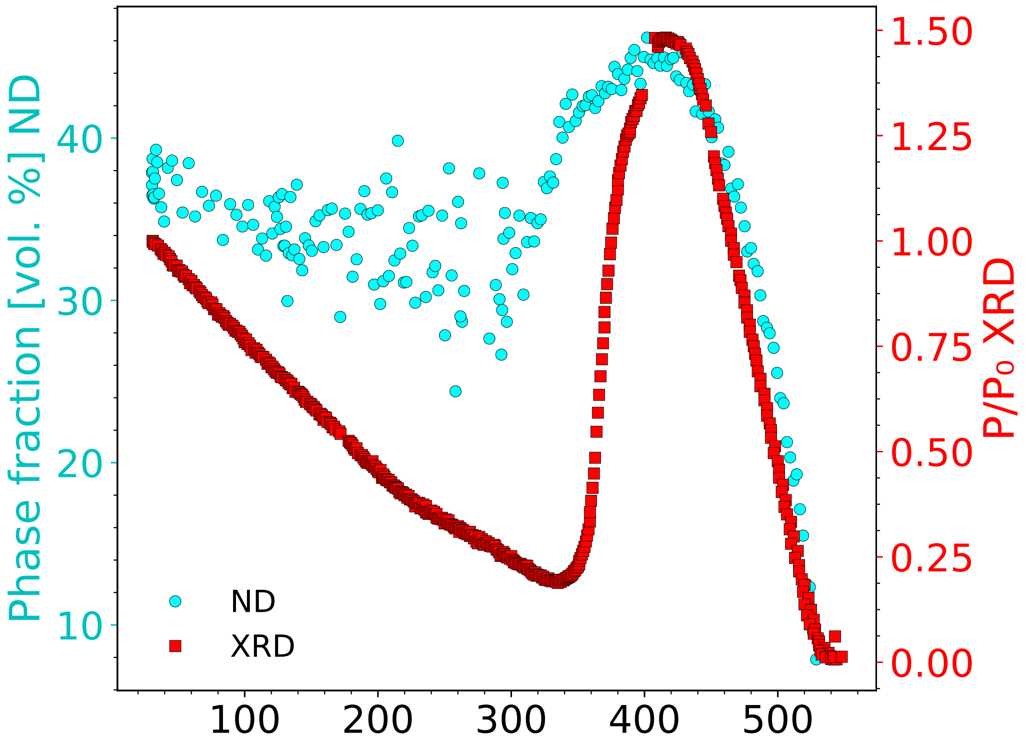

Figure 4.38: The comparison of the volume fraction of ω phase determined by ND and XRD during heating with the heating rate of 5 °C/min. XRD provided only relative values.

from XRD is several times higher than that determined from ND. This might be caused by neglection of the change of lattice parameter of ω phase during calculations of volume fraction from XDR data.

References

1. P. L. Rossiter: *The electrical resistivity of metals and alloys.* Cambridge solid state science series. Cambridge University Press, 1987. isbn: 978-0-521-24947-8.
2. F. Sun, F. Prima and T. Gloriant: High-strength nanostructured Ti–12Mo alloy from ductile metastable beta state precursor. *Materials Science and Engineering: A* **527**(16–17) (June 2010), 4262–4269. issn: 0921-5093. doi: 10.1016/j.msea.2010.03.044.
3. F. Prima, J. Debuigne, M. Boliveau and D. Ansel: Control of omega phase volume fraction precipitated in a beta titanium alloy: Development of an experimental method. *Journal of materials science letters* **19**(24) (2000), 2219–2221. doi: 10.1023/A:1006708420478.
4. A. Devaraj et al.: Three-dimensional morphology and composition of omega precipitates in a binary titanium-molybdenum alloy. *Scripta Materialia* **61**(7) (2009), 701–704. issn: 1359-6462. doi: 10.1016/j.scriptamat.2009.06.006.
5. F. Prima et al.: Nanostructured Metastable β-Titanium Based Alloy. *Journal of Metastable and Nanocrystalline Materials* **13** (2002), 307–314. issn: 1422-6375. doi: 10.4028/www.scientific.net/JMNM.13.307.
6. S. Banerjee and P. Mukhopadhyay: *Phase transformations: examples from titanium and zirconium alloys.* Pergamon materials series 12. Amsterdam ; Oxford: Elsevier/Pergamon, 2007, p. 813. isbn: 978-0-08-042145-2.
7. J. Disegi: *Implant Materials. Wrought Titanium –15% Molybdenum.* Synthes, 2009.
8. T. Gloriant et al.: Characterization of nanophase precipitation in a metastable β titanium-based alloy by electrical resistivity, dilatometry and neutron diffraction. *Scripta Materialia* **58**(4) (2008), 271–274. issn: 13596462. doi: 10.1016/j.scriptamat.2007.10.007.
9. Y. A. Shevchuk: Interdiffusion in the β Phases of the Ti–Ni and Ti–Fe Systems. *Inorganic Materials* **40** (Apr. 2004), 376–379. issn: 1608-3172. doi: 10.1023/B:INMA.0000023959.82728.70.
10. S.-Y. Lee, O. Taguchi and Y. Iijima: Diffusion of Aluminum in β-Titanium. *MATERIALS TRANSACTIONS* **51**(10) (2010), 1809–1813. doi: 10.2320/matertrans.M2010225.
11. W. Sprengel, T. Yamada and H. Nakajima: Interdiffusion in Binary β-Titanium Alloys. *Diffusion in Materials DIMAT 1996.* **143**. Defect and Diffusion Forum. Trans Tech Publications, Jan. 1997, 431–436. doi: 10.4028/www.scientific.net/DDF.143-147.431.
12. P. Zháňal et al.: Evolution of ω phase during heating of metastable β titanium alloy Ti–15Mo. *Journal of Materials Science* **53**(1) (Jan. 2018), 837–845. issn: 0022-2461, 1573-4803. doi: 10.1007/s10853-017-1519-2.
13. J. Šmilauerová, J. Pospíšil, P. Harcuba, V. Holý and M. Janeček: Single crystal growth of TIMETAL LCB titanium alloy by a floating zone method. *Journal of Crystal Growth* **405** (Nov. 2014), 92–96. issn: 0022-0248. doi: 10.1016/j.jcrysgro.2014.07.050.
14. J. Šmilauerová, P. Harcuba, J. Pospíšil, Z. Matěj and V. Holý: Growth of ω inclusions in Ti alloys: An X-ray diffraction study. *Acta Materialia* **61**(17) (Oct. 2013), 6635–6645. issn: 1359-6454. doi: 10.1016/j.actamat.2013.07.059.

15. A. Devaraj et al.: Experimental evidence of concurrent compositional and structural instabilities leading to ω precipitation in titanium–molybdenum alloys. *Acta Materialia* **60**(2) (2012), 596–609. issn: 13596454. doi: 10.1016/j.actamat.2011.10.008.
16. D. Schryvers and L. Tanner: High Resolution Electron Microscopy Observations of Athermal Omega Phase in Ti-Mo Alloys. *Materials Science Forum* **56-58** (1990), 329–334. issn: 1662-9752. doi: 10.4028/www.scientific.net/MSF.56-58.329.
17. P. Zháňal et al.: Phase Transformations in Metastable Ti-15Mo During Linear Heating. *Proceedings of the 13th World Conference on Titanium.* Ed. by V. Venkatesh et al. TMS (The Minerals, Metals & Materials Society), 2016, 431–436. doi: 10.1002/9781119296126.ch67.
18. T. Furuhara et al.: Morphology and Crystallography of α Precipitates in β Ti–Mo Binary Alloys. *Materials Transactions, JIM* **39**(1) (1998), 31–39. doi: 10.2320/matertrans1989.39.31.
19. Y. Zheng et al.: The role of the ω phase on the non-classical precipitation of the α phase in metastable β-titanium alloys. *Scripta Materialia* **111** (Jan. 2016), 81–84. issn: 13596462. doi: 10.1016/j.scriptamat.2015.08.019.
20. Y. Zheng et al.: Role of ω phase in the formation of extremely refined intragranular α precipitates in metastable β-titanium alloys. *Acta Materialia* **103** (Jan. 2016), 850–858. issn: 1359-6454. doi: 10.1016/j.actamat.2015.11.020.
21. M. Donachie: *Titanium: A Technical Guide.* AMS International, 1988. isbn: 0-87170-309-2.
22. E. Gemelli and N. H. A. Camargo: Oxidation kinetics of commercially pure titanium. *Matéria (Rio de Janeiro)* **12**(3) (2007), 525–531. issn: 1517-7076. doi: 10.1590/S1517-70762007000300014.
23. H. Rack, D. Kalish and K. Fike: Stability of as-quenched beta-III titanium alloy. *Materials Science and Engineering* **6**(3) (1970), 181–198. issn: 0025-5416. doi: 10.1016/0025-5416(70)90048-0.
24. G. Carter, H. M. Flower, G. M. Pennock and D. R. F. West: The deformation characteristics of metastable β-phase in a Ti-15 wt. % Mo alloy. *Journal of Materials Science* **12**(11) (Nov. 1977), 2149–2153. issn: 0022-2461, 1573-4803. doi: 10.1007/BF00552235.
25. J. M. Bennett et al.: Observation of a new B2 structured phase in Ti-15Mo (wt%). *Materials Characterization* **142** (Aug. 2018), 523–530. issn: 1044-5803. doi: 10.1016/j.matchar.2018.06.017.
26. G. M. Pennock, H. M. Flower and D. R. F. West: The thinning transformation in β Ti-Mo alloys. *Metallography* **10**(1) (Feb. 1977), 43–53. issn: 0026-0800. doi: 10.1016/0026-0800(77)90042-8.
27. W. H. Bragg and B. A. WL Bragg: The reflection of X-rays by crystals. *Proc. R. Soc. Lond. A*. Vol. 88. The Royal Society, 1913, pp. 428–438. doi: 10.1098/rspa.1913.0040.
28. P. P. Ewald: Introduction to the dynamical theory of X-ray diffraction. *Acta Crystallographica Section A* **25**(1) (Jan. 1969), 103–108. doi: 10.1107/S0567739469000155.
29. J. M. Silcock: An X-ray examination of the to phase in TiV, TiMo and TiCr alloys. *Acta Metall* **6**(7) (1958), 481–493. doi: 10.1016/0001-6160(58)90111-1.

30. T. L. Trenogina and R. M. Lerinman: *Titanium and Titanium Alloys: Scientific and Technological Aspects Volume 3*. Ed. by J. C. Williams and A. F. Belov. 1st ed. Springer US, 1982. isbn: 978-1-4757-1758-7. doi: 10.1007/978-1-4757-1758-7.

31. S. Ankem and C. A. Greene: Recent developments in microstructure/property relationships of beta titanium alloys. *Materials Science and Engineering: A* **263**(2) (1999), 127–131. issn: 0921-5093. doi: 10.1016/S0921-5093(98)01170-8.

32. S. Azimzadeh and H. J. Rack: Phase transformations in Ti-6.8Mo-4.5Fe-1.5Al. *Metall and Mat Trans A* **29**(10) (1998), 2455–2467. issn: 1073-5623, 1543-1940. doi: 10.1007/s11661-998-0217-8.

33. C. Leyens and M. Peters, eds.: *Titanium and titanium alloys: fundamentals and applications*. Weinheim : Chichester: Wiley-VCH; John Wiley, 2003, p. 513. isbn: 978-3-527-30534-6. doi: 10.1002/3527602119.

34. V. A. Drits: *Electron Diffraction and High-Resolution Electron Microscopy of Mineral Structures*. Springer Berlin Heidelberg, 1987. isbn: 978-3-642-71731-4. doi: 10.1007/978-3-642-71729-1.

35. J. Šmilauerová, P. Harcuba, D. Kriegner, M. Janeček and V. Holý: Growth kinetics of particles in β-Ti matrix studied by in situ small-angle X-ray scattering. *Acta Materialia* **100** (Nov. 2015), 126–134. issn: 1359-6454. doi: 10.1016/j.actamat.2015.08.014.

36. J. Šmilauerová, P. Harcuba, D. Kriegner and V. Holý: On the completeness of the $\beta \rightarrow \omega$ transformation in metastable β titanium alloys. *Journal of Applied Crystallography* **50**(1) (Feb. 2017), 283–287. doi: 10.1107/S1600576716020458.

37. J. Nejezchlebová et al.: The effect of athermal and isothermal ω phase particles on elasticity of β-Ti single crystals. *Acta Materialia* **110** (May 2016), 185–191. issn: 1359-6454. doi: 10.1016/j.actamat.2016.03.033.

38. M. Avrami: Kinetics of Phase Change. II Transformation-Time Relations for Random Distribution of Nuclei. *The Journal of Chemical Physics* **8**(2) (1940), 212–224. doi: 10.1063/1.1750631.

39. J. Christian. Oxford: Pergamon, 2002, p. 568. isbn: 978-0-08-044019-4. doi: 10.1016/B978-008044019-4/50016-7.

40. P. Zháňal et al.: Phase Transformations in Ti-15Mo Investigated by in situ Electrical Resistance. *Acta Physica Polonica A* **128**(4) (2015), 779–783. issn: 0587-4246, 1898-794X. doi: 10.12693/APhysPolA.128.779.

41. J. C. Ho and E. W. Collings: Anomalous Electrical Resistivity in Titanium-Molybdenum Alloys. *Physical Review B* **6**(10) (1972), 3727.

Conclusions

This thesis aimed to investigate phase transformations in metastable β titanium alloys, with emphasis on Ti-15Mo alloy, which represents a simple binary system. The thesis mainly focuses on evolution of ω phase. The materials were studied by electrical resistance and dilatometry complemented with ex-situ (post-mortem) TEM allowed to identify individual processes.

In-situ TEM proved to be an inappropriate method for analysis of metastable Ti alloys due to strong thin foil effect.

XRD performed in single crystal allowed to distinguish all 4 crystallographic families of ω and all 12 variants of α phase. Reflections from all α and ω variants exhibit the same evolution with temperature. Therefore, none of the variants is preferred. Furthermore, relative volume fraction of ω phase was determined.

ND provided information of evolution all phases present in the material (α, β and ω) in-situ during heating/cooling/ageing.

The following conclusions can be drawn from the comparison of utilized methods:

- Electrical resistance dependence on temperature of all investigated alloys is not linear, which is typical for metals. In several temperature regions the slope of the dependence ($d\rho/dT$) is even negative.

- The reduction of lattice parameters of β and ω phases around 330 °C is manifested macroscopically by the reduction of material length (negative linear thermal expansion coefficient) with increasing temperature.

- The sharp change of electrical resistance (observed in Ti-15Mo, LCB and TNFS) and an abrupt decrease of thermal expansion coefficient of Ti-15Mo correspond to complete dissolution of ω phase followed by the formation of α phase.

- Both TEM and XRD observations confirmed the orientation relationship known from literature between ω and β phases and identified orientation relationships between α and β.

- Relative changes of the size of ω particles and β/ω interface area during heating was determined by XRD.

- The evolution of the volume fractions of α, β and ω during heating was determined from ND experiments.

- The diffraction experiments unambiguously explained processes identified by indirect measurements.

Future research plans

The future research of metastable β-Ti alloys will firstly continue by processing of already obtained ND data. In particular, the evolution of the volume fractions of α, β and ω phases during cooling will be determined. The record of this measurement already explained a sudden increase of electrical resistance during cooling at about 380 °C as the start of nucleation of ω phase (cf. Figs. 4.39 and 4.29).

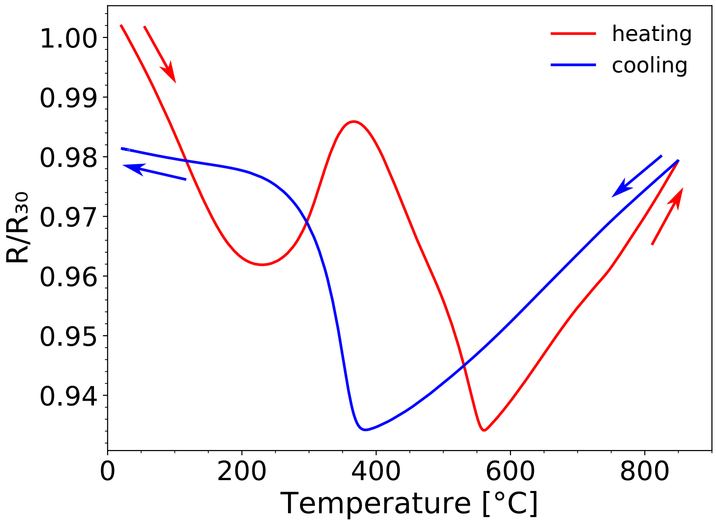

Figure 4.39: The evolution of electrical resistance of Ti-15Mo alloys during heating and cooling with the rate of 5 °C/min.

Additional work will focus on the correction of the determination of the volume fraction evolution during heating with the heating rate of 1.9 °C, which was affected by presence Nb peaks. The determined values should be equal to those determined from the ageing experiment (cf. Figs. 4.33a and 4.34). On the other hand, the presence of Nb peaks will provide a tool for correcting the shift of the measured values of temperature during ND and electrical resistance experiments. The thermal expansion of Nb lattice parameters will allow us to calibrate the measured temperature to correct values.

Another direction of future research is to investigate in detail other metastable β-Ti alloys as is mentioned in Appendices.

Appendix

The results presented in this chapter are beyond the main objective of the thesis. The purpose of their presentation is to show several ways of further research in the area of phase transformation of metastable β-Ti alloys which were evoked by results obtained during my doctoral study. Several results are only preliminary and their complete interpretation will be subject of future investigation.

A Effect of the heating rate on electrical resistance of Ti-5553

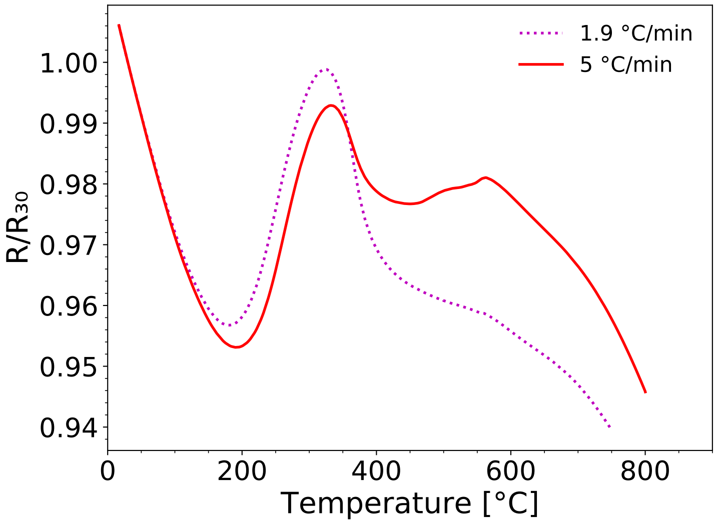

Figure 40: The electrical resistance of Ti-5553 during heating with different heating rates.

The first minimum and maximum of the electrical resistance of Ti-5553 alloy, shown in Fig. 40, are slightly shifted to higher temperatures for faster heating rate. For the temperatures above 350 °C the curves start to differ remarkably. The curve corresponding to the heating rate of 1.9 °C/min (dotted magenta line) decreases with a small bump at about 560 °C. On the other hand, for the heating rate of 5 °C/min (red line) there is a noticeable increase of electrical resistance accompanied by two additional bumps. The second one, which is at about 560 °C, is followed by the continuous decrease of the resistance with temperature. Similar bump at the same temperature of 560 °C was observed also at the curve corresponding to the slower heating rate (dotted magenta line). It is assumed that these bumps are caused by the same process as they occur at the same temperature. As the temeprature of these bumps is almost independet of the heating rate, they might be related to the dissolution of ω phase. The presumed limit of stability of ω phase (at 560 °C) manifests itself as the local maximum of the electrical resistance, which is quite opposite than in Ti-15Mo and LCB (local minimum), cf. Figs. 4.3, 4.4 and 40. It was shown in [1], that, unlike in TiMo and LCB, in

Ti-5553 α phase precipitates before ω phase dissolves. The presence of α phase bellow the stability limit of ω phase could result in such different manifestation. However, detail TEM observations are needed to confirm this assumption.

The decrease in electrical resistance observed between 560 and 800 °C (the highest measured temperature for Ti-5553) is likely caused by the dissolution of α phase towards β-transus. Ti-5553 is the least β stabilized of all studied alloys, therefore, its β-transus temperature is the highest and was not reached during heating up to 800 °C.

B Comparison of electrical resistance evolution of different alloys

Next to Ti-15Mo, LCB an Ti-5553, the electrical resistance evolution was investigated in other metastable β-Ti alloys (TNFS, Timetal 21S and TCFA) with the aim to reveal the effect of alloying elements on phase transformations in this class of materials. These alloys, whose promising properties were described in Materials section, are only present at Department of Physics of Materials shortly and will be subject of thorough investigation in the near future.

The comparison of electrical resistance evolution of all investigated alloys during heating with the heating rate of 5 °C/min is shown in Figs. 41 and 42. The values of resistance for all alloys were normalized by R_{30}. For clarity the alloys are divided into two groups and compared separately in Figs. 41 and 42. The electrical resistance dependence on temperature of all alloys of the first group (LCB, Ti-15Mo, TNFS and Ti-5553) exhibits a distinct common feature, which could be identified as the stability limit of ω phase (local minimum at 500 °C for LCB and TNFS and at 560 °C for Ti-15Mo and local maximum for Ti-5553). On the other hand, TCFA and Timetal 21S alloys does not exhibit such characteristics and, therefore, their electrical resistance evolution is compared to that of Ti-15Mo in Fig. 42.

Due to different behaviour of TNFS alloy compared to others at low temperatures, its resistance values are on the right y axis in Fig. 41. It is obvious, that at low temperatures the electrical resistance of TNFS alloy increases with increasing temperature, while the values of resistance for all other alloys decrease with increasing temperature. This behaviour of TNFS alloys is probably caused by its main alloying element - Nb, which hinders the formation of ω phase [2].

Despite the electrical resistivity of metals typically increases with increasing temperature due to lattice vibrations, the evolution of electrical resistivity of all studied metastable β alloys exhibits significant drops due to ongoing phase transformations. During the dissolution of ω_{ath} particles upon heating to approx. 200 °C (observed for all alloys; for TNFS this deacease starts at 100 °C), the elastic strains are released, which clears the matrix and enhances the electron path and reduces the electrical resistance [3–6].

All electrical resistance curves show similar characteristics, more or less distinct for each alloy. At temperatures above about 200 °C, LCB, Ti-15Mo, Ti-5553 and TNFS alloys exhibit apparent increase of the electrical resistance which is related to irreversible formation of ω_{iso} particles and to common increase of the electrical resistance with increasing temepratur [4, 5, 7, 8] (see Fig. 41). Small

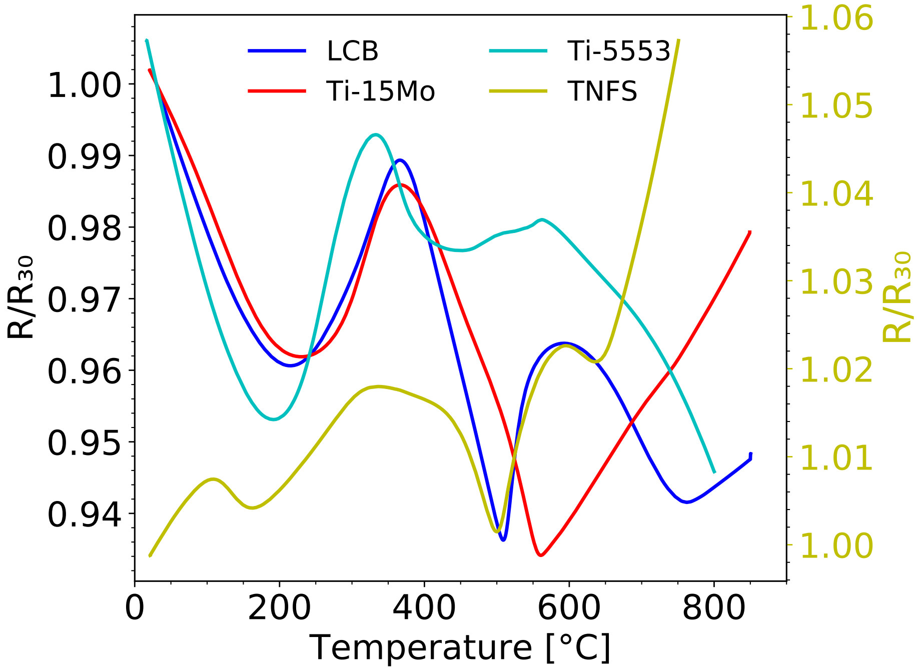

Figure 41: The evolution of electrical resistance of LCB, Ti-15Mo, TNFS and Ti-5553 alloys during heating with the heating rate of 5 °C/min.

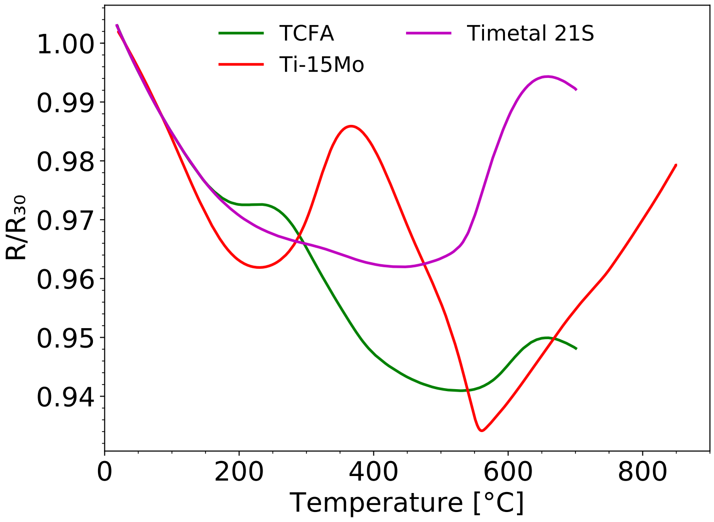

Figure 42: The evolution of electrical resistance of TCFA and Timetal 21S alloys compared to that of Ti-15Mo during heating with the heating rate of 5 °C/min.

bump can be also observed in evolution of TCFA (green line in Fig. 42). A detail examination of the curve of Timetal 21S (magenta line in Fig. 42) reveals a faint bump/plateau around 300 °C just before the curve starts to decrease faster. The presence of this plateau on electrical resistance curves of TCFA and Timetal 21S suggests, that in these two alloys only small amount of ω_{iso} phase precipitates during heating.

The significant decrease of the electrical resistance, which is observed during subsequent heating of LCB, Ti-15Mo and TNFS alloys between ∼400 - ∼500 °C (see Fig. 41), ending with a steep increase is caused solely by $\beta \leftrightarrow \omega$ transformations (some ω particles grow: $\beta \rightarrow \omega$, the volume fraction of ω phase decreases: $\beta \leftarrow \omega \Rightarrow \beta \leftrightarrow \omega$).

On the other hand, the electrical resistance of TCFA and Timetal 21S does not exhibit this sharp change at the stability limit of ω phase. Therefore, the α phase probably forms before the complete dissolution of ω phase, which results in gradual increase of the electrical resistance from 450 and 520 °C for Timetal 21S and TCFA, respectively.

The electrical resistance increase followed by a decrease during heating in temperature interval 510 - 750 °C in LCB (510 - 650 °C - TNFS; 560 - 730 °C - Ti-15Mo - only small bump is present; 520 - 750 °C - TCFA, Timetal 21S - the upper limit is higher for these two alloys, however, 750 °C was maximum reached temperature) is, in all alloys except for Ti-5553, caused by $\beta \leftrightarrow \alpha$ transformations coupled with thermal increase of resistivity due to lattice vibrations [8].

Final increase of the electrical resistance of LCB, TNFS and Ti-15Mo should be caused solely by the electron-phonon scattering because the materials are above their respective β-transus temperatures. β-transus temperature was not reached for TCFA, Timetal 21S and TNFS alloys.

C The evolution of electrical resistance of metastable β-Ti alloys during heating with the heating rate of 1.9 °C/min.

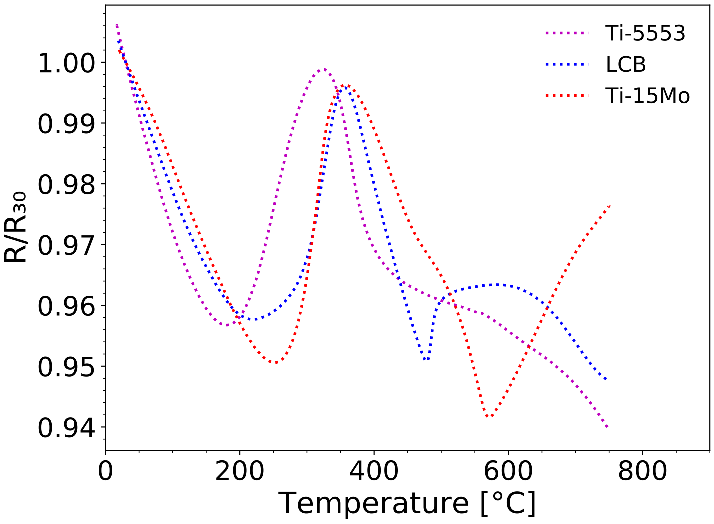

Figure 43: The evolution of electrical resistance of metastable β-Ti alloys during heating with the heating rate of 1.9 °C/min.

D Record of in-situ XRD experiment - CD

E Interactive Fig. 4.17 - CD

F Interactive Fig. 4.20 - CD

References

1. A. Settefrati et al.: Precipitation in a near Beta Titanium Alloy on Ageing: Influence of Heating Rate and Chemical Composition of the Beta-Metastable Phase. *Solid State Phenomena* **172–174** (June 2011), 760–765. issn: 1662-9779. doi: 10.4028/www.scientific.net/SSP.172-174.760.
2. C. W. Dawson and S. L. Sass: The as-quenched form of the omega phase in Zr-Nb alloys. *Metallurgical Transactions* **1**(8) (Aug. 1970), 2225–2233. issn: 1543-1916. doi: 10.1007/BF02643439.
3. M. Ikeda, S. Komatsu, T. Sugimoto and K. Kamei: Negative Temperature Dependence of Resistivity in Ti-Mo Binary Alloys. *Proc. 6th Conf. on Ti.* Societe de France Met., 1988, 313–318.
4. T. Gloriant et al.: Synthesis and Phase Transformations of Beta Metastable Ti-Based Alloys Containing Biocompatible Ta, Mo and Fe Beta-Stabilizer Elements. *Advanced Engineering Materials* **8**(10) (Oct. 2006), 961–965. issn: 1527-2648. doi: 10.1002/adem.200600106.
5. T. Gloriant et al.: Characterization of nanophase precipitation in a metastable β titanium-based alloy by electrical resistivity, dilatometry and neutron diffraction. *Scripta Materialia* **58**(4) (2008), 271–274. issn: 13596462. doi: 10.1016/j.scriptamat.2007.10.007.
6. P. Zháňal et al.: Phase Transformations in Ti-15Mo Investigated by in situ Electrical Resistance. *Acta Physica Polonica A* **128**(4) (2015), 779–783. issn: 0587-4246, 1898-794X. doi: 10.12693/APhysPolA.128.779.
7. F. Prima et al.: Nanostructured Metastable β-Titanium Based Alloy. *Journal of Metastable and Nanocrystalline Materials* **13** (2002), 307–314. issn: 1422-6375. doi: 10.4028/www.scientific.net/JMNM.13.307.
8. P. Zháňal et al.: Evolution of ω phase during heating of metastable β titanium alloy Ti–15Mo. *Journal of Materials Science* **53**(1) (Jan. 2018), 837–845. issn: 0022-2461, 1573-4803. doi: 10.1007/s10853-017-1519-2.

List of Figures

List of Tables

List of Abbreviations

(hkl)	crystallographic plane with Miller indices h, k and l
$[hkl]$	crystallographic direction with Miller indices h, k and l
$\{hkl\}$	set of all planes equivalent to (hkl)
$\langle hkl \rangle$	set of all directions equivalent to [hkl]
bcc	body-centered cubic
DF	dark field
ESRF	European Synchrotron Radiation Facility
hcp	hexagonal close-packed
HRTEM	High resolution transmission electron microscopy
ILL	Institut Laue-Langevin
LCB	low-cost beta (Ti-6.8Mo-4.5Fe-1.5Al)
LVDT	linear variable differential transformer
ND	neutron diffraction
PC	poly crystal
SAED	selected area diffraction pattern
SC	single crystal
SEM	scanning electron microscopy
SM	simple metal
ST	solution treated
TCFA	Ti-13Cr-1Fe-3Al
TEM	transmission electron microscopy
Ti-5553	Ti-5Al-5V-5Mo-3Cr
Timetal 21S	Ti-15Mo-3Nb-3Al-0.2Si
TNFS	Ti-29Nb-1Fe-0.5Si
XRD	X-ray diffraction
α_L	linear expansion coefficient
ω_{ath}	athermal ω; formed during quenching by a diffusionless shuffle mechanism
ω_{iso}	isothermal ω; formed during ageing by a diffusion-assisted mechanism

List of publications

1. Harcuba P, Hájek M, Zháňal P. Mechanical Properties and Microstructure Evolution of Ultra-fine Grained CP Ti. METAL 2013 Conference Proceedings, Brno: Tanger; 2013, p. 1480–6.
2. Strasky J, Harcuba P, Hajek M, Vaclavova K, Zhanal P, Janecek M, et al. Microstructure evolution in ultrafine-grained Ti and Ti-6Al-7Nb alloy processed by severe plastic deformation. IOP Conference Series: Materials Science and Engineering 2014;63:012072. doi:10.1088/1757-899X/63/1/012072.
3. Černý I, Sís J, Zháňal P. Fatigue Resistance of Laser Welded S355 Steel Sheet. Key Engineering Materials 2015;665:69–72. doi:10.4028/www.scientific.net/KEM.665.69.
4. Zháňal P, Harcuba P, Šmilauerová J, Stráský J, Janeček M, Smola B, et al. Phase Transformations in Ti-15Mo Investigated by in situ Electrical Resistance. Acta Physica Polonica A 2015;128:779–83. doi:10.12693/APhysPolA.128.779.
5. Zháňal P, Hájek M, Harcuba P. Microstructural Changes in β-Ti Alloy Investigated by Electrical Resistance. WDS'15 Proceedings of Contributed Papers — Physics, Prague: MATFYZPRESS; 2015, p. 54–60.
6. Harcuba P, Šmilauerová J, Hájek M, Zháňal P, Čapek J. Phase Transformations in Beta-Ti Alloys Studied by In-Situ Methods. In: Venkatesh V, Pilchak AL, Allison JE, Ankem S, Boyer R, Christodoulou J, et al., editors. Proceedings of the 13th World Conference on Titanium, John Wiley & Sons, Inc.; 2016, p. 437–41.
7. Lukáč F, Čížek J, Knapp J, Procházka I, Zháňal P, Islamgaliev RK. Ultra fine grained Ti prepared by severe plastic deformation. J Phys: Conf Ser 2016; 674:012007. doi:10.1088/1742-6596/674/1/012007.
8. Zháňal P, Harcuba P, Janeček M, Šmilauerová J, Veselý J, Smola B, et al. Phase Transformations in Metastable Ti-15Mo During Linear Heating. In: Venkatesh V, Pilchak AL, Allison JE, Ankem S, Boyer R, Christodoulou J, et al., editors. Proceedings of the 13th World Conference on Titanium, John Wiley & Sons, Inc.; 2016, p. 431–6.
9. Zháňal P, Václavová K, Hadzima B, Harcuba P, Stráský J, Janeček M, et al. Thermal stability of ultrafine-grained commercial purity Ti and Ti–6Al–7Nb alloy investigated by electrical resistance, microhardness and scanning electron microscopy. Materials Science and Engineering: A 2016; 651:886–92. doi:10.1016/j.msea.2015.11.029.
10. Stráská J, Zháňal P, Václavová K, Stráský J, Harcuba P, Čížek J, et al. Thermal Stability of Ultra-Fine Grained Microstructure in Mg and Ti Alloys. In: Cabibbo M, editor. Severe Plastic Deformation Techniques, InTech; 2017. doi:10.5772/intechopen.68956.

11. Václavová K, Stráský J, Zháňal P, Veselý J, Polyakova V, Semenova I, et al. Ultra-fine grained microstructure of metastable beta Ti-15Mo alloy and its effects on the phase transformations. IOP Conf Ser: Mater Sci Eng 2017;194:012021. doi:10.1088/1757-899X/194/1/012021.

12. Zháňal P, Harcuba P, Hájek M, Šmilauerová J, Veselý J, Janeček M. Characterization of Phase Transitions Occurring in Solution Treated Ti-15Mo during Heating by Thermal Expansion and Electrical Resistance Measurements. Materials Science Forum 2017;879:2318–23. doi:10.4028/www.scientific.net/MSF.879.2318.

13. Zháňal P, Harcuba P, Hájek M, Smola B, Stráský J, Šmilauerová J, et al. Evolution of ω phase during heating of metastable β titanium alloy Ti–15Mo. Journal of Materials Science 2018; 53:837–45. doi:10.1007/s10853-017-1519-2.

14. Zoul D, Zháňal P. 3D reconstruction of radioactive sample utilizing gamma tomography. Nuclear Instruments and Methods in Physics Research Section A: Accelerators, Spectrometers, Detectors and Associated Equipment 2018;895:107–11. doi:10.1016/j.nima.2018.03.071.